

TECHNISCHE UNIVERSITÄT MÜNCHEN
FAKULTÄT FÜR CHEMIE
LEHRSTUHL FÜR THEORETISCHE CHEMIE

DISSERTATION

**RESPONSE PROPERTIES AT
DYNAMIC LIQUID-LIQUID
INTERFACES**

ZHU LIU

Garching b. München, November 2017

TECHNISCHE UNIVERSITÄT MÜNCHEN

Fakultät für Chemie

Lehrstuhl für Theoretische Chemie

**Response Properties at
Dynamic Liquid-Liquid Interfaces**

Zhu Liu

Vollständiger Abdruck der von der Fakultät für Chemie der
Technischen Universität München zur Erlangung des akademischen
Grades eines

Doktors der Naturwissenschaften (Dr. rer. nat.)

genehmigten Dissertation.

Vorsitzender: Prof. Dr. Ville Kaila

Prüfer der Dissertation: 1. Prof. Dr. Karsten Reuter
2. Prof. Dr. Martin Elsner

Die Dissertation wurde am 28.11.2017 bei der Technischen Universität
München eingereicht und durch die Fakultät für Chemie am 11.01.2018
angenommen.

*Dedicated to my fiancée,
Yuanyuan.*

Abstract

The knowledge of dielectric response properties of the environment is of paramount importance in many theoretical embedding methods and studies of solutes and catalytic sites and processes in condensed phases. In particular, the realistic embedding of active sites into solid/liquid and liquid/liquid interfaces is a crucial point in the context of modeling energy conversion (e.g., electrochemical, photochemical, power-to-X) processes. Recently, the finding that the dielectric permittivity of liquids near solid/liquid interfaces is far from being constant but deviates strongly from the bulk value within several nanometers from the interface has raised the interest in a more fundamental understanding of the response properties near interfaces. As these questions are hard to study experimentally, reliable theoretical models are required. Here we describe a careful first-principles based reparametrization of nonpolarizable molecular mechanics force fields for a class of technological relevant organic chlorinated hydrocarbon solvents which are immiscible with water. For the solvent 1,2-dichloroethane (1,2-DCE) we also present a new polarizable force field based on the Drude oscillator model. Its parametrization needs particular attention to avoid unphysical couplings between the internal torsional degree of freedom and the Drude oscillators, which could severely skew the response properties. The performance of this new set of force fields is critically

assessed based on a comprehensive molecular dynamics study.

Despite the importance of the dielectric continuum response property of liquids at a shared interface, simulations of interfacial dielectric properties have so far mostly considered the case of confined liquids at a rigid solid-mobile liquid interface. Liquid-liquid interfaces are instead known to be intrinsically fluxional in nature. This requires statistical procedures devised to analyze molecular dynamics simulations for the computation of the dielectric tensor fields to be adjusted accordingly. We present a novel coarse grain approach to this problem which yields dielectric profiles with features of similar sharpness as for the solid-liquid case – if the statistical analysis is consistently referenced to the instantaneous liquid-liquid interface. In contrast, simple statistical analyses based on an average interface definition only result in broadened featureless dielectric profiles across the interface region. Numerical results will be presented for the prototypical water/1,2-DCE liquid-liquid interface, using the reparametrized force-field for the organic solvent.

Zusammenfassung

Dielektrische Umgebungseigenschaften sind für viele theoretische Einbettungsmodelle von großer Bedeutung. Darüber hinaus bilden sie die Grundlage für eine Vielzahl von Untersuchungen gelöster Stoffe und katalytisch wirksamer Prozesse in der kondensierten Phase. Speziell im Kontext der Modellierung von Energieumwandlungsprozessen ist hierbei eine realistische und verlässliche Einbettung aktiver Zentren an fest/flüssig oder flüssig/flüssig Grenzflächen essentiell. Besonders die kürzlich gemachte Beobachtung, dass die dielektrische Permeabilität von Flüssigkeiten nahe der Grenzfläche zu einem Feststoff keineswegs konstant ist, sondern vielmehr über mehrere Nanometer stark vom entsprechenden Wert im Inneren der Flüssigkeit abweicht, unterstreicht dabei die Notwendigkeit eines fundamentaleren Verständnisses. Derartige Phänomene sind rein experimentell jedoch schwer zugänglich, sodass deren Untersuchung den Einsatz verlässlicher theoretischer Methoden erfordert.

In diesem Zusammenhang widmet sich die vorliegende Dissertation zunächst einer sorgfältigen Reparametrisierung eines *ab initio*-basierten, nicht-polarisierbaren Kraftfelds zur Beschreibung technologisch relevanter, mit Wasser nicht mischbarer chlorierter Kohlenwasserstoffverbindungen. Für das spezielle Lösungsmittel 1,2-Dichlorethan (1,2-DCE) wird darüber hinaus ein auf Drudes Oszillatormodell basierendes polarisier-

bares Kraftfeld entwickelt und parametrisiert. Hierbei liegt ein besonderes Augenmerk auf der Vermeidung unphysikalischer Kopplungen zwischen den internen Torsionsfreiheitsgraden und den Drude Oszillatoren, da diese die dielektrischen Eigenschaften ernsthaft verfälschen können. Die neuen Kraftfelder werden daher konsequenterweise mit Hilfe umfassender Molekulardynamiksimulationen eingehend untersucht und validiert.

Trotz der Bedeutung der dielektrischen Kontinuumseigenschaften zweier Flüssigkeiten an einer gemeinsamen Grenzfläche haben sich bisherigen Studien hauptsächlich auf Flüssigkeiten direkt an einer statischen fest/flüssig Grenzfläche fokussiert. Flüssig/flüssig Grenzflächen hingegen sind intrinsisch fluktuierend. Dies erfordert im Umkehrschluss eine statistische Analyse zugrunde liegender Molekulardynamiksimulationen, um die dielektrischen Tensorfelder entsprechend zu korrigieren. In diesem Sinne wird ein neuer Ansatz vorgeschlagen, der dielektrische Profile von ähnlicher Abgrenzungsschärfe wie im fest/flüssig Fall erzielt, sofern sich die statistische Auswertung konsistenterweise auf die instantane flüssig/flüssig Grenzfläche bezieht. Dies unterscheidet die hier vorgeschlagene Methode von bisherigen Ansätzen, welche auf der Definition von Durchschnittsgrenzflächen beruhen und entsprechend lediglich verbreiterte, undetaillierte dielektrische Profile über Grenzflächen hinweg erzielen. Die Präsentation entsprechender numerischer Resultate für die prototypische Grenzfläche zwischen Wasser und 1,2-DCE, basierend auf dem zuvor reparametrisierten Kraftfeld, schließt diese Dissertation ab.

Contents

Abstract	v
Zusammenfassung	vii
Contents	ix
1 Introduction	1
2 Theoretical Background	11
2.1 Dielectric Permittivity Tensor	11
2.1.1 Statistical Mechanics Description: Fluctuation Dis- sipation Theorem	13
2.1.2 Continuum Electrostatics Description: Linear Re- sponse	14
2.2 Molecular Dynamics Simulations	16
3 Force Field Reparametrization	21
3.1 Introduction	21
3.2 Theory and Method	26
3.2.1 Nonpolarizable Reparametrization	27
3.2.2 Polarizable Reparametrization	30
3.3 Computational Procedure	34

3.3.1	Simulation of Bulk Liquid Systems	35
3.3.2	Simulation of Liquid-Vapor Interfacial Systems . .	38
3.4	Simulation Details	39
3.5	Result and Discussion	40
3.5.1	Simulation Results Table	41
3.5.2	Dielectric Constants as a Function of Simulation Time and System Size	44
3.5.3	Temperature Dependence of Isothermal Compress- ibility k_T and Dielectric Constant ϵ	47
3.6	Conclusion to Chapter 3	50
4	Intrinsic Liquid-Liquid Interface	55
4.1	Introduction	55
4.2	Theoretical Framework	60
4.2.1	Dielectric Permittivity Tensor	60
4.2.2	Definition of the Intrinsic Interface	61
4.2.3	MD Simulation Details	65
4.3	Results and Discussion	65
4.3.1	Dipole Distribution Profile of LLI	67
4.3.2	Molecular Distribution Profile	69
4.3.3	Parallel Dielectric Permittivity Tensor	70
4.3.4	Molecular Orientation	73
4.3.5	Perpendicular Dielectric Permittivity Tensor	88
4.4	Conclusion to Chapter 4	94
5	Summary & Outlook	97
	Bibliography	101
	List of Figures	122
	List of Tables	129
	Acknowledgements	131

List of Publications

133

Chapter 1

Introduction

A liquid-liquid interface (LLI) arises between two immiscible liquids, generally with water being one of the involved phases. Such an interface constitutes an inhomogeneous environment where the asymmetry in the intermolecular forces yield unique molecular dynamics and structures. The thermodynamic and kinetic processes of molecules at the LLI play a crucial role in electrochemistry, biochemistry, technology and other related fields.[1–5] For example, charged objects such as proteins and lipid membranes embedded in the dielectric environment of water are vastly influenced by the surrounding water.[6] These solvent structure effects with respect to LLI are profoundly depending on the nature of the interface. Molecular level investigation of liquid interfaces hence become the focus of intensive scientific research in the past decades, with many theoretical model simulations studying the dynamics and thermodynamics of chemical reactions at the liquid interface.[7–22] Herein the interfacial water orientations and structures primarily determine the response properties of aqueous interfaces and play an important role in the stability of colloidal suspensions, protein folding and aggregation, and biomolecular recognition.[23–25] This is due to the polar nature of the water molecules that makes water structure strongly modify electrostatic interactions in interfacial systems. The

1. INTRODUCTION

effect of water on electrostatic interactions is quantified by means of the static dielectric permittivity tensor ϵ , which is spatially constant and diagonal in bulk. However, in the vicinity of an interface, the effect of the water is more intricate and strongly depends on the nature of the interface, which especially makes the dielectric permittivity tensor space-dependent.

As an important continuum response property of liquids at a shared interface, the dielectric permittivity sensitively reflects the unique microscopic characteristics in the interfacial region.[26–28] This response property is of fundamental physical importance: on one hand because it is the primary input feature for modeling the electrostatic potential and energies in aqueous environments.[6, 29, 30] Thus a thorough understanding of this property is a key ingredient for the correct modeling of electrostatic effects. For example modeling protein electrostatics requires dielectric properties of the surrounding solvents to be known, as well as the dielectric “constant” of the protein itself which is not a constant but a complex function reflecting the structure and sequence of the protein.[31] On the other hand, the detailed microscopic understanding of phase transfer or catalytic and (photo-) electrochemical processes at complexes embedded in liquid interfaces has to rely heavily on simulations,[32–35] for which the dielectric response of the involved phases is one of the key properties.[36–39] In experiment, terahertz spectroscopy experiments have shown that the dielectric properties of water itself are modified within an interfacial layer of molecular size.[40, 41] As illustrated in Figure 1.1, numerical simulation results even show that the dielectric permittivity of liquids near solid-liquid interfaces is far from being constant, and deviates strongly from the bulk value within several nanometers from the interface. This has raised interest in a more fundamental understanding of the response properties near interfaces.

Despite the importance and widespread interest, simulations of inter-

facial dielectric properties have so far mostly considered the case of confined liquid at a rigid solid/mobile liquid interface.[32–35, 42–47] In contrast, LLIs are known to be intrinsically fluxional in nature,[1, 16] and thus a significant and even more complex estimator for dielectric response analyses. In spite of experimental progress in nonlinear spectroscopic methods such as the vibrational sum frequency generation and second harmonic generation to probe the structure of solid-liquid and liquid-vapor interface systems,[48, 49] very little is known regarding dynamics and mechanisms of the LLI activity. In this case theory plays a pivotal role and can be well complemented by computer simulations.

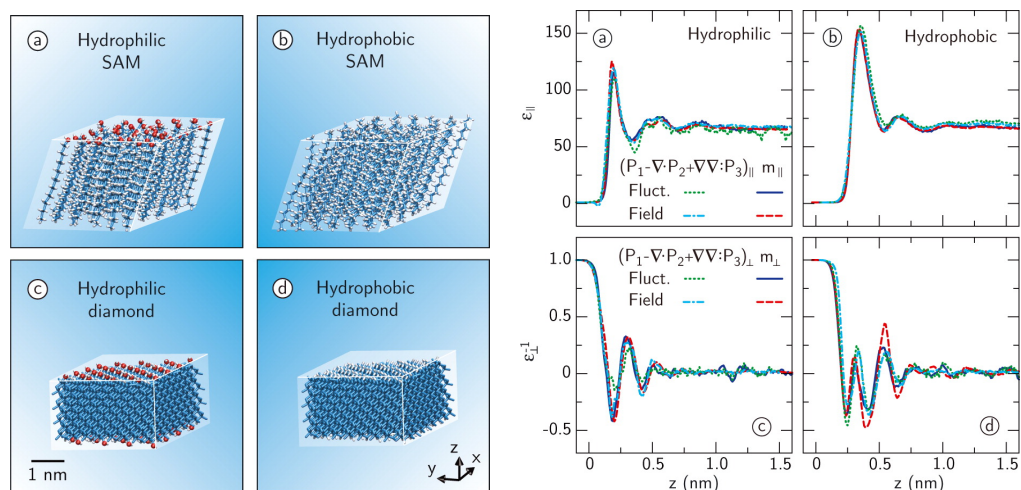


Figure 1.1: Schematic representation of the solid-liquid interface between water and a variety of hydrophobic or hydrophilic substrates (left) with the parallel or perpendicular dielectric response (right). Reprinted with permission from ref. [33]. © 2013 American Chemical Society.

For a physical understanding of the dielectric permittivity, in the macroscopic approach, this dielectric response to an external and static electric field is depending on the dielectric constant of the system. While within microscopic statistical-mechanical theory, that is within framework of linear response theory,[50] the dielectric response

depends on the dipole moment fluctuations in the system. The macroscopic continuum electrostatics and the microscopic statistical-mechanics can be related and present a direct relation between the system's dielectric constant and its dipole moment fluctuations that can be estimated from a computer simulation. Here, to investigate the dielectric response of the LLI system, we apply the statistical-mechanical approach which connects the macroscopic continuum description of the dielectric permittivity to the location fluctuation of the system's dipole moment via a microscopic statistical-mechanical description obtained from MD simulations. This is illustrated in Figure 1.2 with an exemplary MD snapshot of a dipole moment distribution in the LLI system. The local polarization fluctuations are then calculated from a trajectory of such snapshots for a series of separate system-divided slabs parallel to the interface plane along the interfacial normal axis.

It is obvious that a prerequisite of this task is to identify the actual location of the interface at every point. To this end, the vast majority of earlier LLI simulations considered an averaged macroscopic plane parallel to a face of the basic simulation box. This concept of the Gibbs dividing interface plays an important role as a reference point for investigating changes in water properties as a function of the distance to the interface. The Gibbs dividing interface is generally defined as the position where the density of the solvent is half of its bulk value. Once the Gibbs dividing interface is determined, the structural organization and dynamic features of a solvent can be analyzed in consecutive slab-layers parallel to the Gibbs dividing interface. However a LLI actually undergoes dynamic motions. The diffusive motion of molecules in the liquids induces constant perturbations to the instant location of the interface, both in time and spatially across the interface. The static slab-averaging approach has correspondingly been criticized as ignoring this thermal corrugated interface roughness of the interface, known as capillary waves.[9, 51–55] According to capillary wave theory, the

interfacial region includes intrinsic and capillary wave terms.[53, 56–59] The intrinsic component corresponds to the intrinsic profile of the molecular density as a function of distance with respect to the local instantaneous interface. The capillary wave term owes to the thermally corrugated capillary waves broadening the interfacial width. This results in the LLI not being flat but having a time-varying finite roughness.

Thus calculating the response properties relative to the liquid interface, one must remove the effect from capillary waves and evaluate the corresponding intrinsic profile relative to the interface. This is a challenging task as computational protocols to unambiguously identify the fluctuating interface location on a molecular level are only just evolving.[60–62] In MD simulations, different methods have been developed to identify the molecules at the capillary wave fronts of the interface.[58, 59, 63–67] For example, the intrinsic sampling method has been developed to study the intrinsic structure of water/alkane interfaces,[58, 63] whereas the so-called *identification of the truly interfacial molecules* algorithm has been applied to investigate the molecular orientations of water at the vapor and organic interfaces.[64, 65] These approaches mostly focused on combining the capillary wave theory and the molecular view of MD simulations to extract intrinsic profiles such as the density profile and through this identify the interfacial molecules.[58, 63–65]

For the calculations of LLI's response properties with respect to the distance to the instantaneous interface location, the key point of this thesis is to avoid to build upon the continuum capillary wave theory and search for efficient and computationally feasible methods to truly identify the liquid interface. The identification procedure is based on a spatially coarse-grained density field calculated from the atomic coordinates. After determining it, we then reference to this instantaneous interface and describe order phenomena and molecular

1. INTRODUCTION

structure based on the vertical distance from its time-varying position. The construction of the local instantaneous interface follows the ideas by Willard and Chandler.[67] By doing so the spatial deformations of the liquid phase boundary are projected out. Once the instantaneous interface is located, slab-wise analyses are used to bin different regions with respect to the instantaneous LLI to assess various response dynamic and thermodynamic properties associated with the liquid interface such as the density profile, electrostatic potential and dielectric permittivity profile. To elucidate the dielectric response of the interface in more detail, it is essential to analyze to what extent the two involved phases are affected by the presence of the interface. Comparing with molecules within a liquid confined at a solid substrate, the structures at the soft LLI are more complicated due to the instantaneous characteristics of the liquid interface. Detailed knowledge of the molecular orientational profiles with respect to the instantaneous LLI will reveal the subtle proximities of the molecules to the interface that are hidden by the average Gibbs dividing interface, but which are a prerequisite for understanding the mechanism of the interfacial dielectric response.

In this thesis, the LLI system between water and chlorinated hydrocarbons (CHCs) is studied to address some of the questions raised above. CHCs, with one or two carbons and a varying number of chlorine atoms, are rather nonpolar solvents with low boiling points and dielectric constants that are immiscible with water. The LLI of CHCs in contact with a liquid water phase is a particular case for the dielectric analysis because the CHC phase can be “polarized” substantially in the vicinity of the interface by the presence of the water phase. This effect has drawn some attention in theoretical studies.[10, 22, 68, 69] In particular, 1,2-dichloroethane (1,2-DCE) constitutes an interesting prototype molecule, owing to the considerable difference in the dipole moments of its *gauche* and *trans* conformers.[10, 22, 70–75] Both conformers occur in a dynamic equilibrium in the liquid phase of 1,2-DCE and the *trans*

conformer's dipole moment vanishes due to its inversion symmetry. In theoretical studies of mechanical and thermal response properties of the LLI between water and CHCs, MD simulations has already been a reliable tool to understand the dynamics at an atomic level and link the microscopic behavior statistically to macroscopic properties.[76–87] The accurate calculation of thermodynamic and dynamic properties via MD simulations nevertheless depends crucially on the reliability of the employed molecular mechanics force field to describe the nature of the interactions between all components in the simulation system. To this end, currently available models for CHCs have weaknesses in reproducing their dielectric response behavior. Thus we are aiming for strategies to increase the accuracy but without increasing the number of interaction sites to improve the CHC models in the description of the dielectric response.

Part of this thesis work is thus to achieve a careful and balanced first-principles based reparametrization of nonpolarizable (NP) and polarizable molecular mechanics force fields for a class of chlorinated hydrocarbon solvents. In general, for most of the CHCs we limit ourselves to the NP OPLS-AA (optimized potentials for liquid simulations - all atom) type of model, which is sufficiently accurate in modeling a wide variety of the molecular CHC systems. However, the NP models still have an inherent limitation in studying the dielectric constant of nonpolar systems. This comes from neglecting electronic polarizations to account for the dielectric response of the system in the presence of a high-frequency oscillating field, namely the high-frequency or optical dielectric constant ϵ_∞ . [88, 89] For water, the importance of accounting for molecular polarizability in modeling aqueous phenomena has been demonstrated long ago.[90] Incorporating electronic polarization is seen as a major requirement for next generation force fields.[69] Thus for 1,2-DCE we also develop a polarizable force field based on the classical Drude oscillator (DO) model in order to further improve the prediction

1. INTRODUCTION

of the physical properties in comparison to the NP model. The DO model is an efficient tool to account for electronic polarizability without incurring significantly increased computational costs.[91, 92] For the DO model as well as for the NP force field reparametrization, we focus in particular on improved DCE torsional potential energy profiles as compared to quantum chemical (QC) calculations and partial charges based on the RESP fit approach[93, 94] for an improved description of the molecular dipole moments.

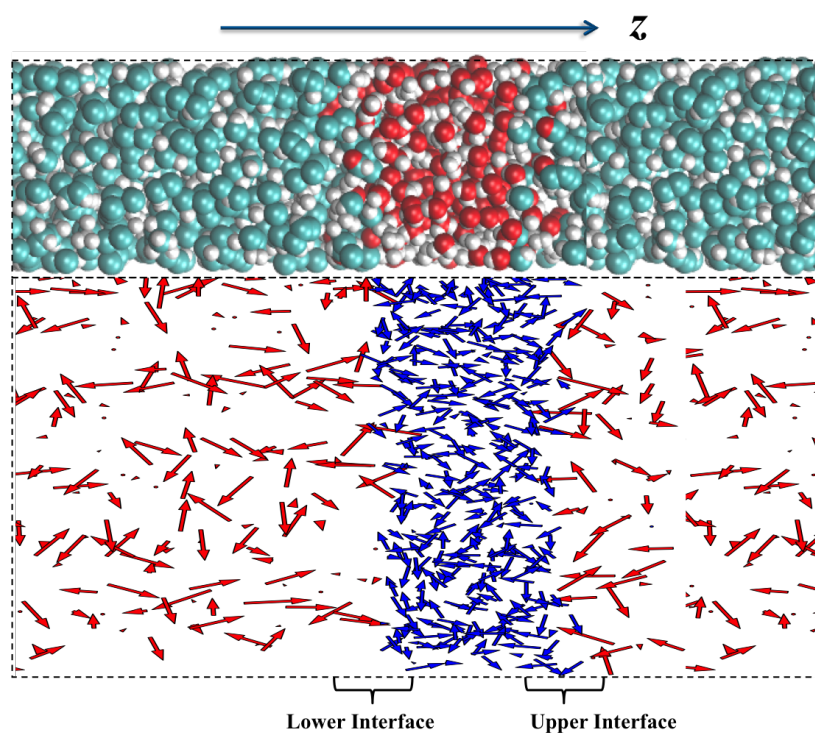


Figure 1.2: Snapshot of an instantaneous equilibrium configuration of the water/DCE interface in the top panel and the representation of the dipole fluctuations of the same simulation snapshot in the bottom panel. Water molecular dipole moments are marked by blue arrows. Red arrows are those of DCE molecules.

The work described in this thesis combines water/1,2-DCE LLI simulations, where the reparametrized NP force field model for the organic

solvent published in Reference [i] is adopted. A computational coarse-grained framework for the determination of the instantaneous LLI locations is implemented, and this advanced interface identification method is used to gain a description of the dielectric permittivity tensor. In Chapter 2, the theoretical framework and computational methods are briefly presented, where the formalisms needed to extract the dielectric tensor from molecular dipole fluctuations are derived step by step. Chapter 3 is concerned with the NP and DO force field parametrization, providing useful and efficient procedures to parametrize effective MM force fields focusing on the reproduction of the dipole moment and distribution and dielectric constants. Implementing the new parameter sets into the classical MD simulations and combining with the statistical procedures from Chapter 2, we present a novel coarse graining approach to analyze MD simulations for the investigation of the dielectric response of the LLI as well as its mechanism in Chapter 4. Chapter 5 contains a summary and outlook.

Chapter 2

Theoretical Background

2.1 Dielectric Permittivity Tensor

The basic idea of the microscopic statistical mechanical theory for the dielectric permittivity of a medium ϵ is to describe its collective response to an applied and uniform electric field in a coarse-grained manner by macroscopic continuum electrostatics.[26–28, 95–98] From the microscopic viewpoint, the response is related to the fluctuations in the system’s dipole moment, which are treated within linear response theory.[50] From the macroscopic continuum viewpoint this same response in the linear approximation is expressed by the dielectric constant. The two expressions can be combined, providing a way to extract the dielectric constant from a computer simulation, connecting the macroscopic continuum description of the dielectric permittivity to the location fluctuations of the system’s dipole moment via a microscopic statistical mechanical description based on MD simulations. For an isotropic bulk system, the dielectric permittivity ϵ^{bulk} can then be determined from the fluctuation of the total dipole moment of the system, as the following equation:[26–28, 95–98]

$$\epsilon^{bulk} = 1 + \frac{4\pi(\langle M^2 \rangle - \langle M \rangle^2)}{3\epsilon_0 V k_B T}, \quad (2.1)$$

2. THEORETICAL BACKGROUND

where M ($= \sum \mu_i$) is the total dipole moment of the simulation cell obtained by the summation over all individual molecular dipole moments μ_i , ϵ_0 is the vacuum permittivity, V is the sample volume and $k_B T$ is the Boltzmann constant. $\langle \dots \rangle$ denotes a statistical average over all different configurations.

In homogeneous and isotropic media ϵ is a scalar, which we call the static dielectric constant, while in an inhomogeneous and anisotropic phase, ϵ becomes a second-rank tensor and depends on the position within the medium.[32–35, 40, 42–47, 99] As an important continuum response property of liquids at an interface, the dielectric permittivity tensor sensitively reflects the unique microscopic characteristics in the interfacial region.[6, 29, 30, 32–35] Yet, a theoretically sound strategy for coarse-graining atomistic simulations of heterogeneous systems towards a continuous dielectric tensor field which unambiguously captures the relevant local interface properties faces quite a few technical challenges. In this work we restrict ourselves to the important but tractable case of an anisotropic LLI system that is nonuniform only along the dimension z , while translational invariance is still preserved in the x and y directions. Thus all response functions such as the electric field and the polarization density only depend on the z coordinates. Maxwell's equation ($\nabla \times \mathbf{E}(z) = 0$) implies

$$\nabla_z E_x(z) = \nabla_z E_y(z) = 0, \quad (2.2)$$

which leads to $E_x(z) = E_y(z) = E_{\parallel}$ and $E_z(z) = E_{\perp}$. The dielectric permittivity tensor becomes diagonal with only two unique components, parallel and perpendicular to the interface[43]

$$\epsilon(z) = \begin{pmatrix} \epsilon_{\parallel}(z) & 0 & 0 \\ 0 & \epsilon_{\parallel}(z) & 0 \\ 0 & 0 & \epsilon_{\perp}(z) \end{pmatrix}. \quad (2.3)$$

2.1.1 Statistical Mechanics Description: Fluctuation Dissipation Theorem

The dielectric constant for a homogeneous isotropic system can be computed by the well-known Kirkwood fluctuation formula, Equ. 2.1. To estimate the dielectric function of the LLI, we consider the microscopic description of the entire simulation box to consist of a collection of slabs parallel to the LLI in which the molecular fluctuations exist.[35, 43, 46] In this case the dielectric permittivity will depend on the correlation between the total system's polarization \mathbf{M} and the local polarization density $\mathbf{m}(\mathbf{r})$ in each statistical slab. For a volume V , $\mathbf{M} = \int_V \mathbf{m}(\mathbf{r}) d\mathbf{r}$. When applying an uniform external field \mathbf{F} , the induced polarization density will be

$$\begin{aligned} \Delta\mathbf{m}(\mathbf{r}) &= \langle \mathbf{m}(\mathbf{r}) \rangle_F - \langle \mathbf{m}(\mathbf{r}) \rangle_0 \\ &= \frac{\int \mathbf{m}(\mathbf{r}) - \langle \mathbf{m}(\mathbf{r}) \rangle_0 \exp[-\beta(U - \mathbf{M}\mathbf{F})] d\tau}{\int \exp[-\beta(U - \mathbf{M}\mathbf{F})] d\tau}, \end{aligned} \quad (2.4)$$

where $\langle \dots \rangle_F$ and $\langle \dots \rangle_0$ denote the statistical ensemble average with and without the electric field \mathbf{F} , β is the inverse temperature, U is the total intermolecular energy and $d\tau$ is the phase space of integration. For a small field \mathbf{F} , we can linearize Equ. 2.4 to obtain

$$\Delta\mathbf{m}(\mathbf{r}) = \frac{\int \mathbf{m}(\mathbf{r}) - \langle \mathbf{m}(\mathbf{r}) \rangle_0 (1 + \beta\mathbf{M} \cdot \mathbf{F}) \exp[-\beta U] d\tau}{\int \exp[-\beta U] d\tau}. \quad (2.5)$$

With the short-hand notation for the ensemble averages, the polarization density becomes

$$\Delta\mathbf{m}(\mathbf{r}) = \beta[\langle \mathbf{m}(\mathbf{r})\mathbf{M} \rangle_0 - \langle \mathbf{m}(\mathbf{r}) \rangle_0 \langle \mathbf{M} \rangle_0] \cdot \mathbf{F}. \quad (2.6)$$

The field \mathbf{F} to which the system responds is constant in space, thus \mathbf{F} is associated with \mathbf{E} depending on the boundary conditions.[35] To simplify the expressions we define the local polarization fluctuation

$$h_{\alpha\beta}(z) = [\langle \mathbf{m}_{\alpha\beta}(z)\mathbf{M}_{\alpha\beta} \rangle_0 - \langle \mathbf{m}_{\alpha\beta}(z) \rangle_0 \langle \mathbf{H}_{\alpha\beta} \rangle_0] \quad (2.7)$$

and the overall polarization fluctuation

$$H_{\alpha\beta} = [\langle M_{\alpha\beta}^2 \rangle_0 - \langle M_{\alpha\beta} \rangle_0^2], \quad (2.8)$$

with $\alpha, \beta = x, y$ or z .

2.1.2 Continuum Electrostatics Description: Linear Response

According to the dielectric linear response,[50] the dielectric permittivity ϵ is based on the linear response of the the local change in the displacement field $D(\mathbf{r})$ to the change in the electric field $E(\mathbf{r}')$. In linear anisotropic media as the LLI system, these two terms are linked via a nonlocal dielectric tensor $\epsilon_{nl}(\mathbf{r}, \mathbf{r}')$ by

$$D(\mathbf{r}) = \epsilon_0 \int \epsilon_{nl}(\mathbf{r}, \mathbf{r}') E(\mathbf{r}') d\mathbf{r}'. \quad (2.9)$$

If we define the local dielectric permittivity $\epsilon(\mathbf{r}) = \int \epsilon_{nl}(\mathbf{r}, \mathbf{r}') d\mathbf{r}'$, for a homogeneous field $E(\mathbf{r}') = E$, Equ. 2.9 leads to

$$D(\mathbf{r}) = \epsilon_0 \epsilon(\mathbf{r}) E. \quad (2.10)$$

With the susceptibility $\chi(\mathbf{r})$, from the linear and local responses[50], the polarization density and total electric field are connected by

$$m_\alpha(\mathbf{r}) = \chi_{\alpha\beta}(\mathbf{r}) E_\beta(\mathbf{r}). \quad (2.11)$$

Since the displacement field $D(\mathbf{r})$ is defined by

$$D(\mathbf{r}) = E(\mathbf{r}) + 4\pi m(\mathbf{r}), \quad (2.12)$$

the dielectric permittivity tensor can be derived as

$$\epsilon_{\alpha\beta}(\mathbf{r}) = 4\pi \chi_{\alpha\beta}(\mathbf{r}) + \delta_{\alpha\beta}. \quad (2.13)$$

The total electric field inside the system is given by the above-mentioned uniform external field F and the induced polarization field due to all sources. That is

$$E(\mathbf{r}) = F(\mathbf{r}) + E^P(\mathbf{r}), \quad (2.14)$$

$$\mathbf{E}_\alpha^P(\mathbf{r}) = \int \Gamma_{\alpha\beta}(\mathbf{r} - \mathbf{r}') \mathbf{m}_\beta(\mathbf{r}') d^3r', \quad (2.15)$$

with the dipole-dipole interaction tensor $\Gamma_{\alpha\beta}(\mathbf{r}) = \frac{1}{r^3}(\frac{3r_\alpha r_\beta}{r^2} - \delta_{\alpha\beta})$. For a periodic system that is nonuniform in only one dimension z , to integrate the dipole-dipole tensor $\Gamma_{\alpha\beta}(\mathbf{r})$, we followed the Refs.[27, 28, 43, 95] via considering the system as a collection of infinitesimally thin and uniformly polarized disks along the z -axis. Thus Equ. 2.15 can be derived as

$$E_\alpha^P(z) = 4\pi(\delta_{\alpha z}[\frac{M_z}{V} - m_z(z)] - \frac{M_\alpha}{3V}). \quad (2.16)$$

During the integration, the electric field is computed using the Ewald summation method, only considering the contribution due to the vacuum boundary conditions, that is under dielectric boundary condition with only the dielectric constant of the vacuum $\epsilon = 1$. Combining Eqs. 2.11, 2.14, and 2.16, the local polarization density can be obtained by

$$m_\alpha(z) = \chi_{\alpha\beta}(z)[F(z) + 4\pi(\delta_{\beta z}[\frac{M_z}{V} - P_z(z)]) - \frac{M_\beta}{3V}]. \quad (2.17)$$

For the response to an external homogeneous electrical field F' , which is not necessarily parallel to the z -axis,

$$\Delta m_\alpha(z) = \chi_{\alpha\beta}(z)[F' + 4\pi(\delta_{\beta z}[\frac{\Delta M_z}{V} - \Delta m(z)] - \frac{\Delta M_\beta}{3V})]. \quad (2.18)$$

Since the LLI system is assumed nonuniform only in the z direction, the susceptibility tensor $\chi(z)$ will be diagonal with the form

$$\chi(z) = \begin{pmatrix} \chi_{\parallel}(z) & 0 & 0 \\ 0 & \chi_{\parallel}(z) & 0 \\ 0 & 0 & \chi_{\perp}(z) \end{pmatrix}. \quad (2.19)$$

By combining the response computed from statistical mechanics (Equ. 2.6, 2.7 and 2.8 in Section 2.1.1) and continuum electrostatics (Equ. 2.18 in Section 2.1.2), we can obtain the relation between the local susceptibility and correlations between the local polarization density

and the total system's dipole moment:

$$h_{\alpha\beta}(z)F' = \chi_{\alpha\beta}(z)[F' + 4\pi(\delta_{\beta z}[\frac{H_{z\gamma}(z)}{V} - h_{z\gamma}(z)] - \frac{H_{\beta\gamma}(z)}{3V})F']. \quad (2.20)$$

Since all tensors \mathbf{H} , \mathbf{h} and χ in Equ. 2.20 are all diagonal, the equations for the individual axes are decoupled. If $E = F'$, i.e. the case without an external field, where the local field is only due to internal dipole fluctuations (e.g. molecular reorientation), we can solve for χ_{\parallel} and χ_{\perp}

$$\chi_{xx}(z) = \chi_{yy}(z) = \chi_{\parallel}(z) = h_{\parallel}(z)(1 - 4\pi\frac{H_{\parallel}}{V})^{-1}, \quad (2.21)$$

$$\chi_{zz}(z) = \chi_{\perp}(z) = h_{\perp}(z)(1 + 4\pi[\frac{H_{\perp}}{V} - h_{\perp}(z)])^{-1}. \quad (2.22)$$

The susceptibilities are related to those of the local dielectric permittivity tensors by $\varepsilon_k(z) = 4\pi\chi_k(z) + 1$, with $k = \parallel, \perp$. For ideal isotropy like in a bulk liquid, the local polarization fluctuation m_k doesn't depend on z anymore, resulting in $h_{xx} = h_{yy} = h_{zz}$ and $\varepsilon_{\perp}(z) = \varepsilon_{\parallel}(z)$, by which we recover Equ. 2.1.

2.2 Molecular Dynamics Simulations

For the work described in this thesis, all-atom classical MD is used to simulate the microscopic dynamics. This is sufficiently acknowledged to quantify the response properties and the molecular structure of the liquid-liquid interface. MD simulations allow us to explore the macroscopic properties of a system of molecules through microscopic level simulations.[100, 101] The macroscopic properties and microscopic simulations are connected via statistical mechanics: Newton's equations of motion (atomic positions and momenta) are integrated numerically and the resulting trajectories analyzed by methods of statistical physics. The basic idea is to compute the system's classical time-evolution, so the system will eventually pass through all possible microscopic states corresponding to a given macroscopic state. Ergodic hypothesis

states that the time averages in statistical mechanics corresponds to the ensemble averages. Many methods exist to perform step-by-step numerical integration; the Verlet algorithm being a common choice.[100, 102] The propagation of the coordinates should fulfill two conditions: (i) accurate calculation of dynamical properties, especially over times as long as typical correlation times Γ_α of properties α of interest; (ii) accurately staying on the constant-energy hypersurface, for much longer times $\Gamma_{run} \gg \Gamma_\alpha$, in order to sample the correct ensemble. It is commonly acknowledged that MD simulations allow a total simulation at time scales of nanoseconds to microseconds for systems of the order of $\sim 10^4$ atoms, which are necessary to converge the fluctuation estimate for the dielectric constant calculation.

At the level of the classical atomic MD approximation, only nuclear degrees of freedom are considered and the motions of the electronic structure are ignored or treated implicitly. According to classical mechanics, MD simulations are based on a classical potential energy function that is parametrizing the quantum ground state potential energy surface due to a given spatial arrangement of the nuclei. In general, such force field includes the contributions of many terms that represent the different types of interactions between the atoms in the system. A typical explicit- or all-atom force field can be written as[100, 101]

$$\begin{aligned}
 V(\mathbf{R}_i) = & \sum_j \frac{k_j^l}{2} (l_j - l_j^0)^2 + \sum_j \frac{k_j^\theta}{2} (\theta_j - \theta_j^0)^2 + \sum_j \frac{1}{2} \sum_{n=1}^6 k_{jn}^\varphi [1 - \cos(n\varphi_j)] \\
 & + \sum_{i,j=1}^N \frac{q_i q_j}{4\pi\epsilon_0 r_{ij}} + \sum_{i,j=1}^N \epsilon_{ij} \left[\left(\frac{\sigma_{ij}}{r_{ij}} \right)^{12} - 2 \left(\frac{\sigma_{ij}}{r_{ij}} \right)^6 \right].
 \end{aligned}
 \tag{2.23}$$

Here the first three sums are bonded (intramolecular) interaction terms – bond stretching, angle bending and torsional rotation contributions to the potential energy. Note that when neglecting the fast electronic

2. THEORETICAL BACKGROUND

degrees of freedom, the molecules are allowed to oscillate, and restoring forces ensure that the system attains equilibrium values of bond lengths and bond angles on average. The torsional profile is related to a set of four connected atom sites, which is usually approximated by a cosine series depending on the dihedral angle φ . The chosen expression applied to cover the torsion rotation throughout this thesis is presented in Chapter 3. The last two sums in Equ. 2.23 constitute nonbonded (intermolecular) interactions – Van der Waals and electrostatic interactions. To represent Van der Waals interactions, the probably most commonly used form is the Lennard-Jones (LJ) 12-6 interaction, where the interaction strength ε_{ij} is the potential well depth and the interaction radius σ_{ij} is the distance at which the potential is 0. To calculate the LJ potential parameters of two dissimilar atom sites, the Lorentz-Berthelot combining rules are adopted in the present work, $\varepsilon_{ij} = (\varepsilon_{ii}\varepsilon_{jj})^{1/2}$ and $\sigma_{ij} = (\sigma_{ii} + \sigma_{jj})/2$. Due to the fact that the LJ potential decays rapidly (r^{-6}) for larger r , the interactions beyond a cut-off radius (general value is $\sim 10 - 15 \text{ \AA}$) can be neglected without losing much accuracy. For the treatment of the slowly decaying Coulomb interaction (r^{-1}), two efficient lattice sum methods approximate the Coulomb interaction beyond the local cut-off radius: the Particle-Particle Particle-Mesh (PPPM) and Ewald summation methods.[98, 103, 104]

The investigation of the mechanical and thermal properties of the simulated system of interest via this empirical approach is crucially dependent on an effective molecular mechanics force field of reliable accuracy to describe all relevant dynamics terms. A vast majority of work correspondingly focuses on the parametrization of classical MD force fields, which faces the challenge of selecting functional forms that are computationally efficient to capture the relevant intra- and intermolecular interactions. Force field parametrization is hence a high dimensional optimization or fitting process and gives rise to the problem that the evaluation of one force field parameter set concerning the

ensemble properties reaches a limit due to the enormous computational cost. The general idea of the parametrization is to perform an empirical calibration of the force field against experimental or first-principle data. Often, this task is complicated by the limited availability of experimental data and a restriction of first-principles data to isolated molecules.

Chapter 3

Force Field Reparametrization

In this chapter, we present a protocol to parametrize force fields for a prototypical class of chlorinated hydrocarbons, which connects the initial reparametrization based on first-principle calculations with classical condensed-phase molecular dynamics simulations for further validation and refinement, with a goal to yield the dielectric constant in good agreement with experimental data. Bulk liquid and liquid-vapor systems are simulated to assess the reparametrized nonpolarizable force field and Drude oscillator polarizable model against results from the common OPLS-AA force field and experimental data. The computed and compared target physical properties include density, isothermal compressibility, thermal expansion coefficient, heat capacity, dielectric constant, heat of vaporization and surface tension. The work described in this chapter is reproduced with permission from Ref. [i]. © 2017 American Chemical Society.

3.1 Introduction

Chlorinated hydrocarbons (CHCs) are a very large and diverse group of organic molecules characterized by their hydrocarbon skeleton with at least one chlorine chemically bonded to it. This class of compounds has

3. FORCE FIELD REPARAMETRIZATION

seen widespread use in numerous application fields that are of great economic, practical, and environmental importance[106, 107] and has hence drawn attention also in theoretical studies. As low-dielectric solvents, CHCs can be “polarized” substantially by a high-dielectric surrounding like water.[10, 22, 68, 69] In particular 1,2-dichloroethane (1,2-DCE) constitutes an interesting prototype model molecule, owing to the considerable difference in the dipole moments of its *gauche* and *trans* conformers.[10, 22, 70–75] This twofold dependence of the dipole moment on its electronic charge deflection and torsion angle potential makes the investigation of the dipole distribution of 1,2-DCE a challenging task when contacting a highly polarizing water phase. In theoretical studies of mechanical and thermal properties of the CHCs, MD simulations have been a reliable tool to understand the behavior of the organic liquids at the molecular level and to link the microscopic behavior statistically to macroscopic properties.[10, 68, 74–87]

The accurate calculation of thermodynamic and dynamic properties of organic systems via MD simulations depends crucially on the reliability of the effective molecular mechanics force field to describe all relevant intramolecular and intermolecular interactions. Nonpolarizable (NP) force fields have been widely used to date and succeed in describing the relevant dynamic terms. This class of force field is also named as additive force field because the point charges are fixed centrally on each of the atomic nuclei. Over the past decades, several additive force fields such as OPLS-AA (Optimized Potentials for Liquid Simulations - All Atom)[81], GAFF (Generalized Amber force field)[82, 83], and CHARMM[85] have been developed for solutes and solvents to model solution systems by MD. For instance the group of Jorgensen[70, 70, 76, 81, 84] showed that the OPLS-AA force field is generally well suited for the simulation of a wide variety of nonaqueous solvents. Coleman et al.[83, 87] presented an extensive MD-based study to provide a force field benchmark for organic liquids comparing the OPLS-AA and

GAFF models. Target properties like density, enthalpy of vaporization, heat capacities, surface tension, isothermal compressibility, volumetric expansion coefficient, and the bulk dielectric constant of a set of organic liquids are compared with experimental data, showing that most properties are in reasonably good agreement, with the notable exception of the dielectric constant which exhibited a rather large deviation from the experimental values. The systematic procedure applied by Frank to parametrize force fields for molecular fluids can achieve correct dielectric constants but only fully rigid MD models are included.[74] While rigid models are computationally more efficient, only flexible force fields will be able to capture the intramolecular dynamics faithfully, which is most probably better suited to simulating the physical and dielectric properties. Hence a class of CHC molecules in this Chapter are represented by the flexible force field, considering all atoms explicitly, which are chloroform (CHCl_3), dichloromethane (CH_2Cl_2), 1,1-dichloroethane (1,1-DCE), and 1,2-dichloroethane (1,2-DCE). For the MD simulations of organic liquids, OPLS-AA force field is regarded as the major force field due to its simplicity and computational efficiency. This force field has already reproduced the thermodynamic, structural and dynamical properties of the CHCs with equivalent levels of detail. Given our current knowledge about the CHCs, however, the original OPLS-AA force field is known to have difficulties in predicting sufficiently correct values of the bulk dielectric constants.[83] The dielectric constant of a medium is a macroscopic concept, which reflects the unique microscopic properties of a material. The systematic improvement of the dielectric constant computed from MD simulations with the reparametrized CHC models is thus one of the key points of this thesis.

NP models, like OPLS-AA, are still commonly used due to the relatively simple potential functions, cheap computational costs and their remarkable success in modeling many molecular systems. In general,

3. FORCE FIELD REPARAMETRIZATION

attempting to improve an efficient force field, we should search for strategies to increase its accuracy without increasing the number of interaction sites.[74, 79, 108] Here, we limit our endeavors to the class of NP force fields for the reparametrization of all CHCs. However, the NP force field has its inherent limitations in the treatment of the electrostatic interactions, because the fixed partial charges make the additive force field incapable of describing the explicit induced polarization experienced by the surroundings. Due to MacKerell et al., NP models in general overestimate the molecular dipole moment from first-principle gas-phase calculation on the order of more than 20%.[109] It is currently common for MD simulations to investigate polar solvents or systems, which respond essentially to the electrostatic fields. The importance of the polarizability in modeling aqueous phenomena has also been demonstrated,[90] which makes electronic polarization a basic requirement in the next generation of force fields.[69] Due to the fact that the NP models for CHCl_3 and CH_2Cl_2 are performing quite well to reproduce the target physical properties, there is no need for an increased model complexity in these cases.[i] We are interested in 1,2-DCE as a prototypical model for the added complexity incurred by a soft internal degree of freedom and the related considerable difference in the dipole moments of its *gauche* and *trans* conformers. Thus we develop a polarizable 1,2-DCE model based on the classical DO model[91, 92] in order to further improve the prediction of the physical properties in comparison with the NP model. The DO model is simply based on the additive force field and keeps the pairwise features of the functional forms, thus without a significant increase of the computational cost.[91, 92] The common strategy for this model to explicitly account for the electronic polarization is to attach a Drude oscillator to its core atom via a harmonic spring to simulate the induced polarization due to the influence of an electric field.

In the present work our goal is via an effective and efficient strategy

to optimize the correct dielectric constants for CHCs. The dielectric constant is mostly related to correct molecular dipole moments and the proper molecular dipole distributions in the condensed-phase from classical MD simulations. Hence the adopted procedure is to optimize the molecular dipole moment by refitting the molecular charge distribution as well as refining the molecular dipole distribution related to the molecular conformational distribution via fitting the molecular torsion potential profiles. We keep the internal (bond and angle) terms the same as in the original OPLS-AA force field. The nonbonded terms in principle are modified and validated from condensed-phase fitting to the experimental data, which is not in the scope of this chapter. Thus for the NP force field reparametrization, we fit the torsion potential energy parameters to the quantum mechanic (QM) calculations and adjust the partial charges based on the RESP fit approach[93, 94] to achieve better agreement with experimental values, focusing on the reproduction of the dielectric permittivity. Regarding the DO model development, we adopt the approach designed by Lamoureux and Roux[91] introducing the polarization to the carbon atom site. Within this approach a self-consistent field (SCF) procedure is avoided by treating the polarizability as an additional classical degree of freedom in the extended Lagrangian mechanics.[110, 111]

This chapter is organized as follows. First, the method to derive the reparametrization is briefly described, followed by the details of the MD simulation. Second, the analysis procedures used to compute the target properties of the improved model are outlined. Third, we present the resulting properties of the improved CHC models and comparisons with available experimental data[112–114] as well as within the framework of the Caleman et al.[83, 87] OPLS-AA force field. The last section gives a conclusion.

3. FORCE FIELD REPARAMETRIZATION

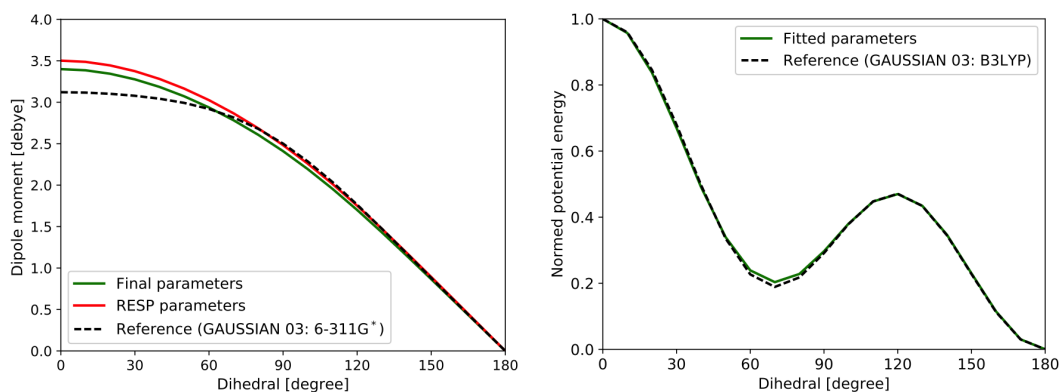


Figure 3.1: Dipole moment (left, dipole profile) and torsional potential energy (right, potential energy profile) of a single 1,2-DCE molecule as a function of its Cl-C-C-Cl dihedral angle. The quantum chemical reference of the dipole profile is calculated with GAUSSIAN 03 using the 6-311G* basis set.[115] The quantum chemical reference of the potential energy profile is calculated with GAUSSIAN 03 at B3LYP aug-cc-pVDZ level.[115] The potential energy of the most stable conformer is set to zero.

3.2 Theory and Method

The OPLS-AA force field by Coleman et al.[83, 87] is used as a starting point for our reparametrization. The standard bond stretching, angle bending and nonbonded Lennard-Jones parameters are initially assigned from the OPLS-AA. The present work then focuses on the improvement of the torsional angle coefficients (where applicable) and atomic partial charges within the flexible NP force field. The objective is to produce simple and efficient OPLS-AA type CHC models that yield improved bulk dielectric constants while at least retaining or possibly improving the computed values for all other relevant physical properties of the solvents. The same approach is then followed to parametrize a polarizable model for 1,2-DCE (1,2-DCE-DO, "DO" for Drude oscillator), now including polarizable carbon atoms to further improve molecular bulk properties. As target properties of the liquids besides the bulk dielectric constant, we focus on equilibrium values for the density, heat

capacities, isothermal compressibility, and the volumetric expansion coefficient. Properties of the CHC liquid-vapor interfaces such as the heat of vaporization and surface tension are evaluated in addition. All calculated results are compared with the available experimental data collected in Table 3.4.

3.2.1 Nonpolarizable Reparametrization

Atomic Charges

The atomic partial charges for the different interaction sites are fitted using the RESP method.[93, 94] The molecular electrostatic reference potential is computed using GAUSSIAN 03 with the 6-311G* basis set[115], in order to be in line with the original parametrization of the OPLS force field[81]. For 1,2-DCE-NP reparametrization, the short MD trajectories, which adopt the initial RESP atomic charge distributions, reveal an overestimation of the *gauche* population. This comes from the increased electric field caused by the overestimated *gauche* dipole moment. Thus the atomic charges of 1,2-DCE need a refitting to achieve better agreement with the respective dipole moment profile as a function of the Cl-C-C-Cl torsion angle. For this purpose, the negative charge of the 1,2-DCE-NP carbon is slightly increased (-0.0075) while the charge of the chlorine is slightly decreased (+0.0075), which result in the *gauche* conformer model of the 1,2-DCE-NP having a lower over-all dipole moment. The left panel of Figure 3.1 illustrates the calculated dipole moment profile of 1,2-DCE as a function of the Cl-C-C-Cl dihedral angle using the initial RESP charge sets and the final refitted partial charges in comparison with the first-principle reference profile, which demonstrates the conformational geometry dependence of the molecular dipole moment. The large deviation of the *cis* regime (0-30°) with respect to the first-principle reference has slight impact on the liquid simulations, since the relevant high potential energy

3. FORCE FIELD REPARAMETRIZATION

barrier almost completely prevents the population of this conformer.[73] The same charge modification is applied to the two different carbon atoms of the 1,1-DCE model. That is slightly increasing the charge split of the bond between the two carbons with the same value used in the C-Cl charge split of 1,2-DCE but without further fitting, in order to increase its over-all dipole moment and the dielectric constant. For CHCl_3 , the carbon charge is set to zero to avoid the artificial behavior. Additionally, the models for CHCl_3 and CH_2Cl_2 with the plain RESP[93, 94] charges do not represent the target properties well enough, requiring slight adjustments of the atomic partial charges based on short MD simulations to achieve better agreement with the experimental values. The final atomic charges for all interaction sites of the CHCs are collected in Table 3.1.

Torsion Potential Parameters

After fitting the atomic charges, the torsion potential parameters are optimized to reproduce the exact energy profiles based on the quantum mechanical calculations. For 1,1-DCE and 1,2-DCE using OPLS-AA force field, the torsional potential energy profiles depending on dihedral angles, φ_i , are described by cosine series of the Fourier form[76]

$$E_{torsion} = \sum_i \left[\frac{1}{2} V_{1,i} (1 + \cos \varphi_i) + \frac{1}{2} V_{2,i} (1 - \cos 2\varphi_i) + \frac{1}{2} V_{3,i} (1 + \cos 3\varphi_i) + \frac{1}{2} V_{4,i} (1 - \cos 4\varphi_i) \right]. \quad (3.1)$$

In order to make the transferability of the torsion potential parameters, we just fit a parameter set for each dihedral angle both work for 1,1- and 1,2-DCE. Here taking the 1,2-DCE as an example, its torsional interaction is reproduced by a total of 12 torsion parameters $V_{k,i}$. Since it is not possible to isolate one single $V_{k,i}$ to evaluate its impact on the potential energy of the different configurations, the execution of a

decoupled and consecutive fitting process is not readily possible. Thus the fitting process turn out to be a high-dimensional situation, resulting in the simple optimization methods to be unsuitable. The differential evolutionary algorithm (DEA) is hence adopted in this chapter. This optimization method is widely used due to its simplicity and success in tackling high-dimensional problems.[116] Different from other generic evolutionary algorithms, the efficiency of the DEA is focused on the steps to generate the trial vector to make sure it contains as least one initial parameter. Details should go to the References [116] and [117]. The torsion parameters $V_{k,i}$ are fitted to the quantum chemical energy profiles using the DEA included in the Python package INSPYRED 1.0[117] with a goal to minimize the difference of those from the classical MD calculations. The torsional cut through the quantum chemical reference potential energy surface is evaluated at 19 different 1,2-DCE conformer geometries with GAUSSIAN 03 at the B3LYP-aug-cc-pVDZ level[115], scanning the respective dihedral angle from 0 to 180 degrees with the rest parts of the molecule kept fixed during the scan. This torsional potential energy profile is showed in the right panel of Figure 3.1. For a molecule in *gauche* configuration, its dihedral angle is characterized by an interval from 30 to 90, while a molecule with dihedral angle between 150 and 210 is declared *trans*. From the figure, it can be seen that the fitted parameter set reproduce the accurate of the potential energy from first-principle computations, where it is worth noticing that the calculated activation energy of torsion angle rotation from *gauche* to *trans* ($E_A = 10.100kJmol^{-1}$) is in agreement with other theoretical studies applying the same level of first-principle calculations.[118, 119] This energy difference is considered to be larger than the thermal energy at the room temperature ($k_B T N_A = 2.479kJmol^{-1}$)[73], making the conformational conversion a rare event. Thus for each of the target conformer geometries a single molecule MD simulation is conducted, progressively cooling down the system

while simultaneously restraining the respective dihedral angle and eventually extracting an effective torsional potential energy value for the respective conformer. The conformer geometries are further weighted properly to keep the focus on the two main conformers (*gauche* and *trans*) and the relative height of the lower one of the two rotational energy barriers. This protocol is also applied for the polarizable model development in order to keep the two fittings on equal footing. Out of an ensemble of parameter sets generated by this protocol with comparable fit quality for the energy profile, the one set is chosen that reproduces the experimentally observed *trans/gauche* ratio best within an MD simulation. The resulting numerical coefficients for this torsion potential energy are listed in the Table 3.2.

3.2.2 Polarizable Reparametrization

A majority of molecular mechanics force fields for MD simulations are based on additive force field where the partial charges are fixed to each atom. As mentioned above, however, these NP models are not capable of fully capturing the molecular response to external fields due to their lack of a polarizable electron density. Thus more complex force fields are needed to adapt the charge distribution to overcome the limitation. One way to take the explicit electronic polarization into account approximately is given by the Drude oscillator model.[69, 89, 120–122] This model accounts for the induced polarization by introducing an almost massless Drude particle (DP) that is harmonically attached to a massive core (DC). The sum of the masses of the DC-DP pair should equal the mass of the modeled atom. Analogously, DC and DP carry different partial charges summing up to the charge of the target atom. The positions of these particles are relaxed into their local minimum energy position in a self-consistent field (SCF) manner, which has to be solved at each MD time step, making the computational cost increase noticeably.[91] What makes the DO model

Table 3.1: Atomic charges for the interaction site of the chlorinated hydrocarbon molecules. q denotes the atomic charge. Reproduced with permission from ref. [i]. © 2017 American Chemical Society.

Molecules	Interaction site	$q(e)$
CHCl ₃	C	0.0000
	H	0.2100
	Cl	-0.0700
CH ₂ Cl ₂	C	-0.2140
	H	0.2075
	Cl	-0.1005
1,1-DCE	C(H ³ C-)	-0.1615
	H(CH ³ -)	0.0950
	C(Cl ² HC-)	-0.0525
	H(Cl ² CH-)	0.1920
	Cl	-0.1315
1,2-DCE-NP	C	-0.0515
	H	0.1160
	Cl	-0.1805
1,2-DCE-DO	DC	2.1911
	H	0.1160
	Cl	-0.1805
	DP	-2.2426

3. FORCE FIELD REPARAMETRIZATION

computationally tractable in MD simulation is the treatment of the Drude oscillators as classical dynamic variables in the context of the extended Lagrangian methods.[110, 111] This is achieved by allocating a small mass m_D to the DP from the initial atom and applying separate thermostats to the relative motion of the DPs around their DCs and the center of mass of the DC-DP pairs.[110, 111] In the current model with a polarizable carbon, m_D is chosen to be small, $m_D = 0.4g/mol$, and the force constant k_D of the harmonic restoring potential is set to be quite large, $k_D = 4180kJ/mol/\text{\AA}^2$, for all Drude oscillators in order to maintain the kinetic decoupling of the DC-DP pair motion. In addition, two separate Langevin thermostats are applied to thermalize the reduced degrees of freedom of the Drude oscillators to keep the atomic system close to the chosen temperature and the degrees of freedom of the DP at 1 K.[110, 111] The recent implementation of *Thole* atomic damping in the Large-Scale Atomic/Molecular Massively Parallel Simulator (LAMMPS) simulation package is used to reduce the short-range attraction of the respective Drude-core-atom interaction, where the parameter l_i is set to the suggested value of 2.6 \AA for all simulations.[92] The reparametrization procedure for the development of the 1,2-DCE DO model also focuses on improving the molecular dipole moment by refitting the partial charges through the polarizability and the resulting *trans/gauche* distribution by optimizing the torsional parameters.

Atomic Polarizability

A direct determination of the Drude charges via RESP fitting is not meaningful. Instead, the charge split is determined by means of the respective atomic polarizability α which is related to the force constant k_D and the Drude charge q_D by

$$\alpha = \frac{1}{2} \frac{q_D^2}{k_D}. \quad (3.2)$$

The 1,2-DCE molecule is built from two equivalent CH₂Cl subgroups, contributing equally to the total polarizability. Not taking into account the hydrogen atoms as potential polarization sites, the DO model development in this study considers either the carbon or the chlorine of each CH₂Cl subgroup as polarizable sites. It is worth noticing that the DO model that assigned the polarizability to the chlorine atoms completely fails to reproduce the correct dielectric constant of bulk 1,2-DCE, with a computed $\epsilon = 20.39$, and exhibits a strong coupling between the DO degrees of freedom and the torsion. The experimental atomic polarizability $\alpha = 1.67\text{\AA}^{-3}$ is thus assigned to the carbon atom sites.[113] The resulting partial charges for the different interaction sites of the 1,2-DCE-DO are collected in Table 3.1.

Torsion Potential Parameters

It is common that the reference is not directly from first-principle calculations. According to Justin et al.[123], the Drude oscillator model developing approach contains model choices which are based on experience, for example they arbitrarily used a tunable parameter with the related atomic polarizability to achieve significantly better result during empirical optimization. Herein our approach is to minimize the changes needed to go from the well-performing NP model to the polarizable version. Thus a slightly modified approach to fit the dihedral parameter is applied to the polarizable model with the already fitted 1,2-DCE-NP model as a starting guess. It is important to mention that even though the potential energy profile for a single molecule might be reproduced correctly, the final conformational distribution can still varies to a large extent for the resulting condensed phase. Thus an additional modification of the dihedral parameters based on a set of MD simulations proves necessary for a proper reproduction of the conformational *trans/gauche* ratio. For the final set of parameters the obtained average dipole moment is close to the quantum chemical

3. FORCE FIELD REPARAMETRIZATION

reference.[73] The refitted dihedral parameters with the established partial charge set that can provide the proper reproduction of the conformational distribution in the bulk liquid simulation are selected. They are listed in Table 3.2.

Table 3.2: Coefficients of the torsion potential energy for 1,1-DCE and 1,2-DCE. Reproduced with permission from ref. [i]. © 2017 American Chemical Society.

Molecules	Dihedral angle	V_1	V_2	V_3	V_4
1,1-DCE	H-C-C-H	1.5000	0.2960	0.1910	0.1080
	H-C-C-Cl	0.2300	0.9120	0.3590	0.0000
1,2-DCE-NP	H-C-C-H	1.5000	0.2960	0.1910	0.1080
	H-C-C-Cl	0.2300	0.9120	0.3590	0.0000
	Cl-C-C-Cl	1.4490	0.4960	0.1270	0.0000
1,2-DCE-DO	H-C-C-H	1.5000	0.0000	0.1603	1.2498
	H-C-C-Cl	0.6960	0.6973	0.2454	0.6100
	Cl-C-C-Cl	1.5000	0.2546	1.0054	0.0614

3.3 Computational Procedure

After equilibration, production MD simulations are performed to compute thermodynamic and dynamic properties for all optimized models of the CHCs: CHCl_3 , CH_2Cl_2 , 1,1-DCE and 1,2-DCE, in order to assess the quality of the reparametrized force fields. The evaluated properties are density, volumetric expansion coefficient, isothermal compressibility, constant volume and pressure heat capacity, dielectric constant, heat of vaporization and surface tension. Two sets of simulations are thus required, corresponding to a “bulk liquid” system and a “liquid-vapor” system for each CHC. The remaining details for the bulk liquid and

liquid-vapor simulation sets are given in the following paragraphs.

3.3.1 Simulation of Bulk Liquid Systems

For the equilibrium properties of each CHC, we prepare five independent bulk liquid systems. The lengths of the X , Y , Z edges of the cuboid simulation box are 22, 22, and 68 Å, respectively. The simulation cells contain 248 CHCl_3 , 312 CH_2Cl_2 , 244 1,1-DCE, 252 1,2-DCE-NP, and 252 1,2-DCE-DO molecules to reproduce bulk densities of the respective liquids at room temperature. The settings for the bulk liquid simulations are given above.

Density ρ

An average density $\rho = M_T / \langle V \rangle$ is obtained from additional 1 ns constant pressure simulations after the equilibration phase for each CHC. Densities are collected every 0.1 ps by monitoring the instantaneous volume V with the total mass M_T . Here and in the following, the $\langle \dots \rangle$ denotes a statistical average over different configurations of the system.

Volumetric Expansion Coefficient α_p , Isothermal Compressibility k_T , Heat Capacity C_p and C_v

We use the fluctuations in the NPT ensemble to calculate the volumetric expansion coefficients α_p , isothermal compressibility k_T and heat capacity C_p at constant pressure for all CHCs. For the calculations of α_p , k_T , and C_p , additional NPT simulations are performed after equilibration at different temperatures T for all CHCs. Each simulation is run for 1 ns, sampling the target properties every 0.1 ps during these production runs. For the computation of the target properties from fluctuations, we

3. FORCE FIELD REPARAMETRIZATION

refer to Ref.[101] using the following equations:

$$\begin{aligned}
 k_T &= \frac{1}{k_B T \langle V \rangle} (\langle V^2 \rangle - \langle V \rangle^2)_{NPT} \\
 \alpha_P &= \frac{[\langle V \cdot U \rangle - \langle V \rangle \cdot \langle U \rangle + P(\langle V^2 \rangle - \langle V \rangle^2)]_{NPT}}{k_B T^2 \langle V \rangle} \\
 C_P &= \frac{ik_B N}{2} + \frac{1}{k_B T^2} [(\langle U^2 \rangle - \langle U \rangle^2) + 2P(\langle V \cdot U \rangle - \langle V \rangle \cdot \langle U \rangle) \\
 &\quad + P^2(\langle V^2 \rangle - \langle V \rangle^2)]_{NPT},
 \end{aligned} \tag{3.3}$$

with temperature T , pressure P , volume V , Boltzmann constant k_B , the potential energy U , the number of molecules N , and the number of degrees of freedom i . Since none of the CHC molecules are restraint, we have $i = 6$. To evaluate the constant volume heat capacity C_V , additional NVT simulations are performed after equilibration at temperature T for all CHCs. Each system is simulated for 1 ns and samples are collected every 0.1 ps. The constant volume heat capacity C_V is calculated from the fluctuations in the NVT ensemble:

$$\begin{aligned}
 C_V &= \frac{ik_B N}{2} + \frac{1}{k_B T^2} [(\langle U^2 \rangle - \langle U \rangle^2) + 2P(\langle V \cdot U \rangle - \langle V \rangle \cdot \langle U \rangle) \\
 &\quad + P^2(\langle V^2 \rangle - \langle V \rangle^2)]_{NVT}.
 \end{aligned} \tag{3.4}$$

Dielectric Constant ϵ

The static dielectric constant, ϵ , is related to the fluctuations of the system's total dipole moment M in the computational box. Here we take into account the contribution from the high-frequency dielectric constant when calculating the static dielectric constant. Thus, the dielectric constant can be determined from the following fluctuation formula[88, 89, 95],

$$\epsilon = \epsilon_\infty + \frac{4\pi \langle M^2 \rangle - \langle M \rangle^2}{3 \epsilon_0 V k_B T}. \tag{3.5}$$

Here ϵ_∞ denotes the high-frequency or optical dielectric constant,[88, 89], V is the volume of the simulation box, k_B is the Boltzmann constant and M is the dipole moment of the total simulation cell. The high-frequency optical dielectric constant ϵ_∞ relates to the molecular polarizability,[88, 124]which can be measured from the classical fluctuations of induced dipoles of the simulation box. Here we adopt the procedure proposed by Lamoureux et al.[88, 89] that is estimating the ϵ_∞ from the dipole fluctuations of the system only refer to the movement of the Drude oscillators, through regularly extracting the fixed nuclear configurations from MD simulations according to Langevin dynamics at temperature 1 K as for the low-temperature thermostat used in the extended Lagrangian MD simulations:

$$\epsilon_\infty = 1 + \frac{4\pi}{3} \frac{\langle M^2 \rangle_{(f)} - \langle M \rangle_{(f)}^2}{\epsilon_0 V_{(f)} k_B T}. \quad (3.6)$$

$\langle \dots \rangle_{(f)}$ indicates an average over induced-dipole fluctuations only. After performing this equation to dozens of configurations of the system, the high-frequency ϵ_∞ is calculated with a value of 1.54. For NP model ϵ_∞ is set to 1 since no electronic degrees of freedom are explicitly modeled in this case. Thus Equ.3.5 covers both standard and polarizable models that is covering both the low-frequency and high-frequency dielectric constant of a system. The system's total dipole moment M ($= \sum \mu$) is obtained by the summation over all molecular dipole moments in the simulation cell. As it has been observed before[83, 125, 126], the fluctuation term ($\langle M^2 \rangle - \langle M \rangle^2$) tends to converge quite slowly (see below). Thus 12 ns long simulations in the microcanonical (NVE) ensemble are carried out to ensure that the computed values are well converged, treating the initial 2 ns as equilibration, with the following 10 ns used to record 10001 sample configurations at an interval of 1 ps for analysis.

Table 3.3: Sizes of the cubic liquid-vapor simulation boxes for the different CHC systems, only showing the edge length in the X dimension. Each system contains $N = 1000$ molecules. Reproduced with permission from ref. [i]. © 2017 American Chemical Society.

System	CHCl ₃	CH ₂ Cl ₂	1,1-DCE	1,2-DCE-NP	1,2-DCE-DO
$X(\text{Å})$	52.0	49.0	52.5	51.5	51.5

3.3.2 Simulation of Liquid-Vapor Interfacial Systems

The liquid-vapor interfacial systems are more complex to simulate in comparison to the bulk systems. Additionally, the surface tension is a property well-known to be rather problematic to reproduce with an NP force field.[127, 128] For the calculation of the liquid-vapor interfacial systems, five cubic simulation systems containing 1000 molecules are prepared respectively. The lengths of the cubic edge of the respective simulation boxes are summarized in Table 3.3. These lengths are selected to reproduce the same densities of the liquids as in the above bulk liquid simulations at room temperature. To obtain the liquid-vapor interfaces, the size of each simulation box in the Z direction is extended by a factor of 4, creating vacuum regions at the top and bottom side (periodic boundary conditions) of the CHC slabs. This generates a system with two liquid-vapor interfaces parallel to the XY -plane. Each system is simulated for 5 ns, with the initial 4 ns treated as the equilibration phase. During the final nanosecond, samples are collected for the target properties every 0.1 ps. All simulations are run in the NVT ensemble using a larger cut-off radius $r_c = 15 \text{ Å}$. All other settings are consistent with the above simulation details.

Heat of Vaporization ΔH_{vap}

The heat of vaporization ΔH_{vap} can be calculated from the difference between the potential energy of an ideal gas and the liquid state. Without considering additional corrections, the simplest approximation is given by $\Delta H_{vap}(T) \approx (H_{gas} - H_{liq})/N + RT^3$, with H_{gas} and H_{liq} being the potential energy of the N molecules in gas phase and liquid phase, respectively, and R being the gas constant. H_{gas} is taken from the potential energy of N molecules in a gas phase simulation while H_{liq} is deduced from the potential energy of each system in the liquid-vapor simulation.

Surface Tension γ

The surface tension is computed from the pressure tensor following the mechanical method of Kirkwood and Buff[129] by the integration of the difference between the normal pressure-tensor component $P_n(z) = P_{zz}(z)$ and tangential components $P_t(z) = (P_{xx}(z) + P_{yy}(z))/2$ along the z direction (perpendicular to the liquid-vapor interface). The resulting formula reads $\gamma(t) = L_z/2(P_z(t) - (P_x(t) + P_y(t))/2)$, where P_n is the pressure tensor in the direction n and L_z is the length of the simulation region along the z direction.

3.4 Simulation Details

All simulations are carried out by classical molecular dynamics using the LAMMPS simulation package.[130] The intermolecular interaction potential used in this study is Lennard-Jones (LJ) site-site potentials plus Coulomb interactions. The standard Lorentz-Berthelot rules, $\epsilon_{ij} = (\epsilon_{ii}\epsilon_{jj})^{1/2}$ and $\sigma_{ij} = (\sigma_{ii} + \sigma_{jj})/2$, are used to derive the LJ potential parameters between unlike atom-types, where ϵ_{ij} and σ_{ij} are the energetic and size parameters of the LJ interaction between sites i and j , respectively. The nonbonded LJ interactions are treated using a

regular spherical cut-off (cut-off radius $r_c = 10\text{\AA}$) while the long-range Coulomb interaction is evaluated using the Ewald[103, 104] summation method with a relative error of 10^{-6} . During the entire simulation, periodic boundary conditions (PBC) are applied in all three directions. The integration time step is 1 fs. After initial energy minimization to remove unfavorable interactions, all atoms in each system are randomly assigned initial velocities based on a gaussian distribution to produce the desired simulation temperature. Then each system is equilibrated for 1 ns in the canonical (NVT) ensemble and subsequently for 3 ns in the isothermal-isobaric (NPT) ensemble at 1 atm and 298.15 K. Analysis programs are either taken from the *Pizza.py* toolkit[131] or written in-house.

3.5 Result and Discussion

In the following, the equilibrium properties, including density, volumetric expansion coefficient, isothermal compressibility, heat capacity, dielectric constant, heat of vaporization, and surface tension obtained from the above-described MD simulations are presented. The models from the present work are labeled as OPLS-NP and OPLS-DO to indicate either the standard nonpolarizable or polarizable Drude oscillator models reparametrized based on the original OPLS-AA force field. Table 3.4 compares the above physical properties of the CHCs compute using our new models with values obtained from the original OPLS-AA force field by Caleman et al.[83, 87], here labeled as OPLS, and also with experimental data[112–114]. As already mentioned, the statistics entering the dielectric constant are not easily converged and require simulations on the nanosecond time scale. We evaluate the dielectric constant as a function of simulation length for the CHC models (see Section 3.5.2). To control the influence of the system size on the dielectric constant, we additionally calculate ϵ from three independent simulations

with varying numbers of molecules for 1,2-DCE-NP and 1,2-DCE-DO, respectively. The results are identical to the values given in the table for the smaller systems. To extend the range of the applicability of our force field model, we also compute the isothermal compressibility and dielectric constant not only at room temperature but as a function of the temperature for this class of the CHCs (see below).

3.5.1 Simulation Results Table

To clearly show the better performance of our new reparametrized models in producing the physical properties, we plot the deviations of the target properties calculated using our new parameter sets and the original OPLS force field with respect to the experiment data in Figure 3.2. All the used values can be found in Table 3.4. As Table 3.4 and Figure 3.2 show, the results obtained with our reparametrized models are in overall good agreement with the available experimental data. Our reparametrization leads either to an improved agreement with a range of experimental properties, or matches them roughly equally well as the previous OPLS-AA models. Additionally, it is important to stress that for the dielectric constant and surface tension, the reparametrized models reproduce the experimental value much more accurately than the original OPLS-AA force field. The improvement of the dielectric constants is achieved by assigning improved atomic partial charges yielding better agreement with the respective molecular dipole moments and, for the more flexible molecules, a more accurate conformational distribution obtained by the reparametrization of the torsion potential coefficients.

We obtain 32.3% and 30.8% of *trans* conformer for 1,2-DCE-NP and 1,2-DCE-DO model, respectively, which are consistent with the experimental value of 34.9%[132] and in good agreement with an ab initio MD calculation (32.2%)[73]. Both new models clearly outperform the

Table 3.4: Properties of CHCs with the improved force field models. ρ , ΔH_{vap} , r , ϵ , α_P , k_T , C_V and C_P denote the density, surface tension, relative dielectric constant, volumetric expansion coefficient, isothermal compressibility, heat of vaporization, constant volume heat capacity and constant pressure heat capacity at 298.15 K. OPLS-NP is the new non-polarizable model which is directly comparable to the standard OPLS (all atom) parametrization. OPLS-DO denotes the polarizable model (see text for details). ^a Reference [112]. ^b Reference [113]. ^c Reference [114]. ^d For the polarizable model $\epsilon_\infty = 1.54$ is determined according to the procedure from refs [88] and vorobyov2005polarizable. Reproduced with permission from ref. [i]. © 2017 American Chemical Society.

Liquid	Model	ρ (g/cm ³)	ΔH_{vap} (kJ/mol)	r (0.001N/m)	ϵ (0.001/K)	α_P (1/GPa)	C_V (J/mol/K)	C_P (J/mol/K)
CHCl ₃	OPLS-NP	1.40	24.13	24.34	4.33	1.70	76.80	121.35
	OPLS	1.37 ^a	29.20 ^a	11.8 ^a	3.3 ^a	2.28 ^a	89.6 ^a	113 ^a
	Expt.	1.48 ^b	31.28 ^b	26.67 ^c	4.71 ^c	1.29 ^b	116.98 ^b	117.00 ^b
CH ₂ Cl ₂	OPLS-NP	1.20	20.64	21.62	8.85	1.85	78.40	120.19
	OPLS	1.21 ^a	23.36 ^a	10.5 ^a	4.4 ^a	2.31 ^a	75 ^a	53.5 ^a
	Expt.	1.32 ^b	28.82 ^b	27.20 ^c	8.82 ^c	1.35 ^b	100.86 ^b	100.88 ^b
1,1-DCE	OPLS-NP	1.13	28.85	20.71	10.02	1.69	124.43	168.45
	OPLS	1.18 ^a	28.29 ^a	15.1 ^a	3.2 ^a	1.60 ^a	100.7 ^a	64 ^a
	Expt.	1.17 ^b	30.62 ^b	24.07 ^c	10.10 ^c	1.33 ^b	126.18 ^b	126.20 ^b
1,2-DCE	OPLS-NP	1.16	29.66	27.57	10.79	1.31	126.84	164.96
	OPLS-DO	1.21	31.31	29.95	14.01 ^d	1.45	132.68	181.70
	OPLS	1.24 ^a	35.08 ^a	23.2 ^a	13.4 ^a	1.43 ^a	106.7 ^a	78 ^a
Expt.	1.25 ^b	35.16 ^b	31.86 ^c	10.13 ^c	1.15 ^b	128.88 ^b	128.90 ^b	

original OPLS-AA force field in this respect, which results in 9.7%. The most notable properties, which are not improved over the standard OPLS-AA and are still off the experimental values in the NP models, are the density and the heat of vaporization, which might be the price to pay for improving the dielectric performance. There seems to be a clear trade-off for what can be achieved with a NP model, where we opt for a rather balanced treatment of important solvent properties. Some improvement with respect to the underestimated density might also be possible using larger simulations thus reducing statistical fluctuations and possible PBC effects. It is also noted that nonideal gas corrections in the estimates of the heat of vaporization might improve the agreement with experiment. In both cases we adopt a more conservative approach (e.g. traditional approximation in Section 3.3.2 for ΔH_{vap}) to render our results more easily comparable with former parametrizations.

The introduction of polarizable sites, which increase the flexibility of the respective model, could improve the density and thermal compressibility since both long-range attraction and short-range repulsion are influenced by the additional Coulomb potential terms.[133] The density ρ and thermal compressibility k_T obtained within the 1,2-DCE-DO model are indeed noticeably improved over the 1,2-DCE-NP model, illustrating the expected correlation of these two properties and confirming the assumption that the introduction of the polarizability would yield improved ρ and k_T . For the liquid-vapor interfacial simulations of 1,2-DCE, the Drude oscillator model also leads to a significant improvement of agreement with experiments for quantities ΔH_{vap} and r , compared to 1,2-DCE-NP model without losing the agreement for other properties. The heat capacities C_P and C_V are hardly influenced, showing that no energy is artificially deposited in the degrees of freedom modeling the electronic polarizability. The dielectric constant ϵ of 1,2-DCE obtained with the OPLS-DO model is in general agreement with the experimental reference, however not as good as

3. FORCE FIELD REPARAMETRIZATION

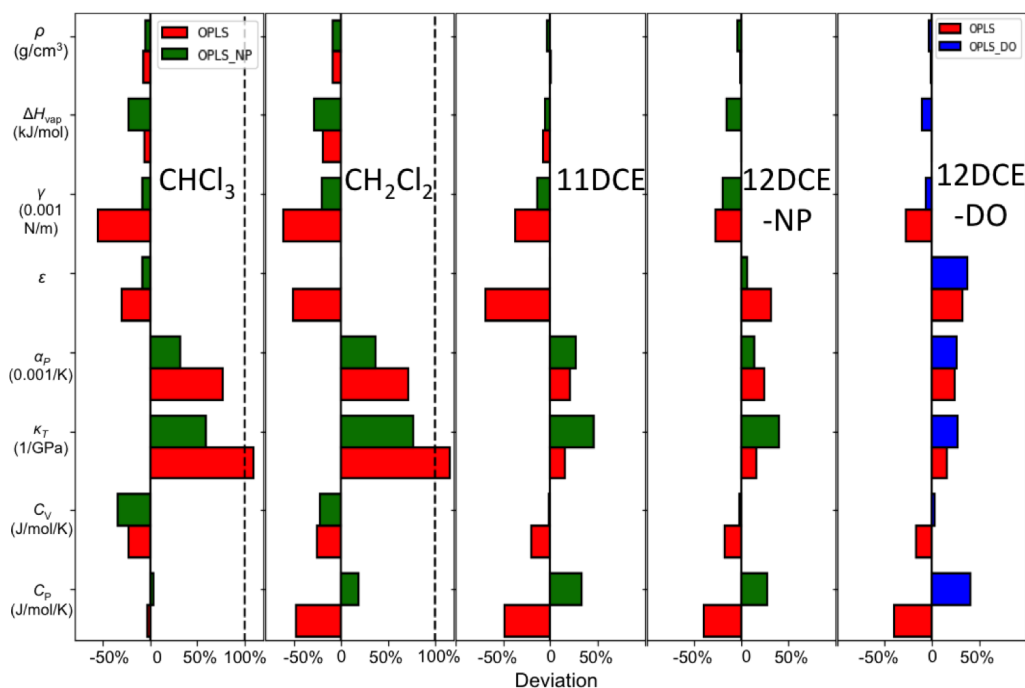


Figure 3.2: Deviations of the properties obtained by using the improved OPLS-NP and OPLS-DO models with respect to the experiment value, comparing to those of the standard OPLS all atom parametrization. (Other labels consist with Table 3.4.)

with the OPLS-NP model. Since the system is assumed to be isotropic, $\langle M \rangle^2 \approx 0$ and the overestimated value of ϵ according to Equ. 3.5 implies that the term $\langle M^2 \rangle / V$ of the polarizable system is increased. This can be explained by the fact that the dipole moment fluctuations in the denominator of $(\langle M^2 \rangle - \langle M \rangle^2) / V$ increase owing to the broadened *gauche* dipole moment regime and at the same time also the density increases.

3.5.2 Dielectric Constants as a Function of Simulation Time and System Size

We evaluate the effects of different simulation parameters such as the trajectory length and the system size during the determination of the

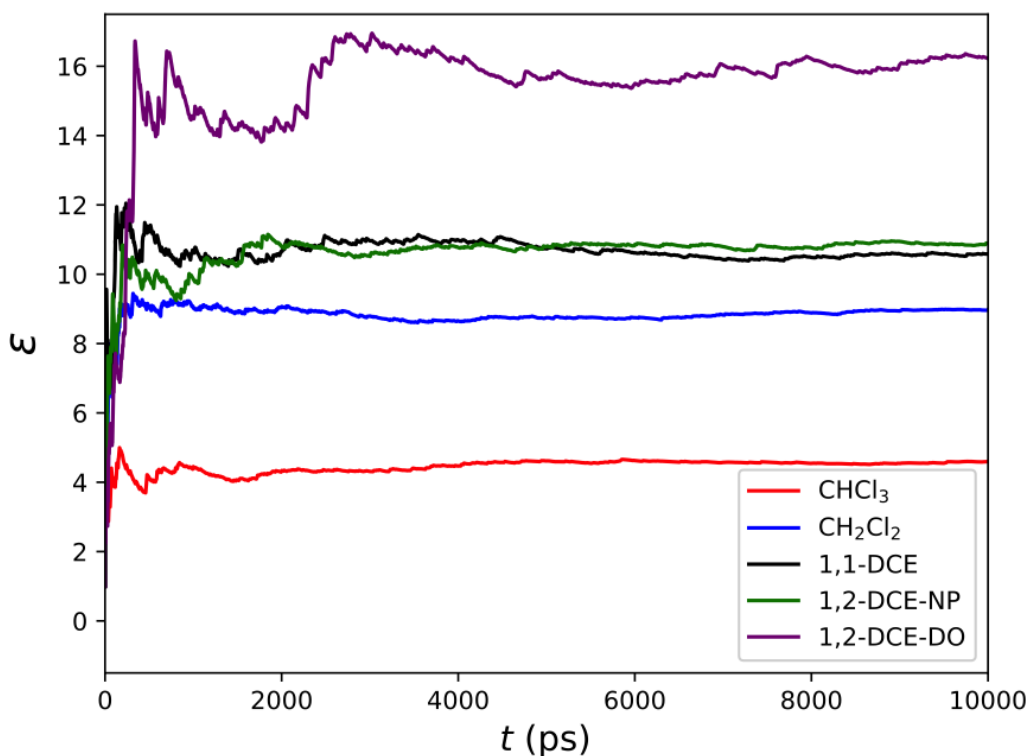


Figure 3.3: Static bulk dielectric constant ϵ as a function of the sampling time for the CHCs studied. All the simulations have been already equilibrated prior to these runs. Reproduced with permission from ref. [i]. © 2017 American Chemical Society.

static dielectric constant at 298.15 K. Figure 3.3 shows the estimates for the dielectric constant as a function of the sampling time for different CHCs. From Figure 3.3, it is clear that a properly converged value can only be achieved after about 6 ns. In general, the fluctuation properties are more difficult to predict than the simple averages, which means that longer equilibration and production simulation durations are needed. For the current work we settle on simulations with 10 ns production time length to obtain consistent estimates of dielectric constant.

To study the dependence of the computed dielectric constant on the system size, we focus on the 1,2-DCE models, since this system exhibits the most subtle effects due to its internal degree of freedom which

3. FORCE FIELD REPARAMETRIZATION

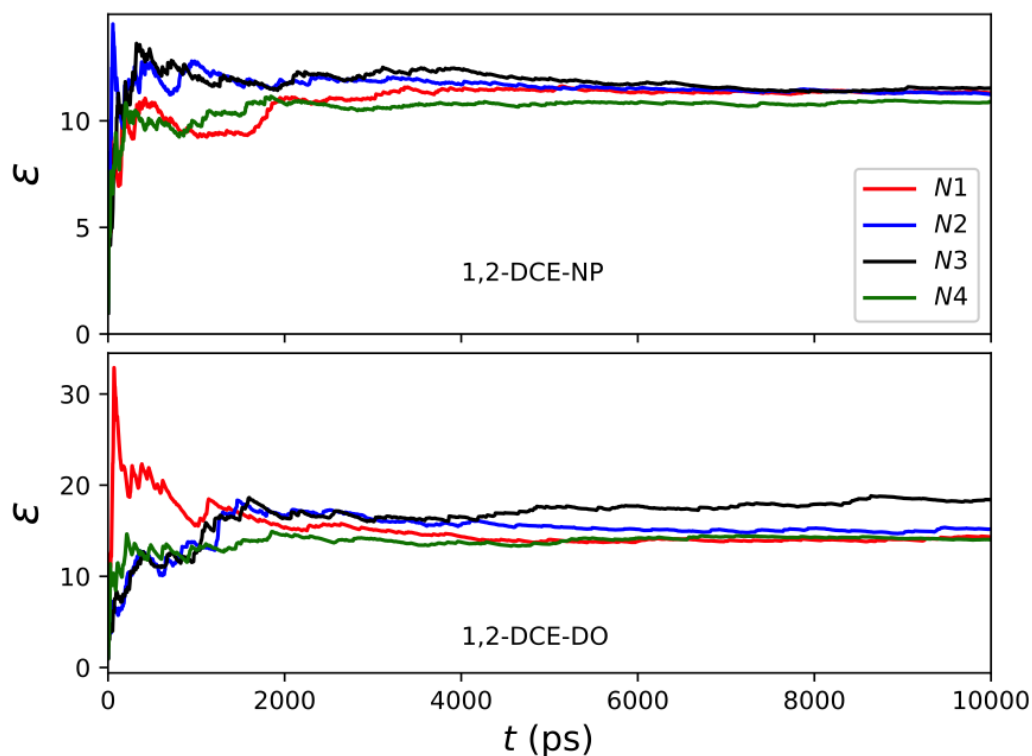


Figure 3.4: Static bulk dielectric constant ϵ as a function of the system size for 1,2-DCE-NP and 1,2-DCE-DO models. The number of molecules $N1$, $N2$, $N3$, $N4$ in the four different simulation systems are 63, 126, 189 and 252, respectively. Reproduced with permission from ref. [i]. © 2017 American Chemical Society.

dominates the molecular dipole moment. As Figure 3.4 shows, no monotonous dependence of the dielectric constants for both nonpolarizable and polarizable 1,2-DCE molecules on the system size can be established. This result agrees well with Gereben's work[125], but is unfortunately different from Morrow's finding[134] that the static dielectric constant increases with increasing system size and slowly converges to the theoretical of the infinite system size within the periodic boundary condition. Preliminary results in a different context seem to indicate that much larger system sizes might be required to enter the regime of smoother convergence. Furthermore systematic coarse-graining of models on a molecular scale to yield dielectric

continuum models definitely needs to be studied more thoroughly.[125] For the purpose of this reparametrization we settle on the larger systems with the number of molecules stated above in Section 3.3.1.

3.5.3 Temperature Dependence of Isothermal Compressibility k_T and Dielectric Constant ε

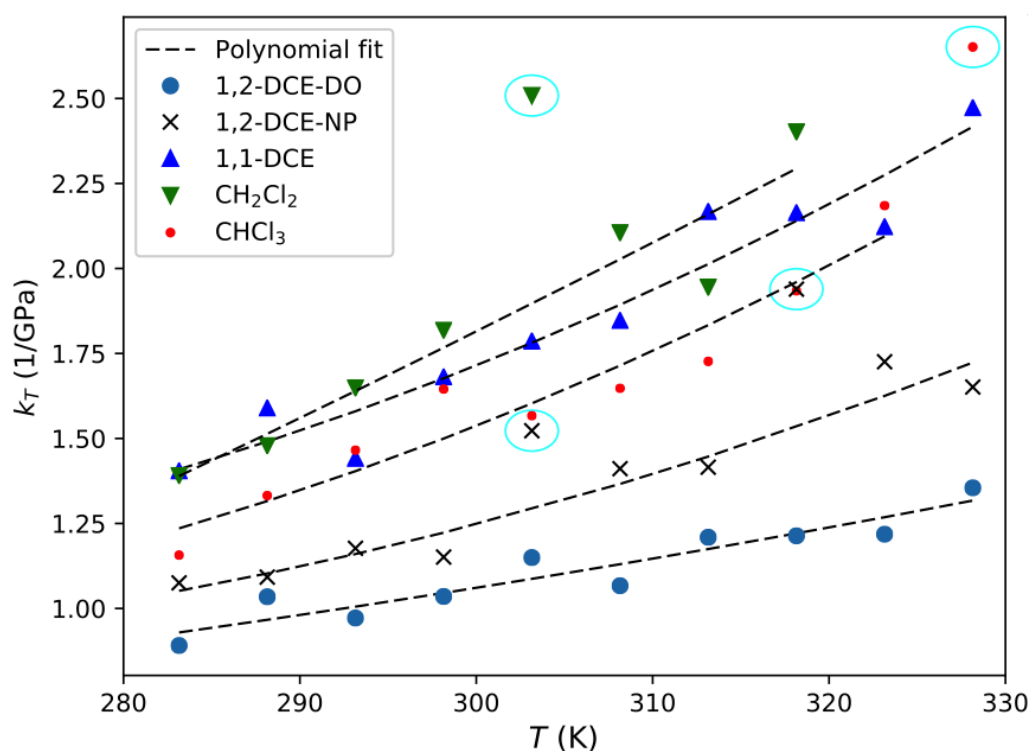


Figure 3.5: Temperature dependence of isothermal compressibility k_T for the CHC models. The black dashed lines are the polynomial fitting curves for each liquid shown. The cyan-circle marked outliers of the CHCl_3 model at 328 K, CH_2Cl_2 model at 303 K and 1,2-DCE-NP model at 303 K and 318 K are removed from the fit. All models capture the trend of increasing k_T with increasing temperature. Reproduced with permission from ref. [i]. © 2017 American Chemical Society.

We evaluate the isothermal compressibility and static dielectric constant as a function of temperature for the CHCs to investigate how well

3. FORCE FIELD REPARAMETRIZATION

Table 3.5: Parametrization of temperature dependence of isothermal compressibility in a polynomial form $k_T = A + BT + CT^2$. N is the number of data points included in each fit. Reproduced with permission from ref. [i]. © 2017 American Chemical Society.

Molecules	N	T_{min}	T_{max}	A	B	C
CHCl ₃	9	283.15	323.15	9.319e+00	-7.238e-02	1.548e-04
CH ₂ Cl ₂	7	283.15	318.15*	-2.949e+00	5.964e-03	3.305e-05
1,1-DCE	10	283.15	328.15	9.164e+00	-7.035e-02	1.517e-04
1,2-DCE-NP	8	283.15	328.15	7.727e+00	-5.679e-02	1.173e-04
1,2-DCE-DO	10	283.15	328.15	1.228e+00	-9.403e-03	2.948e-05

* T_{max} for CH₂Cl₂ is limited by the boiling point.

Table 3.6: Parametrization of temperature dependence of dielectric constant in a polynomial form $\epsilon = A + BT + CT^2$. N is the number of data points included in each fit. Reproduced with permission from ref. [i]. © 2017 American Chemical Society.

Molecules	N	T_{min}	T_{max}	A	B	C
CHCl ₃	10	283.15	328.15	5.627e+00	1.551e-02	-6.606e-05
CH ₂ Cl ₂	8	283.15	318.15*	4.717e+01	-1.975e-01	2.292e-04
1,1-DCE	10	283.15	328.15	3.061e+01	-8.209e-02	4.260e-05
1,2-DCE-NP	10	283.15	328.15	6.764e+01	-3.437e-01	5.146e-04
1,2-DCE-DO	10	283.15	328.15	2.582e+02	-1.529e+00	2.396e-03

* T_{max} for CH₂Cl₂ is limited by the boiling point.

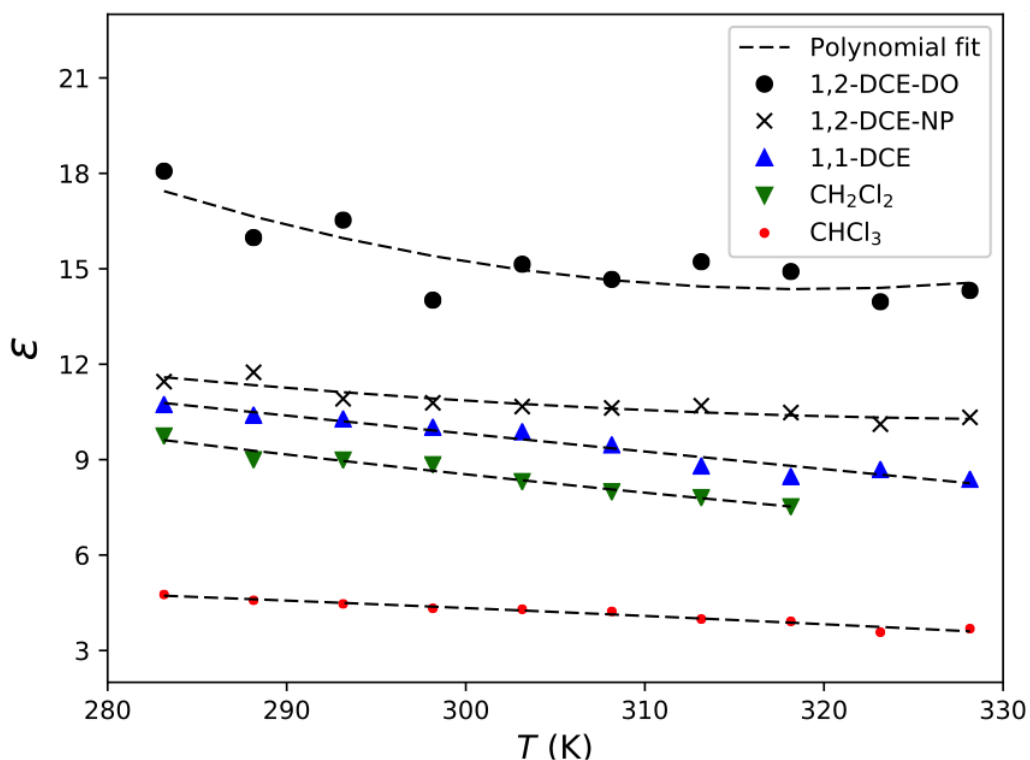


Figure 3.6: Temperature dependence of the static bulk dielectric constant ϵ for the CHC models. The black dashed lines are the polynomial fitting curves for each liquid shown. All models capture the trend of decreasing ϵ with increasing temperature. Reproduced with permission from ref. [i]. © 2017 American Chemical Society.

our reparametrized models capture the temperature dependence in the equilibrium bulk over a range of relevance in applications. Additional simulations are run at temperatures from 283.15 to 328.15 K, in 5 K increments (see Table 3.5 and 3.6), where temperatures above 320 K are already beyond the boiling point of the bulk liquid CH_2Cl_2 and thus not included for this molecule. All other settings are consistent with the above bulk liquid simulation details. The isothermal compressibility and dielectric constant are fitted to a 2nd-order polynomial in T temperatures (as is also used in the Handbook of Chemistry and Physics[113]) over the above range of temperatures in order to permit interpolation and regularization. The resulting coefficients are given

in Tables 5 and 6 for isothermal compressibility and dielectric constant, respectively. The interpolation polynomials are also used in order to compare the simulations to experimental data. Corresponding plots of the isothermal compressibility $k_T(T)$ and dielectric constant $\epsilon(T)$ as a function of temperature and their fits for each CHC with respect to the experimental results are presented in Figure 3.7 and 3.8.

As Figures 3.5 and 3.6 show, within the range of relevant temperatures, all models exhibit the same physically reasonable behavior: $k_T(T)$ increases with increasing temperature while $\epsilon(T)$ decreases with increasing temperature, which is also in agreement with the experimental values[113] and the original OPLS-AA force field[83]. It has to be noted that all models not only capture the trend of $\epsilon(T)$, with the exception of CH_2Cl_2 close to its boiling point, but also reproduce the experimental slope of this trend rather well over a range of 40 K according to the plots in Figure 3.6. The respective temperature dependence of ϵ and k_T for each CHC with the polynomial fitting are showed in Figure 3.7 and 3.8. The experimental temperature dependence of ϵ in the Handbook of Chemistry and Physics[113] is also showed in Figure 3.8.

3.6 Conclusion to Chapter 3

In this chapter, MD simulations are performed to assess the validity of reparametrized OPLS-AA based force field models in predicting solvent properties of a set of important CHCs. The new parameter sets yield a range of physical properties of these CHCs in excellent agreement with the available experimental data at ambient conditions. Additionally, it is possible to reproduce the temperature dependence of the isothermal compressibility and dielectric constant. The nonpolarizable force field reparametrizations directly use the original OPLS-AA force field as the starting point and improve the atomic partial charges and thereby the molecular dipole moments via the RESP approach based on quantum

3.6. Conclusion to Chapter 3

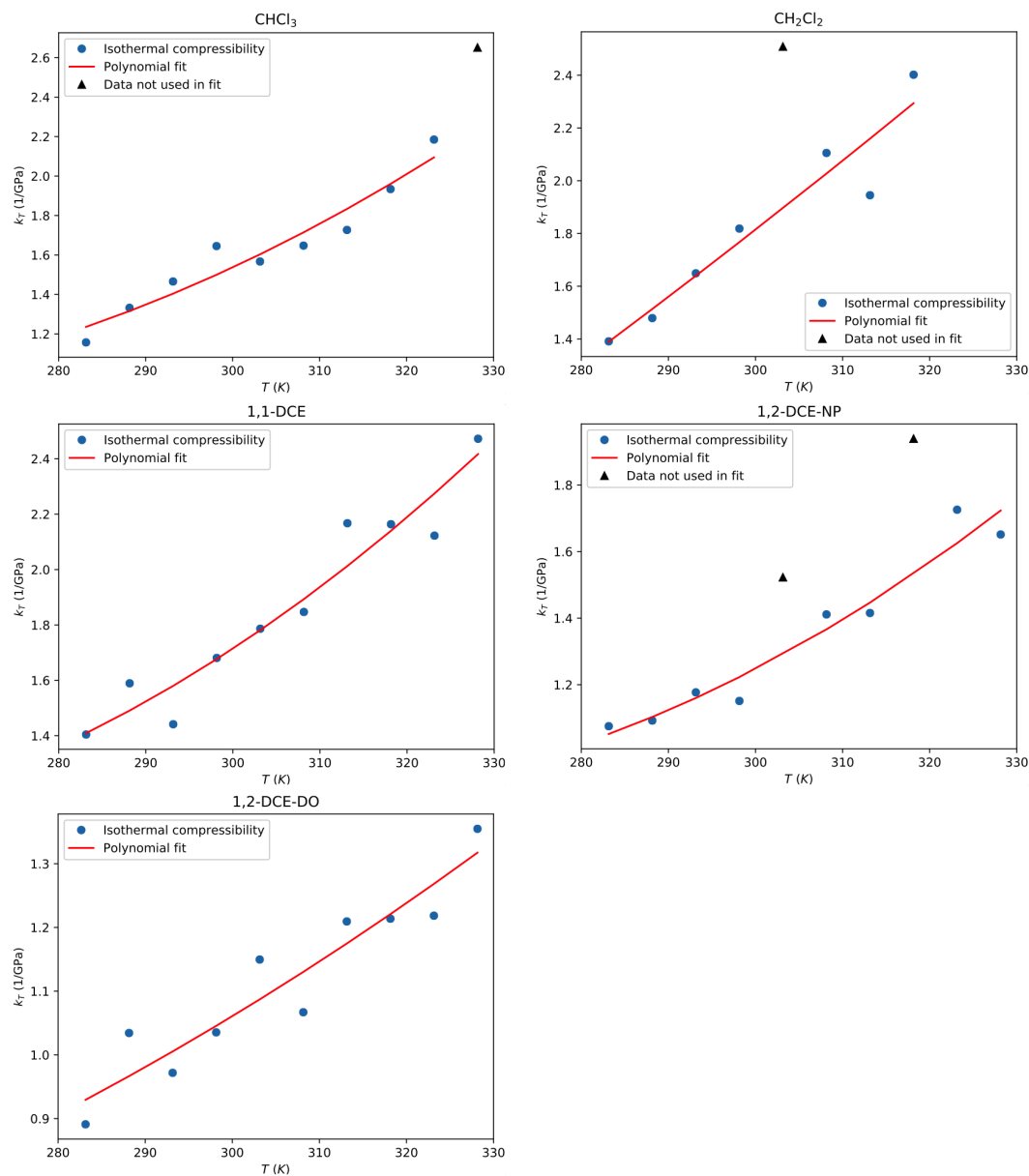


Figure 3.7: The isothermal compressibility $k_T(T)$ as a function a temperature with its polynomial fitting for CHCs. Reproduced with permission from ref. [i]. © 2017 American Chemical Society.

3. FORCE FIELD REPARAMETRIZATION

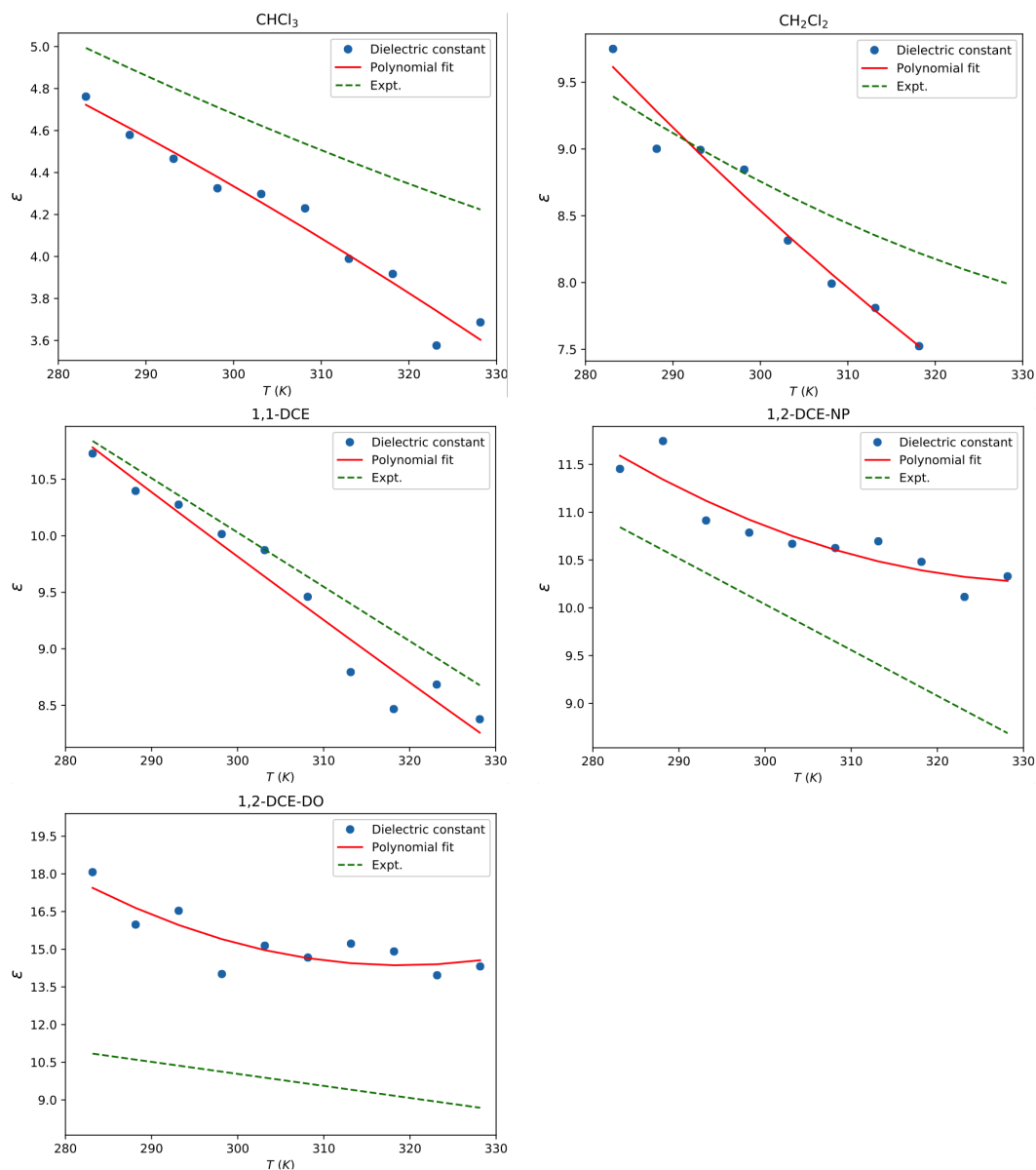


Figure 3.8: The static dielectric constant $\epsilon(T)$ as a function a temperature with its polynomial fitting for CHCs. Reproduced with permission from ref. [i]. © 2017 American Chemical Society.

chemical computations. Systematically improved torsional potential energy surface cuts for the internal degree of freedom in the flexible 1,1- and 1,2-DCE molecules are achieved by adjusting the torsional potential parameters to match corresponding quantum chemical calculations and cross-validated by checking rotational conformer distributions in classical MD simulations. Improvements for the dielectric constants could be achieved due to this systematic approach which considers a new atomic charge set that yields a better model for the respective molecular dipole moments in tight combination with a more accurate representation of the conformational distribution obtained by reparametrization of the torsion potential coefficients. For the 1,2-DCE molecule, we also develop a polarizable DO model to better capture the more intricate response properties of this molecule whose dipole moment is determined by the torsional degree of freedom. The most promising model for 1,2-DCE assigns polarizability to the carbon atom site. A careful modification of the torsion potential coefficients starting from the nonpolarizable parametrization proves to be crucial, which allows the DO model to remedy some problems with correlations among physical properties observed in the reparametrization of the NP force field.

This chapter presents a simple but effective systematically first-principles based refitting protocol for the derivation of improved parameter sets for the CHC MD models to reproduce accurate dielectric constants without sacrificing well-reproduced physical properties of existing models. The methodology developed here might be useful in deriving and improving further force fields for (organic) solvents relevant in applications that are sensitive to response properties.

Chapter 4

Intrinsic Liquid-Liquid Interface

In this chapter, we present a methodology to extract the static dielectric permittivity profile from the molecular fluctuations of the water/1,2-DCE (DCE) liquid-liquid interface by using molecular dynamics simulations, which is based on the coarse grained theoretical framework of the Willard-Chandler instantaneous interface rather than the average Gibbs dividing interface. The examined analyses include molecular density, the dielectric permittivity profile and the molecular orientation profile. This work also provides an explanation of the mechanisms underlying the overshooting parallel dielectric and averaged perpendicular dielectric responses.

4.1 Introduction

For modeling the electrostatic potential and energies in aqueous environments, continuum electrostatics methods such as the Poisson-Boltzmann and Generalized Born equations are typically used[6, 29, 30]. In these, the dielectric permittivity, as a primary input quantity for models based on continuum electrostatics, is of fundamental physical importance. The dielectric permittivity sensitively reflects the unique microscopic characteristics of the medium and dramatically influences

the electrostatic interactions in aqueous solutions. A thorough understanding of this property is a key ingredient for correctly modeling the electrostatic effects. In a homogeneous scenario the dielectric permittivity ϵ is a constant, while in an anisotropic medium ϵ becomes a second-rank tensor and spatially dependent in the medium[42–44]. The computation of the effective dielectric function of an inhomogeneous medium presents many theoretical challenges. While the bulk dielectric response of fluids is well understood, experiments, analytic theories and atomistic simulations confirm that the dielectric response is strongly modified interfaces[32–35, 40, 42–47, 99]. For example, recent terahertz spectroscopy experiments have demonstrated that at a lipid/water interface a thin water layer exists with modified dielectric properties[40]. Thomas *et. al* presented *ab initio* simulations to elucidate the orientational structure of water at the water/vapor interface and demonstrated that these molecular water arrangements are directly related to the interfacial dielectric properties.[135] For an interfacial system, its dielectric response can be described by two local profiles, $\epsilon_{\perp}(z)$ and $\epsilon_{\parallel}(z)$ (see Chapter 2). Bonthuis *et al.*[33–35] extracted dielectric profiles from interfacial water simulations and showed that the dielectric response of the surface water layer exhibits an oscillatory behavior as a function of the distance to the rigid solid surface.

Despite the importance and widespread interest, simulations of interfacial dielectric properties have so far mostly considered the case of confined liquids at a rigid solid/mobile liquid interface.[32–35, 42–47] The interface between two immiscible electrolyte solutions (ITIES) is known to be intrinsically fluxional in nature due to the presence of capillary waves[1, 8, 9, 15, 16, 136]. As an inhomogeneous environment, the liquid-liquid interface (LLI) is of ubiquitous interest in many fields and is therefore of relevance to technological and biological interfacial phenomena.[10–14, 17–20, 66, 137–144] The asymmetry of the anisotropic liquid-liquid medium in the intermolecular forces produces

unique molecular structures and dynamics. This makes the computation of the local components of ϵ in the anisotropic liquid-liquid medium even more complicated, requiring further theoretical investigation. Let us note that to the best of our knowledge, no work on the dielectric permittivity tensor for a LLI has been reported before. As a prototypical system, the water/DCE interface has been investigated intensely in the past, via both experimental and computational/theoretical modeling approaches[1, 10–13, 15–20, 145]. To investigate its dielectric behavior, we generalize the approach by Stern and Feller to this prototypical LLI system that is nonuniform in one dimension, adopting their theoretical framework to extract both parallel and perpendicular interfacial dielectric response functions from large-scale MD simulations.[43] The basic idea of this theoretical framework is to connect the macroscopic continuum description of the dielectric permittivity to the local fluctuation of the system's dipole moment via a microscopic statistical-mechanical description obtained by MD simulations. This MD approach allows us to study molecular motions of liquid interfaces and becomes a particularly useful method to investigate detailed interfacial structures and dynamics at atomic resolution[100].

From the majority of MD liquid interface simulations, it has been shown that any study purporting to show the trends across the interface needs to account for the anisotropy appropriately.[32–35, 42–47] Studying the dynamics and structures of the interface is essential for the understanding of the respective interfacial chemistry and physics. It is a long-standing challenge to obtain detailed insights into the liquid interfacial structure at the molecular scale. Most typical profiles of the physical properties of interfaces have used the average Gibbs dividing interface as a reference. The Gibbs dividing interface is an idealized and rather static average interface separating two immiscible liquid phases[8–10]. But the LLI actually undergoes dynamic fluctuations, and thus is a time-varying rough region that is neither flat nor stationary

4. INTRINSIC LIQUID-LIQUID INTERFACE

at the molecular level. The shape and location of the interface change with time. The effect of deformations and drifts that the real dynamic interface undergoes will be obscured by the simplistic average Gibbs dividing interface approximation. Lack of reliable information on the microscopic ITIES structure will therefore be a main obstacle toward understanding the true molecular nature of the interfacial properties. Statistical procedures devised to analyze MD simulations to examine the dielectric behavior of the interface have to be adjusted accordingly, which requires a molecular level insight into the true interfacial structure and needs to capture the temporal variation of the interface location. Here we establish a dynamic frame of reference in which liquid structure at molecular length scales is described in terms of distance from the time-varying position of the instantaneous interface. We refer to this instantaneous interface as the intrinsic interface, which is a significant improvement over prior work that considered the average Gibbs dividing interface[67]. In this case, we perform a spatial transformation defining the vertical distance relative to the local instantaneous interface rather than relative to a fixed Cartesian plane. By doing so the spatial deformations of the liquid phase boundary are projected out. This novel approach yields dielectric profiles with features of similar sharpness as for the rigid solid/liquid case if the statistical analysis is consistently referenced to the instantaneous LLI. Simple statistical analyses based on an average interface definition on the other hand only result in broadened featureless dielectric profiles across the interface region.

The dielectric response at the interface is evidently the outcome of the interfacial molecular arrangements and orientations due to the anisotropy. The presence of the inhomogeneous interface will strongly affect the molecular arrangements for both phases and thus their physical properties as a function of the distance to the interface. Experimental measurements such as optical second harmonic generation

and sum-frequency generation at liquid interfaces have shown that water molecules near a charged surface exhibit a strong orientational order.[146] Similar interfacial molecular orientations have been already observed in many interface simulations.[64, 147–149] Michael and Benjamin[149] found a decrease in the number of hydrogen bonds per molecule from the bulk region to the interface of water/nitrobenzene. This means that interfacial molecules arrange themselves and behave in a layered way. We perform a bivariate orientation distribution analysis of the unique orientation of each interfacial molecule, where we measure its orientation with respect to the specific local frame of the instantaneous interface. With the help of the instantaneous interface, we can detect collective interfacial molecular alignment. Our results show that both water and DCE interfacial molecules form a tightly packed layer oriented parallel to the interface, with reduced mobility in the perpendicular direction. Beyond this layer, DCE molecules quickly restore their bulk structure, while water molecules exhibit structural anisotropies that extend further into the bulk region. These molecular orientation distributions correspond to the overshooting dielectric response at the interfacial region.

This chapter presents a computational framework for the determination of the interfacial structures at the molecular level, and an advanced interfacial structure method for the description of the dielectric permittivity tensor to provide a deeper understanding of the LLI. First we give a thorough derivation of the formulation adopted to calculate the parallel and perpendicular dielectric permittivity tensor from MD simulations in Section 4.2.1. Second we illustrate the procedure to identify the instantaneous liquid-liquid interface from the MD trajectory in Section 4.2.2. Following is the description of the details of the MD simulations. Third we investigate the molecular distributions, the dielectric responses and the orientation profiles of the simulated LLI system in the reference frame of the instantaneous interface and compare with those referenced

to the average Gibbs dividing interface. A final section concludes this chapter.

4.2 Theoretical Framework

4.2.1 Dielectric Permittivity Tensor

According to Chapter 2, for the anisotropic LLI system, the space-dependent dielectric permittivity tensor can be determined from the dipolar linearized version of the molecular fluctuations.[35, 43, 46] Figure 1.2 shows the dipole fluctuations of one snapshot from the MD simulation of a water/DCE LLI. Note that the red points are either the dipole moments pointing perpendicular to the paper plane or the almost zero dipole moments of the *trans*-DCE conformers. The parallel and perpendicular polarization correlation functions are denoted as

$$h_\alpha(z) = (\langle m_\alpha(z)M_\alpha \rangle - \langle m_\alpha(z) \rangle \langle M_\alpha \rangle) / dV, \quad (4.1)$$

where dV is the volume of each statistical slab; $m_\alpha(z)$ is the polarization density for each slab at position z , $m_\alpha = \sum_{\text{slab}} \mu_\alpha$ with $\alpha = \parallel, \perp$. We analyze the water and DCE polarization contributions according to $m_\alpha = m_\alpha^{\text{water}} + m_\alpha^{\text{DCE}}$. The total polarization density is an integral over the entire simulation box, $M_\alpha = \int_0^z m_\alpha dz$. We define the total polarization correlation as $H_\alpha = \langle M_\alpha^2 \rangle_0 - \langle M_\alpha \rangle_0^2$. The parallel dielectric permittivity tensor component which varies along the z -axis, $\varepsilon_\parallel(z)$, is related to the average lateral polarization correlations:

$$\varepsilon_\parallel(z) = 1 + \frac{1}{k_B T \varepsilon_0} h_\parallel(z) \left(1 - \frac{H_\parallel}{V}\right)^{-1}, \quad (4.2)$$

where $k_B T$ denotes the thermal energy and ε_0 is the vacuum permittivity. The perpendicular dielectric permittivity profile is

$$\varepsilon_\perp(z) = 1 + \frac{1}{k_B T \varepsilon_0} h_\perp(z) \left(1 + \left[\frac{H_\perp}{V} - h_\perp(z)\right]\right)^{-1}. \quad (4.3)$$

For comparison, the perpendicular polarization correlation function $h_{\perp}(z)$ can be expressed as a function of $\varepsilon_{\perp}(z)$,

$$h_{\perp}(z) = k_B T \varepsilon_0 \frac{[1 + H_{\perp}(z)/V][\varepsilon_{\perp}(z) - 1]}{\varepsilon_{\perp}(z)}. \quad (4.4)$$

In the interface situation, where all the fields and observables are nonuniform in the z direction, the parallel and perpendicular expressions Equ. 4.2 and Equ. 4.3 will be intrinsically different, which will be discussed in the following in detail. The key finding is that a local expression of the permittivity involves correlations of the local and total polarization, not of the local polarization alone.

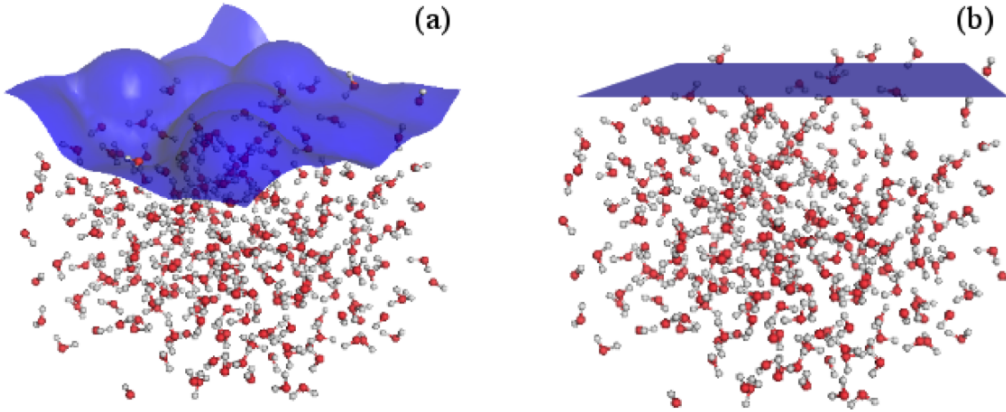


Figure 4.1: Schematic representation of the interface structure in the same snapshot from a MD simulation: (a) the instantaneous interface; (b) the average Gibbs dividing interface.

4.2.2 Definition of the Intrinsic Interface

To quantify the molecular properties associated with soft interfaces, we need to reference to the location of the interface. Capillary waves smooth out the structure of fluid interfaces, making the detailed analysis of the interfacial structure difficult.[9] Most computer simulation investigations performed to date have focused on the computation of average density profiles, ignoring the characterization of the intrinsic structure

4. INTRINSIC LIQUID-LIQUID INTERFACE

of the interface. This approach is justified from a macroscopic point of view in which the interface is just the slowly evolving region where two bulk phases are in contact. From the point of view of a system, e.g. a catalyst particle, embedded into the interface, which experiences the response of its rather local environment on shorter time and length scales, the average description is too simplistic. Recent theoretical developments have improved the situation, making possible the detailed investigation of the interfacial intrinsic structure at an unprecedented level of detail.[58, 63–65, 67] We then can take out the varying nature of the oscillations around the average Gibbs dividing interface.

We all know this liquid interfacial configuration by nature is time-dependent because of the molecular motions. Thus the respective interface location definition must accommodate the molecular roughness of the interface. To identify this time varying position of the instantaneous LLI, we adopt a procedure proposed by Willard and Chandler[67] for a liquid-vapor interface system, which we adapt for our LLI system. This procedure uniquely defines a molecularly rough interface based upon a spatial coarse-grained representation of the discrete molecular positions. It can be used to describe time dependent phenomena, because this procedure can be applied to any arbitrary i th particle at any position \mathbf{r}_i in time t : $\rho(\mathbf{r}, t) = \sum_i \delta(\mathbf{r} - \mathbf{r}_i(t))$. This equation indicates the instantaneous density field at space-time point (\mathbf{r}, t) . Here we adopt coarse-graining to form a set of more manageable fields.[67] Coarse-graining is achieved by convoluting the instantaneous density field of each water molecular position \mathbf{r}_0 in the simulation cell with a normalized Gaussian.

$$\varphi(\mathbf{r}; \tilde{\zeta}) = (2\pi\tilde{\zeta}^2)^{-d/2} \exp(-r^2/2\tilde{\zeta}^2), \quad (4.5)$$

where $r = |\mathbf{r} - \mathbf{r}_0|$, $\tilde{\zeta}$ is the coarse-graining length, and d stands for dimensionality. In our system, the water molecule yields a better approximation for the instantaneous interface since it is smaller than DCE

and more adequately described by a single spherical Gaussian density. We use $\xi = 2.5\text{\AA}$ as suggested before, which is approximately the molecular diameter of water.[67]. Compared to capillary wave theory, this molecular diameter is similar to the empirical parameter used to truncate the capillary wave spectrum and it would be meaningless to define the instantaneous interface with a resolution higher than the molecular diameter.[56–59] We reference the spherical Gaussian density function with respect to the molecular center of mass (c.o.m) of the water molecule and normalize to 1, which yields an approximate probability density for a water molecule in the simulation box. Combining with $\rho(\mathbf{r}, t)$ the coarse-grained density field is obtained

$$\bar{\rho}(\mathbf{r}, t) = \sum_i \varphi_i(\mathbf{r}; \xi). \quad (4.6)$$

The coarse-grained density field $\bar{\rho}$ can be interpolated on a spatial grid covering the simulation cell. To define the instantaneous interface location, we use the so-called “10-90” criterion[21, 53, 150] for the water/DCE LLI. That is determining the interface as points in space where the density is 90% of the bulk water density. To extract this iso-density interface, we chose an efficient algorithm called Marching Cubes algorithm[151]. Marching Cubes is a 3D iso-surface construction technique, which produces a triangle mesh by computing iso-densities from discrete data. By connecting the patches from all cubes on the iso-surface boundary, we obtain a triangulated surface representation. Figure 4.1 illustrates the obtained instantaneous LLI from one snapshot of a MD simulation, with the horizontal averaged Gibbs dividing interface for comparison. Only a slab of water molecules and the upper instantaneous interface as a blue wavy surface are showed.

The distance for each time-varying molecular configuration to the iso-density interface $\Delta r_i(t)$ is defined as the distance from the molecular c.o.m to the projected point on the continuous instantaneous interface. The projected point is obtained by projecting the respective c.o.m along

4. INTRINSIC LIQUID-LIQUID INTERFACE

the z -axis onto the instantaneous LLI. We base all statistic binning on this distance when calculating the response properties. In this way we can take out the smoothing effect of the capillary waves and thus obtain the required nanoscopic length and timescales of the interfacial response properties. This approach is advantageous because there is no need for the the calculation of the response properties across the interface to identify the exact locations of each interfacial molecule, thus the Willard-Chandler interface as a coarse-grained approach is efficient and effective over prior works. Additionally it is independent of an interfacial reference plane or presumed symmetry, since for the long range dynamic behavior the two instantaneous interfaces (with respect to the upper and lower water phase boundaries, see Figure 4.1) are not correlated. This will makes the dielectric profiles with respect to the different instantaneous interfaces intrinsically different, as we will discuss in detail in Section 4.3.

4.2.3 MD Simulation Details

The interface is constructed by joining two preequilibrated liquid slabs of DCE and water. After energy minimization to remove the unphysical energy contributions due to overlaps of the molecules at the boundary of the two liquid phases, the interface system is further equilibrated for 1 ns in the canonical (NVT) ensemble and 3 ns in the isothermal-isobaric (NPT) ensemble at 1 atm and 298.15 K. Here DCE is modeled using the nonpolarizable force field reparametrized in Chapter 3, which has shown to be effective at matching the bulk dielectric property. Water is simulated using the flexible SPC model[126]. The nonbonded (LJ) interactions are treated using a regular spherical cutoff (cutoff radius = 10Å). The long-range Coulombic interaction is evaluated using the Ewald summation method with a precision of a relative value 10^{-6} . All simulations except those within Figure 4.15 are performed in rectangular boxes with dimensions, $L_x = L_y = 22\text{Å}$ and $L_z = 90\text{Å}$. The liquid slab thicknesses, $\approx 68\text{Å}$ for DCE and $\approx 22\text{Å}$ for water, are chosen to avoid correlations between different interfaces. After proper equilibration, we run a 10 ns long trajectory in the microcanonical (NVE) ensemble to make sure that the measurements are reasonably converged and averaged over sufficient time lengths. The integration time step is 1 fs. In the 10 ns long production, 10001 sample configurations are recorded with an interval of 1 ps for analysis. All simulations are carried out using the LAMMPS simulation program package with periodic boundary conditions applied in all three directions.[130] The translational motion of the c.o.m is removed every time step. Analysis programs are taken from either *Pizza.py* toolkit[131] or written in-house.

4.3 Results and Discussion

The work described here is aimed at the integration of continuum modeling with molecular informations provided by MD simulations, in

4. INTRINSIC LIQUID-LIQUID INTERFACE

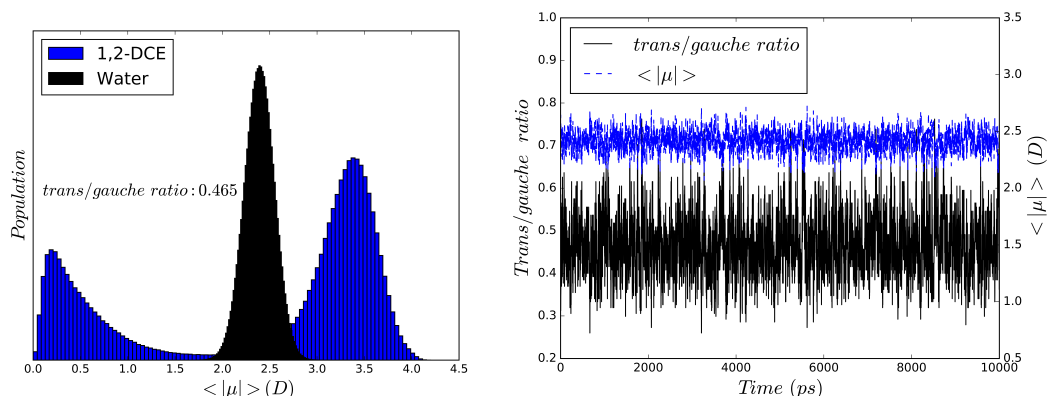


Figure 4.2: The distribution of dipole moment magnitudes for the water/DCE LLI system (left panel) with water molecular dipoles shown as black histogram while DCE as blue histogram. The histograms of molecular dipole moment magnitudes have been averaged over whole trajectories. The *trans/gauche* ratio of the total DCE phase is 0.465. The right panel shows the fluctuations of the *trans/gauche* ratio (black curves and left axis) and average absolute molecular dipole moment (blue curves and right axis) of the total DCE phase within each LLI's MD snapshot as a function of the simulation time.

order to investigate the dielectric response of the water/DCE LLI. Here the respective experimental number density is $N_{\rho}^{water} = \frac{\rho^{water} V^{total}}{M^{water} N_{slab}} = 33.43/nm^3$ for water and $N_{\rho}^{DCE} = \frac{\rho^{DCE} V^{total}}{M^{DCE} N_{slab}} = 7.65/nm^3$ for DCE at $T=298.15$ K and $P=1$ bar. A novel aspect of our analyses is that the specific dielectric profiles are measured using the theoretical framework introduced in Section 2.1 of Chapter 2 with respect to the instantaneous interface defined in Section 4.2.2. Specifically we measure the molecular density profiles, the dielectric permittivity profiles, and the molecular orientation profiles reference to the instantaneous interface. Herein slab analyses are used to bin different instantaneous curved layer regions in order to calculate all these response properties of the heterogeneous LLI. We first define slabs based on the vertical distance from the instantaneous LLI and then perform statistics within these time-dependent fluxional slabs over the whole MD trajectory. The differences

between the coordinates based on the instantaneous interface and the average Gibbs dividing interface are also examined.

4.3.1 Dipole Distribution Profile of LLI

The left panel of Figure 4.2 shows histogram distributions of the dipole moment magnitudes for water and DCE. The conformational *trans/gauche* ratio for DCE in the LLI system is showed in the right panel, which is consistent with first principle calculations.[73, 145] Herein the perfect *cis* conformer with 0° is almost nonexistent due to the energy barrier, which can be seen in Figure 3.1. In particular *trans* in the narrowest sense would only be 180° , which would be statistically meaningless. Thus in analogy to the bulk calculation in Chapter 3, DCE molecules with dihedral angles in $[30^\circ, 90^\circ]$ are declared *gauche* conformers whereas a *trans* conformer is characterized by a dihedral interval of $[150^\circ, 210^\circ]$. All other rotamers (with a percentage of 0.189% over the whole trajectory) are excluded with respect to the *trans/gauche* ratio. The present ratio is a little bit smaller than the bulk DCE conformational ratio 0.477 (calculated from the *trans* ratio 0.323 in Chapter 3), which means there are more *gauche* conformers in the water/DCE LLI than in bulk DCE. This is in agreement with the assumption that the DCE phase can be “polarized” when it is in contact with a water phase.

The right panel of Figure 4.2 shows the respective fluctuation of the *trans/gauche* ratio and the average magnitude of the DCE molecular dipole moment as a function of the simulation time. The average molecular dipole moment of DCE have been sufficiently converged with a constant value $\sim 2.4D$ over simulation time. The stationary state of ratio fluctuations shown in the figure confirm that the sampling time is sufficient to fully equilibrate the *trans/gauche* ratio in the LLI system. And the configuration samples taken every picosecond (ps)

4. INTRINSIC LIQUID-LIQUID INTERFACE

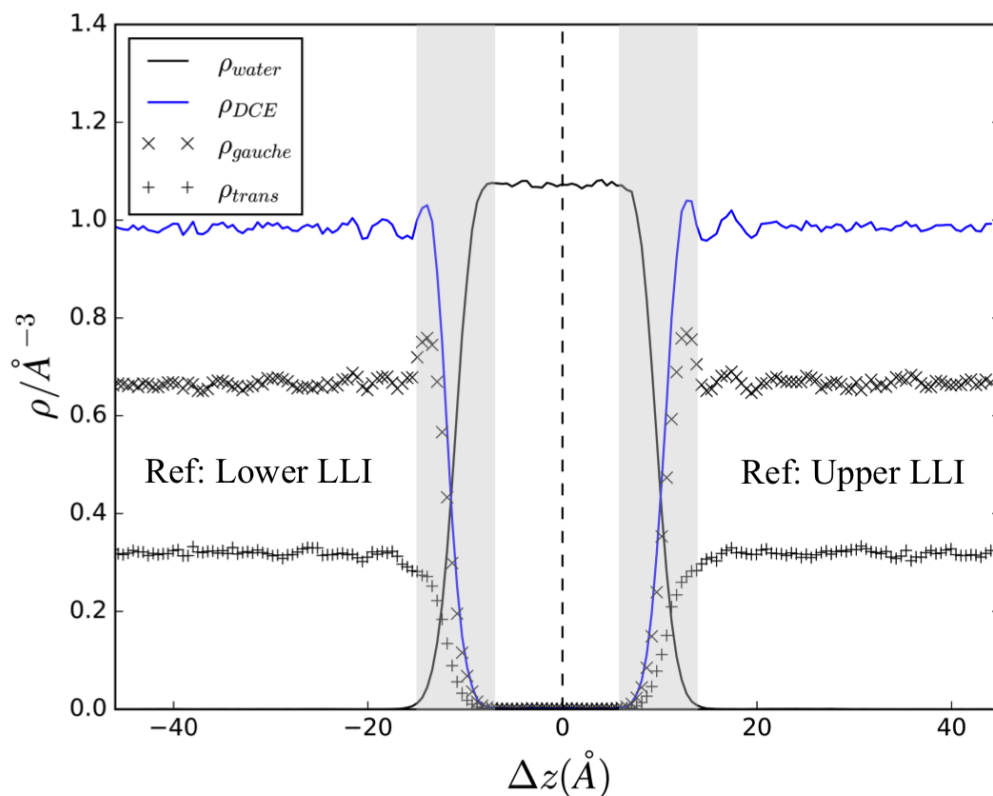


Figure 4.3: Molecular number density as a function of distance from the respective instantaneous interface along the z -axis (blue and black solid lines refer to water and DCE components, respectively; left axis), normalized by the experimental molecular number density of N_{ρ}^{water} and N_{ρ}^{DCE} . Contributions of the *gauche* (cross) and *trans* (plus) DCE conformers are also showed, scaled by N_{ρ}^{DCE} of the overall DCE molecules. The oscillations of the DCE density profile are mostly due to the *gauche* conformer. The zero dashed line is set at the central water phase. Negative values indicate positions below the central water phase and are measured with respect to the lower instantaneous LLI (the left light grey region), while positive values are relative to the upper instantaneous LLI (the right light grey region).

can be regarded as independent microscopic states for sampling the conformational transitions.

4.3.2 Molecular Distribution Profile

To characterize the distribution of the truly interfacial molecules along the interface perpendicular axis, we have estimated the molecular density profile for the respective water and 1,2-DCE phases. Meaningful statistics within the interfacial analyses have to correspond to the closest interface. Figure 4.3 shows two analyses for both simulated phases with respect to the lower and upper instantaneous LLIs for the respective molecular density profile. The profiles are joined in the bulk of the central water phase at the position ($= 0$) indicated by the dashed line shown in Figure 4.3. The negative distance values are referenced to the lower instantaneous LLI while positive values are relative to the upper LLI. The lower and upper LLI regions are marked by the light grey stripes. It is obvious that for a periodic interfacial simulation the interface may change the position parallel to its normal axis (here the z axis) because of collective translational motions, which would result in an averaged broadened interface. In order to avoid such artifacts, we removed the translation of the c.o.m at every time step during the simulation. As seen in the figure, the density profiles of water and DCE correspond to each other and are in agreement with the time-averaged interfaces at around $z = \pm 12 \text{ \AA}$. The fluctuations in the interface location in the z direction vanish because of the time average. In the two interfacial regions, the density profile of the *gauche* DCE conformer exhibits peaks, including an enrichment of *gauche* DCE near the interface, while the *trans* DCE density is correspondingly found to be smaller than in the bulk phase. This result suggests that the water phase induces a strong polarization of DCE molecules in the vicinity of the interface, which is consistent with the assumption that the low dielectric DCE phase can be “polarized” substantially near the interface

by the presence of the water phase. This finding is in agreement with earlier simulation results using the average Gibbs dividing interface[22]. And it should be mentioned here that the molecular density profile in Figure 4.3 is similar to that calculated reference to the average Gibbs dividing interface. This is because the molecular density is physical property that is comparatively easy to converge, which is hardly showing response to the molecular orientations near the true instantaneous LLI.

4.3.3 Parallel Dielectric Permittivity Tensor

The local dielectric permittivity tensors along the z axis are calculated with respect to the instantaneous LLI. Due to the isotropy within the xy -plane, only the parallel dielectric permittivity tensor $\epsilon_{\parallel}(\Delta z)$ in the x direction ($\epsilon_{xx}(\Delta z)$) as a function of the distance normal to the upper and lower instantaneous interface is showed in Figure 4.4. From this figure, the parallel dielectric profiles $\epsilon_{xx}(\Delta z)$ reveal a clear distinction between DCE and water phases with their respective approximate bulk dielectric values. In contrast to the average Gibbs dividing interface, which only shows the featureless parallel dielectric response displayed in the bottom panel of Figure 4.4, we observe enhanced dielectric responses within the instantaneous interfacial regions. It can be seen from the top two panels of Figure 4.4 that the overshooting dielectric response acquired at the interfaces on the water side propagates into the bulk water phase, and a relatively high permittivity tensor component in the vicinity of the interfacial DCE region approaches the average bulk DCE dielectric value within a few Angstroms.

The dielectric permittivity tensor components with large deviations from the experimental bulk values at the interface are not statistical fluctuations but imply a very high degree of molecular order in the vicinity of the interface. Support for this argument follows from the

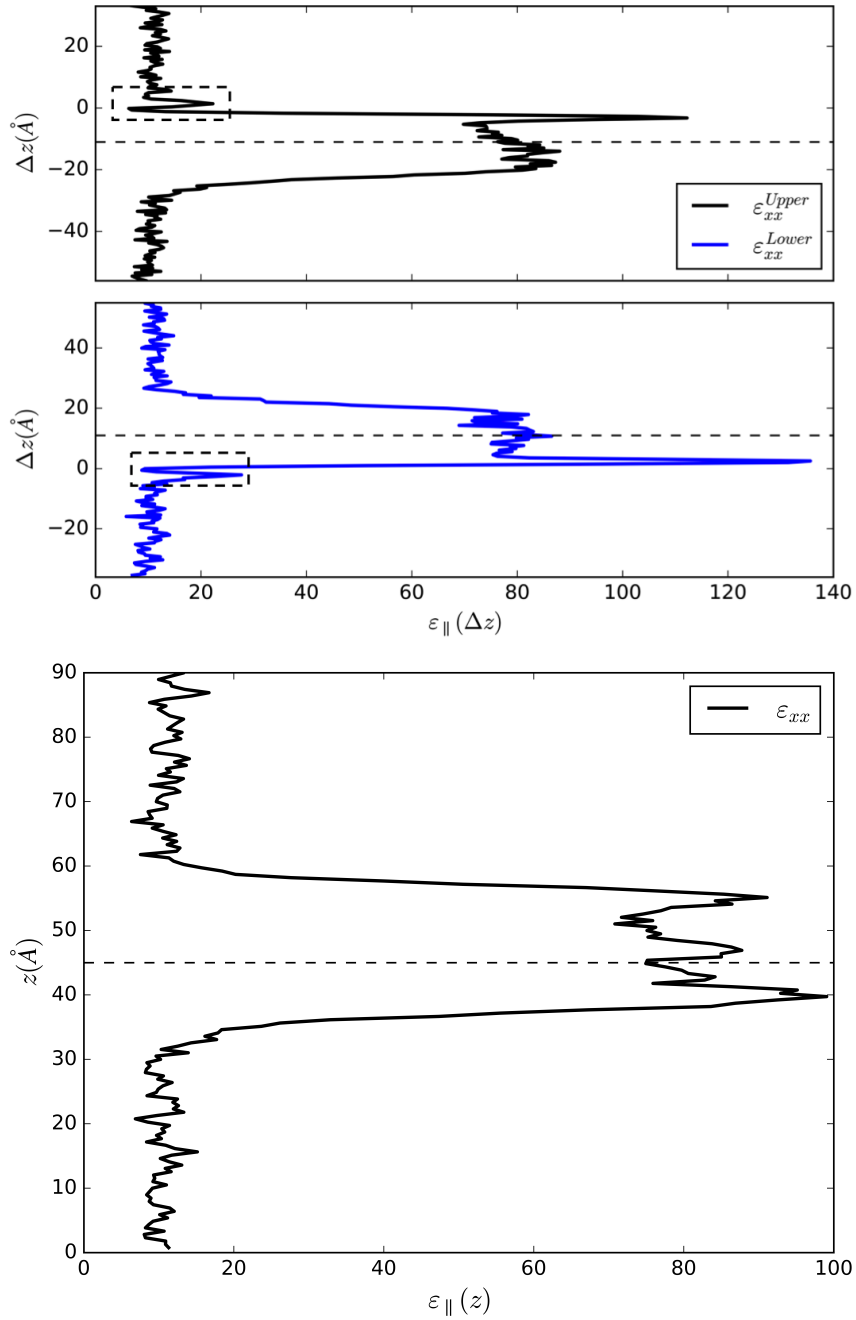


Figure 4.4: Parallel dielectric profiles ($\epsilon_{||}(\Delta z)$, top panel) with respect to the distances normal to the lower and upper instantaneous interface respectively. The zero locations are approximately the reference instantaneous interfaces. Parallel dielectric permittivity as a function of z referenced to the average Gibbs dividing interface ($\epsilon_{||}(z)$, bottom panel). The dashed lines show the central water phase, corresponding to the zero dashed line in Figure 4.3.

4. INTRINSIC LIQUID-LIQUID INTERFACE

molecular orientation profiles in Figure 4.7 and 4.9, which we will get back to in Section 4.3.4. It is known that in the isotropic bulk liquid, water or DCE molecules are randomly orientated, but they will have a non-uniform distribution at the interface due to the asymmetry in forces experienced by other types of molecules within the interfacial region.

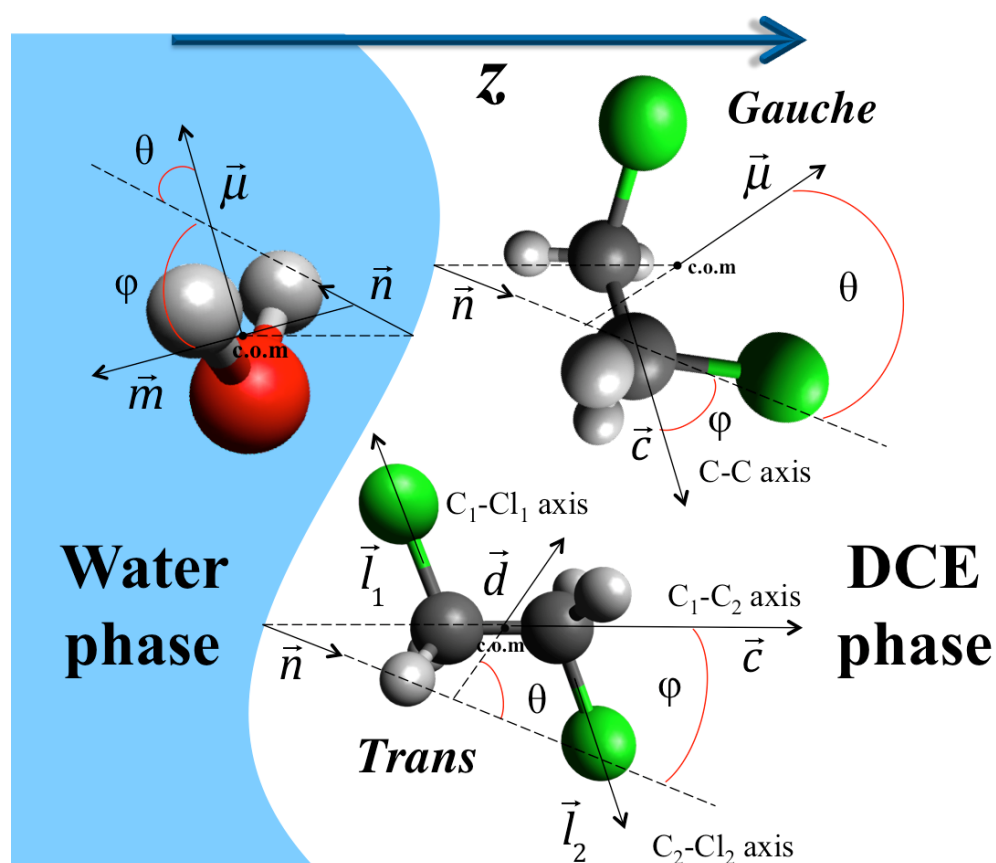


Figure 4.5: Schematic orientation of the water and DCE molecule the instantaneous liquid-liquid interface. The definition of the angles θ and φ in the local atomic coordinate frame for water and DCE molecules are showed. The vectors are the instantaneous interface normal vector \vec{n} , the molecular dipole vector $\vec{\mu}$, the molecular normal vector \vec{m} for water and the carbon-carbon axis vector \vec{c} for DCE; the new defined vector \vec{d} for *trans* DCE.

The local dielectric responses due to the statistics referenced to the upper

and lower interface reference, respectively, can be aligned as the top panels of Figure 4.4 shown. Each of the profiles is slightly asymmetric because of the microscopic asymmetries in parallel polarization correlations $h_{xx}(\Delta z)$ (Equ. 4.1) due to the respective interface references. It is evident that the fluctuations in the two instantaneous interfaces do not occur in parallel, therefore spontaneously formed asymmetries between both interfaces can survive up to a typical time scale of nanoseconds. For meaningful statistical analyses of interface effects, the response properties or any other slowly decaying properties must be calculated with reference to the closest interface. The distance between such interfaces in a simulation needs to be large enough to avoid correlations between them as well as to reach the true bulk behavior somewhere between them.

4.3.4 Molecular Orientation

So far we have investigated the dielectric response properties of the interface separating the water from DCE phase. It is also interesting to analyze to what extent the two phases are affected by the presence of the interface. Compared to the liquid molecular structure confined by a solid surface, molecular structures at soft LLI are even more complicated phenomena that must be associated with the intrinsic characteristics of the liquid interface. The molecular structure in the vicinity of the interface is strongly influenced by the interface's time-dependent position. The detailed knowledge of the molecular orientational profiles with respect to the above defined intrinsic LLI will be discussed in the following. This is a prerequisite for understanding the true nature of the heterogeneous LLI.

To fully describe the orientation of a molecule in one conformation, we require two independent vectors to define a local molecular coordinate system. Here for water, these two independent vectors are the normal

vector to the molecular plane \vec{m} and the molecular dipole vector $\vec{\mu}$. For *gauche* DCE, they are the carbon-carbon (C-C) axis \vec{c} and its molecular dipole vector $\vec{\mu}$. Then we take these molecular coordinate systems and reference them to the locally defined instantaneous LLI to give a full description of the orientational statistics of molecules. We calculate the bivariate joint distribution of two independent orientational variables, which are two isolated angles θ and φ used to determine the molecular orientation, as shown in Figure 4.5. For water, θ is the angle between its molecular dipole vector $\vec{\mu}$ and the interface normal vector \vec{n} ; φ is the angle between the molecular normal vector \vec{m} and the projection of \vec{n} onto the plane perpendicular to $\vec{\mu}$. The projection \vec{n}_\perp is calculated as

$$|\vec{n}_\perp\rangle = |\vec{n}\rangle - \frac{\langle \vec{n} | \vec{\mu} \rangle}{\|\vec{\mu}\|^2} \cdot |\vec{\mu}\rangle. \quad (4.7)$$

For *gauche* DCE, θ is the angle between its molecular dipole vector $\vec{\mu}$ and the interface normal vector \vec{n} ; φ is the angle between the carbon-carbon (C-C) axis \vec{c} and \vec{n}_\perp , defined the same way as for the water molecule. Due to the molecular symmetry of the water and DCE molecule, the normal vector to the molecular plane in water as well as the C-C vector in DCE are only defined up to a change in sign (i.e. +- vector). This is clearly an approximation if vibrations (e.g. O-H or C-Cl stretches) deform the molecules and break their ideal symmetry (in both cases C_{2v}). Due to timescale and energy separation between such vibrations[22, 152, 153] and the torsion (c.f. Figure 4.2), we assume this approximation to be valid throughout. Thus water and DCE molecules can always be orientated in such a way that restricts the angle φ to the interval $[0^\circ, 90^\circ]$. The molecular orientation analyses of H₂O and DCE molecules are performed at various distances measured with respect to the lower instantaneous LLI. The bivariate orientation distributions for the angles θ and φ , $H(\cos\theta, \varphi)$, are calculated for all molecules falling within a particular distance away from the interface to create the intensity histograms.

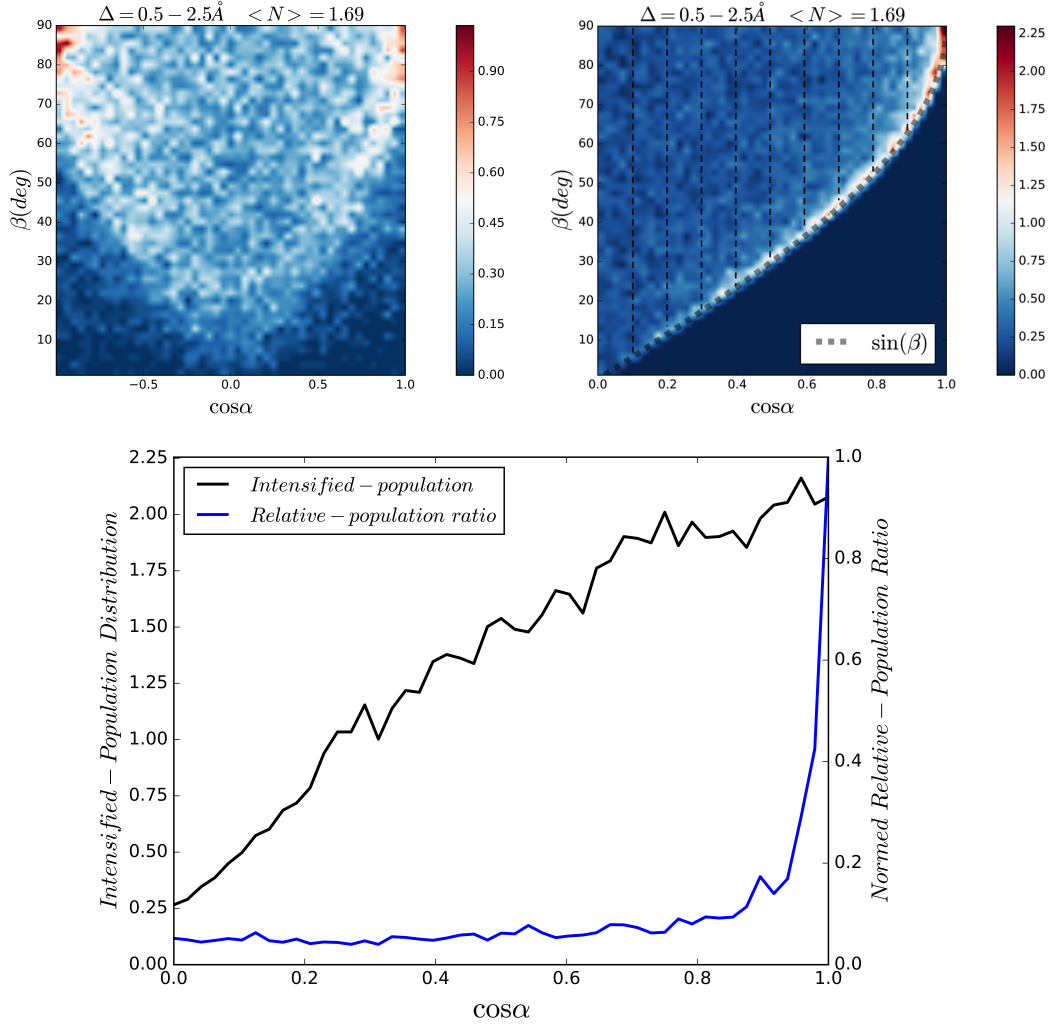


Figure 4.6: Top panels: correlation histograms of *trans* DCE within an interfacial region from 0.5 Å to 2.5 Å relative to the lower instantaneous LLI ($z = 0$ Å). Top left panel shows the correlation between the C-C vector \vec{c} and dipole vector $\vec{\mu}$, while top right panel shows that between the C-C vector \vec{c} and the new defined vector \vec{d} . The horizontal axes of the histograms represent $\cos \alpha = \frac{\langle \vec{n} | \vec{c} \rangle}{\|\vec{c}\|}$. The vertical axis of the top left panel represents $\beta = \arccos\left(\frac{\langle \vec{n} | \vec{\mu} \rangle}{\|\vec{\mu}\|}\right)$, whereas it represents $\beta = \arccos\left(\frac{\langle \vec{n} | \vec{d} \rangle}{\|\vec{d}\|}\right)$ in the top right panel. The grey thick dashed line in the top right panel is a perfect Sine function of angle β . Areas of low intensity appear in dark blue, and highest intensity in dark red. The black curve in the bottom panel shows population distributions lie within the intensified red and white realm (see the top right panel) as a function of $\cos \alpha$. The blue curve in the bottom panel shows the normed relative population ratio (see text) as a function of $\cos \alpha$. The dashed lines in the top right panel indicate the analyzed windows for the integral.

For the case of the DCE molecule in the *trans* configuration, using the molecular dipole vector $\vec{\mu}$ and the C-C vector \vec{c} like for the *gauche* DCE to describe the rigid body geometry with respect to the instantaneous interface becomes problematic as shown in Figure 4.6. The analysis yields a strong geometric correlation of the angle α between the vector \vec{n} and \vec{c} and the angle β between \vec{n} and $\vec{\mu}$ within a slab having a thickness of 2 Å. The slab is defined based on the vertical distance from the lower instantaneous LLI ($z = 0$ Å). In the top left panel of Figure 4.6, the randomly distributed white regions are noise or error fluctuations of the correlation. This is because the dipole vector $\vec{\mu}$ of the *trans* DCE has almost zero magnitude and is therefore not a stable descriptor for molecular orientation. Any kind of bond angle changes will tilt this tiny dipole vector into completely different directions, which results in large orientational noise. In this case, we cannot separate the influence of the C-C axis orientation and the strongly varying orientation of the, in magnitude, almost vanishing dipole vector. We need to define a new vector for the *trans* case that is closest to what the dipole vector is for the *gauche* conformer.

As Figure 4.5 schematically shows, we define a new vector \vec{d} for *trans* DCE as

$$\vec{d} = \vec{c} \times (\vec{l}_1 \times \vec{c} - \vec{l}_2 \times \vec{c}), \quad (4.8)$$

where vectors \vec{l}_1 and \vec{l}_2 are respectively the C₁-Cl₁ and C₂-Cl₂ axis vector. Here instead of taking the sum of the normal vector $\vec{l}_1 \times \vec{c}$ of the plane (Cl₁C₁C₂) and $\vec{l}_2 \times \vec{c}$ of plane (C₁C₂Cl₂) to obtain an almost vanishing sum vector, we take the difference and multiply it by the vector \vec{c} to obtain a robust descriptor for the *trans* conformer's rigid body motion which coincides with the dipole vector in the case of the *gauche* conformer. This vector \vec{d} lies within the plane containing the C-C axis and bisecting the torsional angle. It is stable against all bending angle and bond length deviations from the molecular ideal symmetry. Then we perform the same rigid body geometry analysis within the

same slab for *trans* DCE by calculating the correlation of the newly defined vector \vec{d} and vector \vec{c} , which is showed in the top right panel of Figure 4.6.

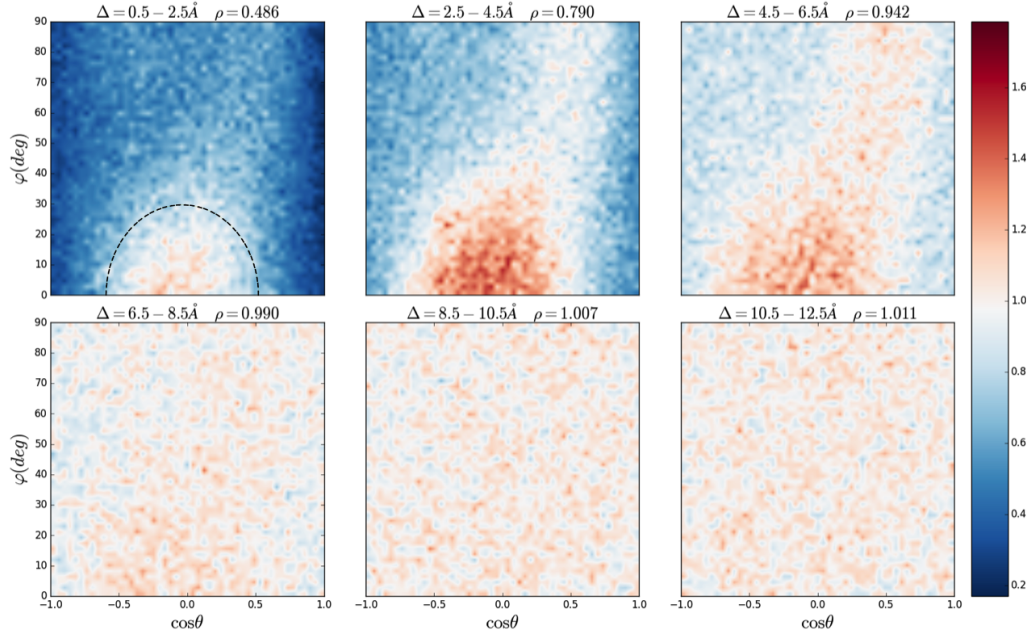


Figure 4.7: Molecular orientation histograms of H₂O for the water/DCE LLI system with respect to the lower instantaneous interface region. The location of each of the regions which are represented by these histogram is given by their distance from the LLI in Å. The instantaneous interface is located at 0 Å with positive distances toward the water phase. Each histogram shows the bivariate angle distribution for $\cos\theta$ (horizontal axes, $\cos\theta = \frac{\langle \vec{n} | \vec{\mu} \rangle}{\|\vec{\mu}\|}$) and φ (vertical axes, $\varphi = \arccos(\langle \vec{n}_\perp | \vec{m} \rangle)$). Regions of high intensity are marked as dark red, and low intensity are dark blue. A completely white histogram would correspond to a distribution which attains the perfect average homogenous bulk state at each point.

Due to the symmetry in the choice of the vectors used in Equ. 4.8 to define the vector \vec{d} , where all involved vectors could each equally well point in two opposite directions, both angles α and β lie in the range $[0^\circ, 90^\circ]$. Basing on this panel, we can see that the majority of distributions are focused in the intensified red and white realm.

4. INTRINSIC LIQUID-LIQUID INTERFACE

The black curve in the bottom panel quantitatively shows the population distributions within the intensified red and white realm as a function of $\cos \alpha$. Moreover, we calculate the ratio of the population focused in the red and white realm to the integral of populations in the dashed windows in the light blue region (see the top right panel). This ratio as a function of $\cos \alpha$ is showed as the blue curve in the bottom panel. The black and blue curves demonstrate that the majority of *trans* molecules falls in the region as the Sine curve marked in the top right panel, and the highest probability is focused in the region corresponding to $H(\cos \alpha \approx 1.0, \beta \approx 90^\circ)$. This strong correlation indicates that the vector \vec{d} and vector \vec{c} are perpendicular to each other. Thus we can conclude that the vector \vec{d} is well defined for *trans* DCE as a basis for the molecular orientation analysis to distinguish its influence from those of vector \vec{c} . For *gauche* DCE, since its molecular dipole vector $\vec{\mu}$ is already well defined, there is no need to define a new vector.

Then the molecular orientation correlations of H₂O and DCE molecules are calculated for all molecules falling within a particular distance from the instantaneous interface to create histograms as shown in Figures 4.7 and 4.9. The distance of each slab with respect to the LLI is marked (in Å) on the top, with the interfacial location set at 0 Å. All histograms are normalized by the respective experimental number density of water ($N_{\rho}^{water} = 33.43/nm^3$) and DCE ($N_{\rho}^{DCE} = 7.65/nm^3$) at $T=298.15$ K and $P=1$ bar. The relative water molecular number densities of each slab normalized by N_{ρ}^{water} are showed on the top of each histogram in water orientation profiles, whereas showing the *trans/gauche* ratios ω and the relative DCE number densities of each slab normalized by N_{ρ}^{DCE} on each DCE histogram's top. The horizontal axes of each histogram represent $\cos \theta$ values, and the vertical axes represent the angle φ . These histograms illustrate how the orientations of H₂O and DCE change when moving from the interface further into the respective bulk phase.

H₂O Orientation Profile

The increased density at $\cos \theta = 0$ in Figure 4.7 indicates that on the water side of the LLI the water molecular dipoles have a clear tendency to lie parallel to the instantaneous interface. These water molecular structural effects appear to be directly related to the interfacial dielectric response in Figure 4.4. This is also suggested by the experiment of atomic force microscopy to measure the dielectric permittivity profile of the water at the charged mica surface, where the polarization variation is related to the reorientation of the water molecular dipoles and thus results in a variable water dielectric permittivity at the interface.[154] However, molecular ordering behavior at the LLI is rather different from that at the mica or solid-liquid interface, which makes the mechanism of the interfacial dielectric response intrinsically different.

The solid-liquid interface has the well-known excluded volume effect, which results in a density depletion gap at the surface. In experiments at a water-mica interface[154] and simulations for the hydrophobic diamond-water interface[33], oscillations of the water molecular density were observed for such interfaces. According to Bonthuis, this density oscillation is similar in shape to the parallel dielectric profile, see Figure 1.1.[33] In the LLI simulation, however, there are no water density oscillations, as shown by the blue water density curve in Figure 4.3, which is perfectly flat in the interfacial regions. Thus the oscillating parallel dielectric response observed at the LLI in Figure 4.4 cannot be explained by variations in the density profiles, which is intrinsically different from the case of the solid-liquid interface.

For an atomically flat rigid solid surface, the Gibbs dividing interface provides a perfect description. In the vicinity of a solid surface, molecules cannot rotate or reorient as freely as in the case of the instantaneous LLI. This yields a layer of water molecules directly at the interface with molecular normal vectors predominantly parallel to

4. INTRINSIC LIQUID-LIQUID INTERFACE

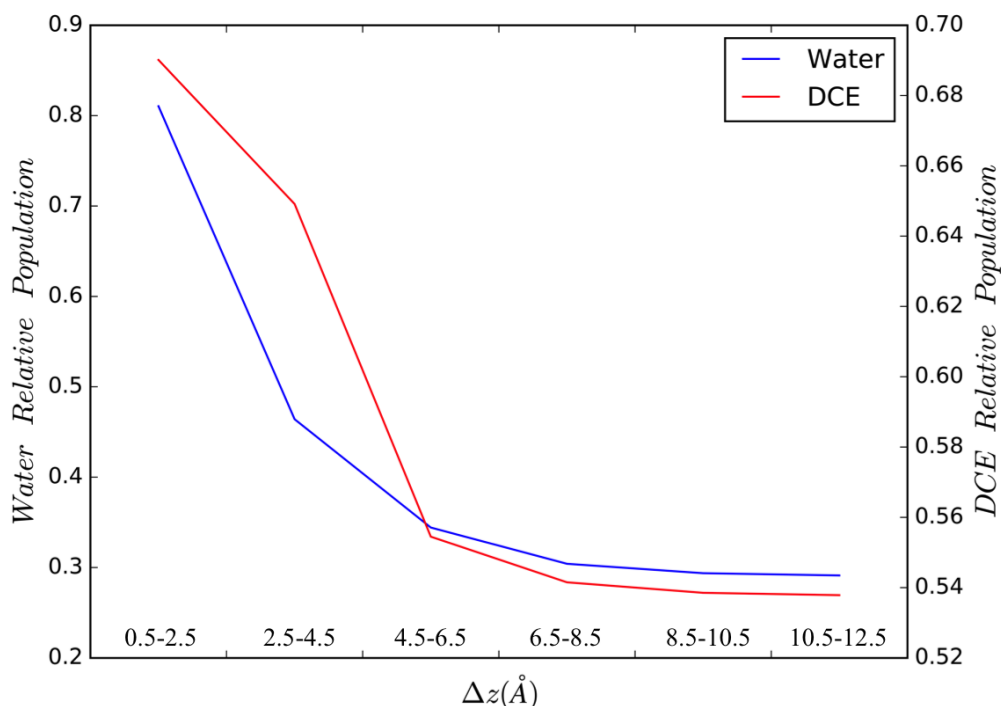


Figure 4.8: Relative population within the regions of preferential molecular orientation marked by the semi-ellipse for water (blue line, left axis) and rectangular box for DCE (red line, right axis) in the respective orientation profiles. The details to define these regions can be found in the main text. The population of each slab with respect to the instantaneous LLI is normalized by the respective molecular number density.

the interface normal vector. Their molecular dipoles are highly ordered parallel to the rigid interface. Since the water molecules in the first layer cannot reorient freely, the dielectric response directly at the interface is lower than the bulk value. Additionally, the hydrogen bond network to molecules in the next layer is partially broken, yielding a second layer in which the water molecules and thus their dipoles can reorient more freely which translates into a larger dielectric response for the bulk. Thus the water dielectric permittivity profile oscillates at the interface. But in the case of the LLI, water and DCE molecules can easily accommodate each other. The preferential orientations in Figure

4.7 are not simply due to confinement by the rigid surface but result from subtler collective polarization effects in the neighboring liquid phases which follow the spatial fluctuations of the instantaneous LLI. For the parallel dielectric permittivity profiles ϵ_{\parallel} at the LLI, it seems that the preferential alignment of water molecular dipoles parallel to the interface can explain the observed effects if these molecular dipoles are reorienting. This will result in a bigger net effect, which produces the large dielectric response (peak with $\epsilon_{\parallel} = 120 - 140$) observed in the water phase in the vicinity of the interface (see top panels of Figure 4.4). We note that due to the difference in the mechanism leading to this peak, there is no accompanying region of the lowered ϵ_{\parallel} closer to the interface which has been observed in simulations of solid-liquid interfaces.

Figure 4.7 shows that the orientational order is vanishing from the interface further into the bulk phase. If we calculate the population distribution of the intensified regions, corresponding to the semi-ellipse marked region in Figure 4.7, for each histogram, we can quantify the relative water orientation distribution in Figure 4.8. Close to the interface, the intensified semi-ellipse region corresponds to water molecules that exhibit a preferential orientation relative to the interface. It is defined with the center of the ellipse at $(0, 0)$, where the semi-axis in the $\cos \theta$ direction is 0.62 and along the φ axis is 27.9 (degrees). Here all the histograms are generated based on the slab statistics, which contain different averaged numbers of molecules. We therefore normalize the populations of each histogram to the experimental number density $N_{slab}^{water} / N_{\rho}^{water}$. The DCE relative populations are calculated in the same way with the normalization factor $N_{slab}^{DCE} / N_{\rho}^{DCE}$.

Figure 4.8 (blue curves and the left axis) quantitatively shows the preferred water orientation distribution decaying from the interface value towards the random orientation characteristics of the bulk. Starting from the interface to the bulk water phase, the preferential orientation of water is lost quickly at first and asymptotically approaches a plateau,

4. INTRINSIC LIQUID-LIQUID INTERFACE

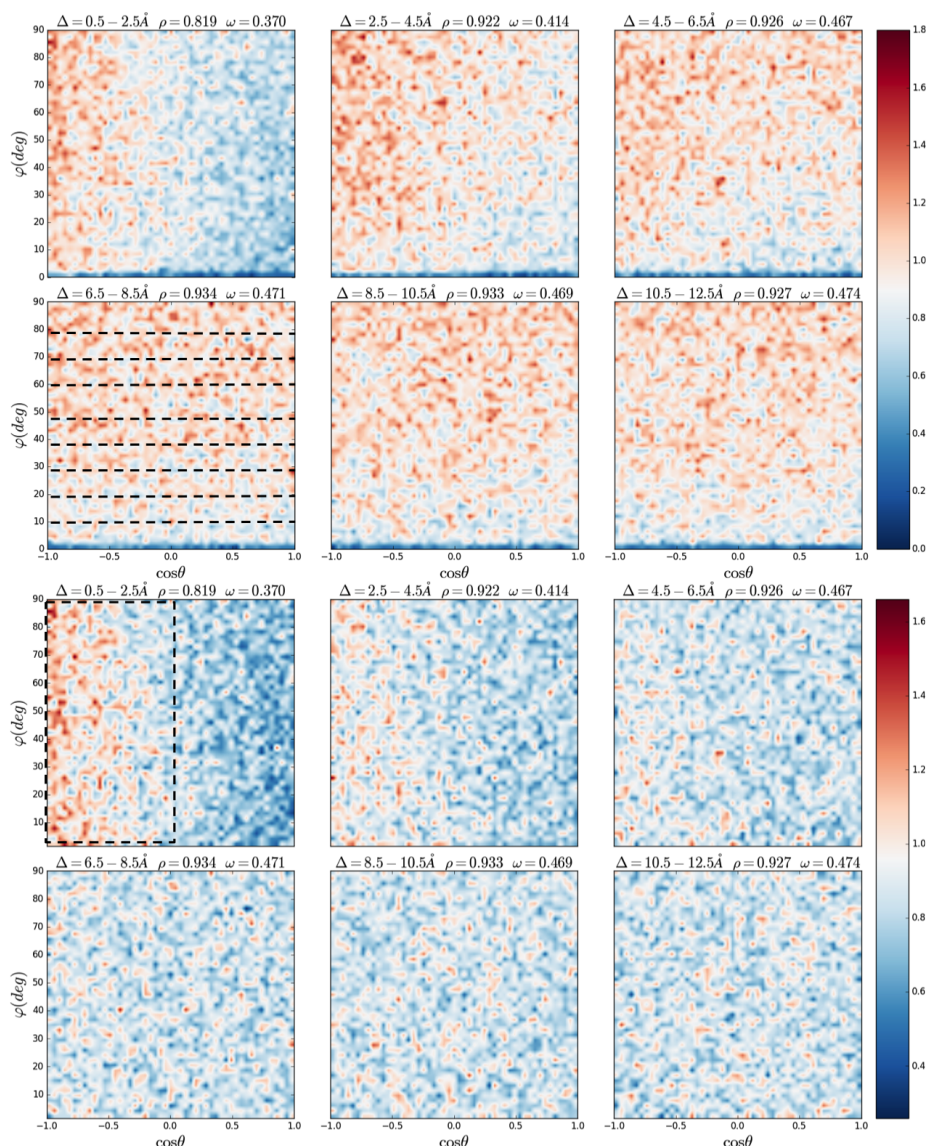


Figure 4.9: Molecular orientation histograms of DCE near the water/DCE LLI with respect to the lower instantaneous interface $z = 0 \text{ \AA}$ (top panel). Positive distances indicate locations further into the DCE phase. Each histogram is a bivariate angle distributions for $\cos \theta$ (horizontal axes, $\cos \theta = \frac{\langle \vec{n} | \vec{\mu} \rangle}{\|\vec{\mu}\|}$) and φ (vertical axes, $\varphi = \arccos(\langle \vec{n}_\perp | \vec{c} \rangle)$). Regions of high intensity are marked as dark red, and low intensity are dark blue. Bottom panel shows the molecular orientation histograms of DCE near LLI after removing the Sine statistical effect (see text) while all other settings are the same for the top panel. A completely white histogram in the bottom panel corresponds to a distribution which attains the perfect average homogenous bulk DCE state at each point.

with a value of 0.3, which corresponds to the ratio of the integration domain to the area of the whole histogram ($S_{semi-ellipse}/S_{All} = 30.2\%$). The plot shows that the orientation within the region around 10 Å and further away from the interface is the same as the bulk random orientation. The decay observed in Figure 4.8 parallels the water density profile in Figure 4.3, which at ~ 10 Å is eventually approaching the bulk.

DCE Orientation Profile

The resulting orientation profile for DCE in Figure 4.9 indicates that the first layers of the organic phase exhibit a preferential orientation for the molecular dipoles to point toward the bulk organic phase. Due to the molecular alignment, we again observe a relatively high dielectric permittivity in the vicinity of the interface in the DCE phase (dash-line-rectangle marked region of the top panel in Figure 4.4).

The dark blue region in the orientation histograms in the top panel of Figure 4.9 seems to indicate that $\varphi = 0^\circ$ does not occur. This means that the probability of finding the C-C axis in alignment with the interfacial normal vector is negligible. This effect is solely due to varying weights of the integration area for points on the surface of a sphere which scales as the Sine of the polar angle. To elucidate this effect, we take the integral over $\cos \theta$ in $[-1, 0]$, $\int_{-1}^0 H d \cos \theta$, for histograms in the top panel of Figure 4.9. The dashed lines in the fourth histogram indicate the analyzed windows for the integral. Figure 4.10 shows that the resulting integrals as a function of φ all behave like a normal Sine function (black dashed curve).

In all plots of the top panel of Figure 4.9, the integration area effect, that is the Sine integration effect, dominates the whole color scale of the histograms, making a detailed analysis difficult. We therefore normalize the histograms by the integration area, removing the bins for which $\sin \varphi \approx 0$, to avoid numerically problems due to division by zero.

4. INTRINSIC LIQUID-LIQUID INTERFACE

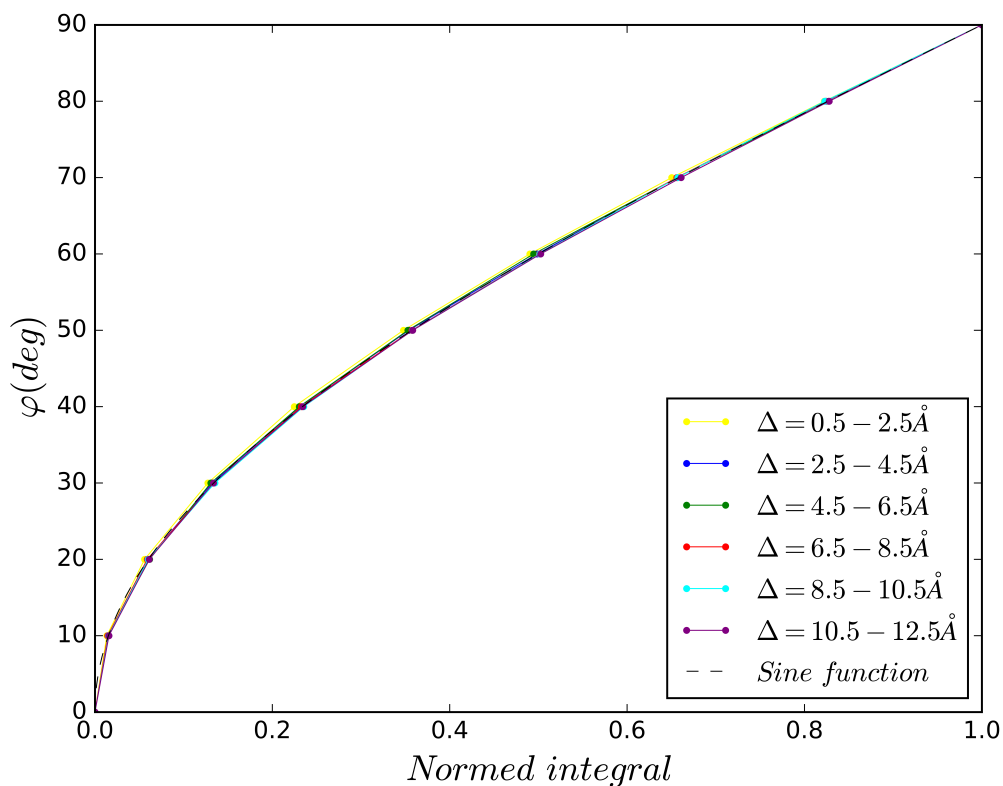


Figure 4.10: Integrals $\int_{-1}^0 H d \cos \theta$ as a function of the angle φ with respect to the histograms in the top panel of Figure 4.9. All the integrals are normalized by the respective total population within each histogram.

After removing the Sine integral effect on top of the histograms, we obtain the histograms in the bottom panel of Figure 4.9, which allow us to examine the molecular orientations of DCE with respect to the lower instantaneous LLI. As the panel shows, it is much more clear that the predominant orientation is rapidly lost towards the bulk phase when increasing the distance to the instantaneous LLI. In analogy to the water orientation analysis, we calculate the relative population of the left-half histogram region in the bottom panel of Figure 4.9. We obtain a quantitative result of the relative intensified DCE orientation distribution in Figure 4.8. The integral area is marked by a dashed

rectangular box, as shown in the first histogram in the bottom panel. There are exactly as many vertical stripes of the 2D histogram in the marked region as in the rest of the respective histogram. The blue curve and right axis corresponding to DCE in Figure 4.8 quantitatively shows the loss of orientation observed in Figure 4.9.

Due to the considerable difference in the dipole moments of the two conformers of DCE, it is necessary to separate the individual orientational contributions of the *gauche* from the *trans* case to the total DCE histograms. Figure 4.11 shows the orientation profiles of the *gauche* and *trans* DCE referenced to the lower instantaneous LLI, with the average number of molecules $\langle N \rangle$ shown on the top of each plot. All histograms are normalized by the experimental number density of DCE ($N_{\rho}^{DCE} = 7.65/nm^3$ for DCE at $T=298.15$ K and $P=1$ bar).

In Figure 4.11, a completely white histogram in the *gauche* DCE orientation profile (top panel) corresponds to a value of ~ 0.65 , which is approximately the percentage of the population of the *gauche* conformers in the DCE bulk liquid. This corresponds to a distribution attaining the perfect average homogenous DCE bulk state at each point. For the *trans* DCE orientation profile (bottom panel), a completely white histogram with a value of ~ 0.35 is also regarded as the perfect average homogenous bulk state of DCE. From the top panel, it is obvious that the orientation profile of DCE in Figure 4.9 is dominated by the *gauche* conformer. This dominant *gauche* population is consistent with the peak of the molecular density profile of DCE in the interface region in Figure 4.3.

To extract the subtle *trans* DCE orientation effects, we consider the relative population of the left half region of each histogram for the *gauche* and *trans* orientation profile, which are marked by the dashed rectangular box in Figure 4.11. They correspond to the respective preferential orientations relative to the instantaneous LLI. Here same as

4. INTRINSIC LIQUID-LIQUID INTERFACE

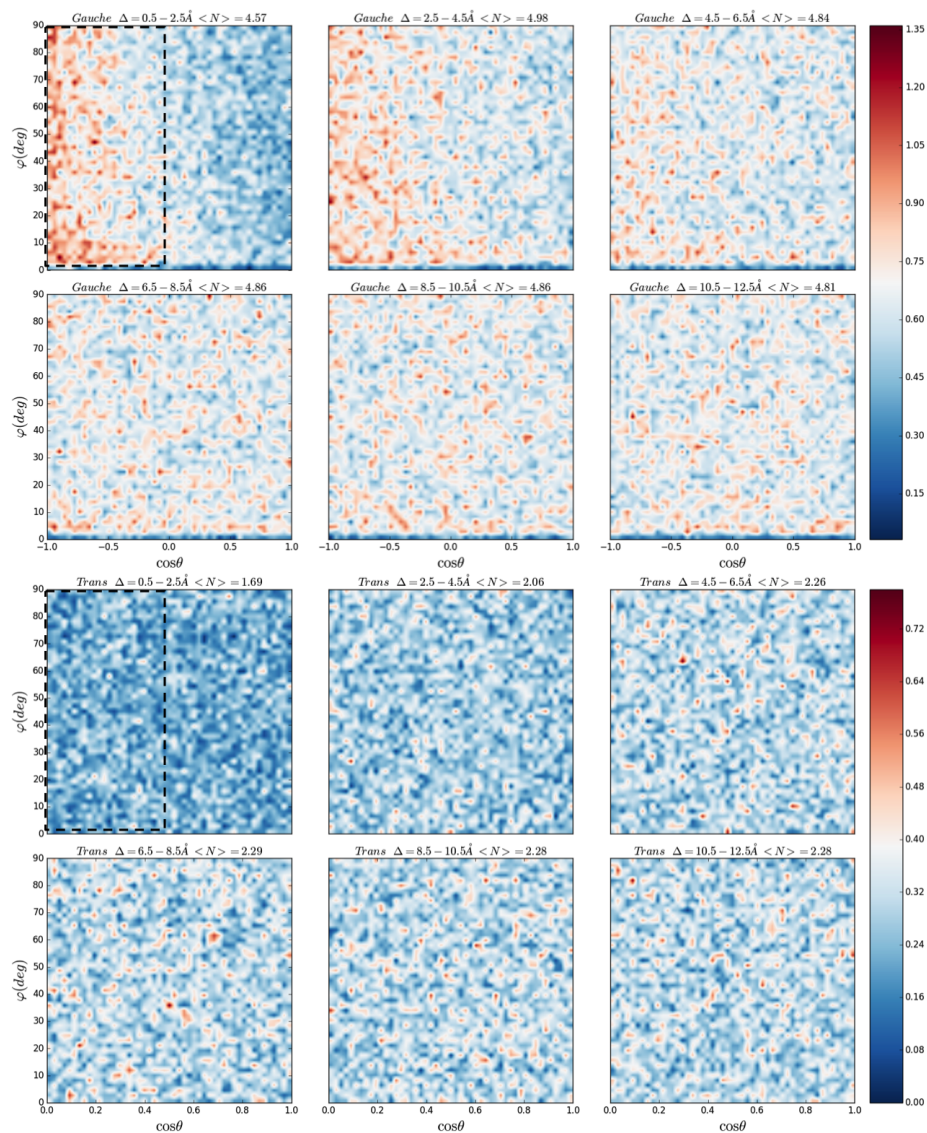


Figure 4.11: Orientation profiles of the *gauche* (top panel) and *trans* DCE (bottom panel) with respect to the lower instantaneous LLI. The respective conformer and the average number of molecules in each layer is showed on the top of each plot. The distances of each histogram from the instantaneous LLI are also showed on the top in \AA with the location of the LLI set at 0 \AA . Regions of high intensity are marked as dark red, and low intensity are dark blue.

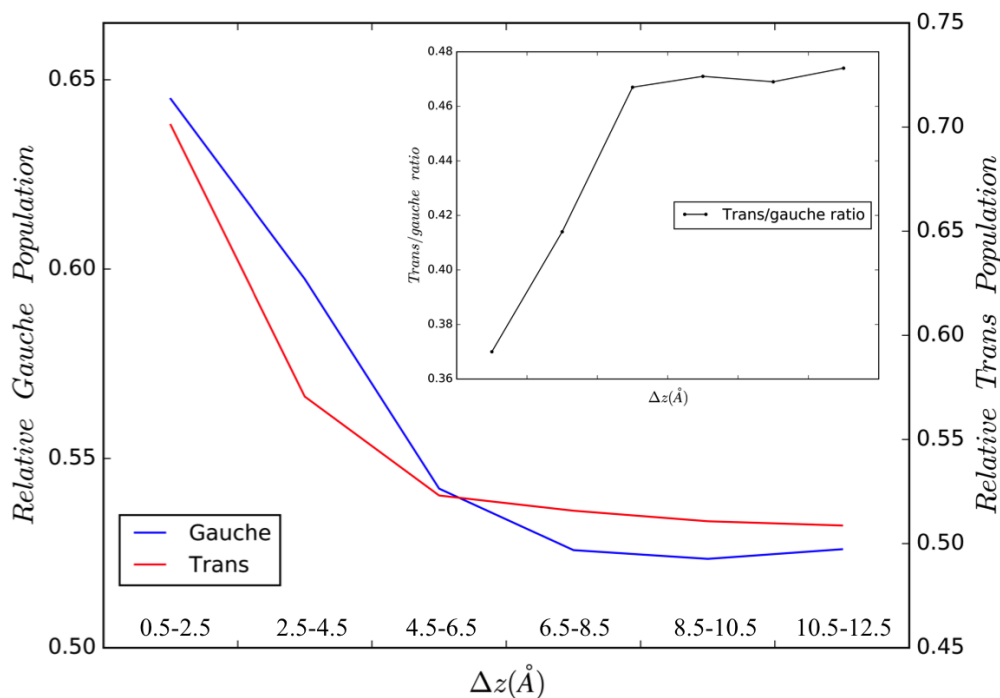


Figure 4.12: Relative population within the intensified region marked by the dashed rectangular box for *gauche* (blue line, left axis) and *trans* DCE (red line, right axis) in the respective orientation profiles in Figure 4.11. The definition of these regions are same as for the local DCE population. The population of each slab with respect to the *gauche* or *trans* profile is normalized by the overall number of DCE molecules within the same layer. The inset graph shows the *trans/gauche* ratio as a function of vertical distance to instantaneous LLI.

the normalization notation in Figure 4.8, all histograms are normalized by the respective *gauche* and *trans* molecular numbers in slabs relative to the experimental *gauche* and *trans* molecular number density, which are $N_{slab}^{gauche} / N_{\rho}^{gauche}$ and $N_{slab}^{trans} / N_{\rho}^{trans}$ respectively. Here $N_{\rho}^{gauche} = N_{\rho}^{DCE} \cdot \omega^{gauche}$ and $N_{\rho}^{trans} = N_{\rho}^{DCE} \cdot \omega^{trans}$, with ω^{gauche} and ω^{trans} calculated from the experimental *trans/gauche* ratio $\omega = 34.9\%$.

In Figure 4.12, the quantitative analyses of the orientation distribution for *gauche* (blue line) and *trans* DCE (red line) demonstrate that the preferred orientations of *gauche* and *trans* DCE vanish in an almost

identical manner from the interface into the bulk. It should be noticed here that the *trans* DCE should not show a preference by itself due to its vanishing dipole moment. The orientational effect in the *trans* profile is due to internal rotations between *gauche* and *trans* DCEs. This means that the *trans* orientation is because of molecules which are oriented while in the *gauche* state and then rotate internally to become a *trans* DCE without overall reorientation occurring quickly enough to lose the orientational order. The *trans/gauche* ratio in the inset graph of Figure 4.12 is rapidly increasing from the value within the interfacial layers to a value of ~ 0.47 , which is approximately the calculated value of the bulk *trans/gauche* ratio in Chapter 3. This quantitatively confirms that there are more *gauche* conformers in the water/DCE LLI than in the bulk DCE, which is also in accordance with the peak of the molecular density profile of DCE in the interface region in 4.3.

4.3.5 Perpendicular Dielectric Permittivity Tensor

Contrary to the parallel dielectric permittivity profile, the perpendicular dielectric responses rather seem like fluctuating around a mixed average dielectric permittivity value as seen from Figure 4.13. Comparing with the perpendicular dielectric profile with respect to the average Gibbs dividing interface (bottom panel) only showing an average dielectric value, our perpendicular dielectric profiles referenced to the instantaneous LLI furthermore capture enhancements within the interface regions, as seen in the top panels of Figure 4.13. This tells us that the molecular structure along the z -axis within the small length scale of the instantaneous interface has a strong ordering behavior. The average perpendicular dielectric permittivity does not come unexpectedly as the perpendicular dielectric permittivity tensor is generally acknowledged to be rather difficult to extract. This is due to the reason that very small changes in the polarization correlation function $h_{\perp}(\Delta z)$ can lead to tremendous changes in the numerical calculation of $\epsilon_{\perp}(\Delta z)$.

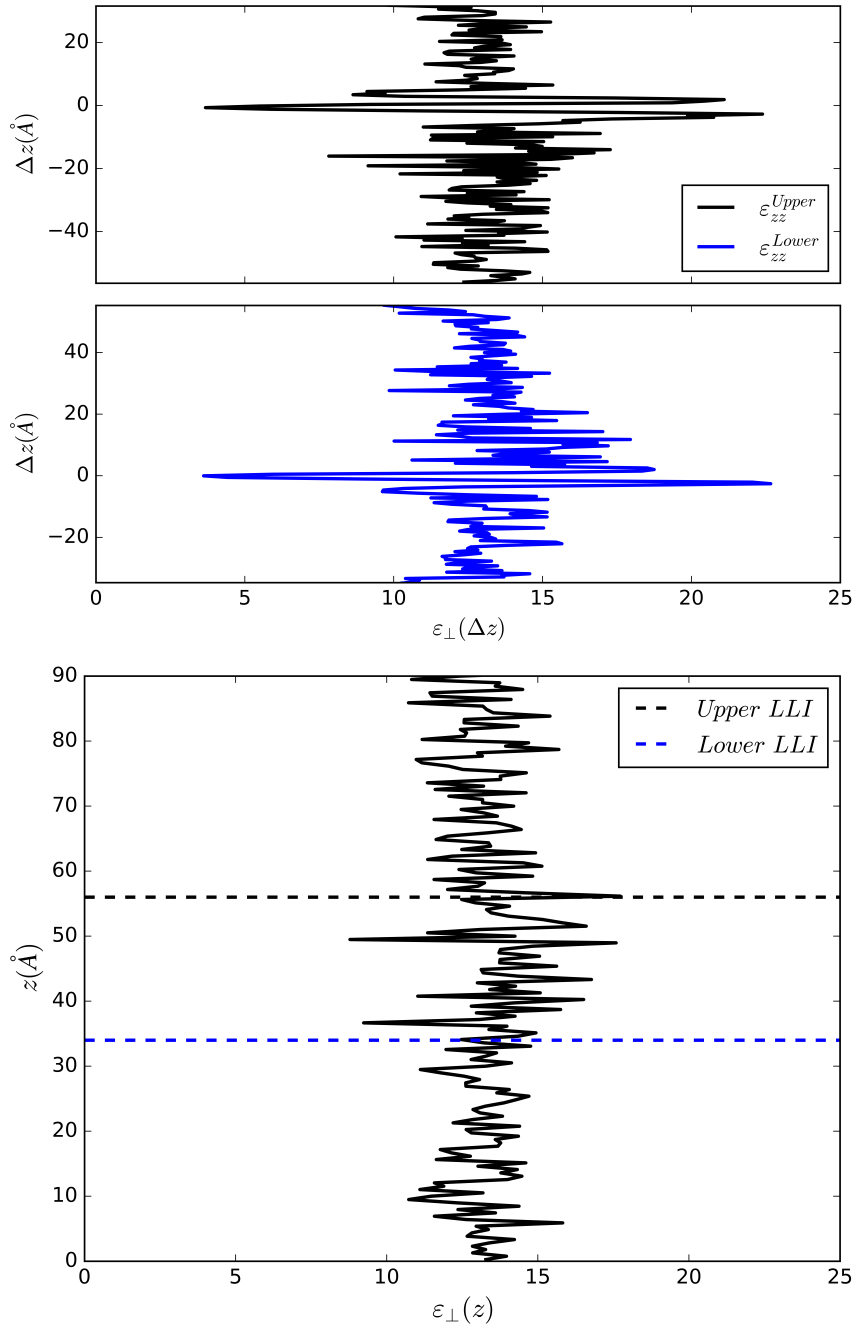


Figure 4.13: Perpendicular dielectric profiles ($\epsilon_{\perp}(\Delta z)$, two top panels) with respect to the distances normal to the lower (blue) and upper (black) instantaneous interface. The zero locations are approximately the reference instantaneous interfaces. The bottom panel shows for comparison the perpendicular dielectric permittivity as a function of z referenced to the average Gibbs dividing interface. The black and blue dashed lines show the respective upper and lower LLI, corresponding to the zero locations in the two top panels.

It is important to mention that the dielectric response is dominated by the polarization correlation functions as shown in Equ. 4.1. Therefore, in Figure 4.14 we plot the correlation function $h_{zz}(z)$ itself, along with the values corresponding to various dielectric constants obtained from Equ. 4.4 as a reference. Different from the observation for the perpendicular polarization correlation profile for the case of the solid-liquid interface where $h_{\perp}(\Delta z)$ passes through zero several times[32, 35], the profile of $h_{\perp}(\Delta z)$ never passes through zero in this study. Therefore, the inverse term $\epsilon_{\perp}^{-1}(\Delta z)$ does not exhibit singularities and extensive negative parts, which confirms Equ. 4.3. Even though following exactly Equ. 4.3 and other previously employed expressions[35, 42, 46], we still fail in the extraction of the orthogonal component of the dielectric permittivity tensor, which is in line with previous findings[42, 43, 46].

The reason why we obtain an average perpendicular dielectric permittivity tensor may come from the current widely used continuum theory, which we introduced in Chapter 2, not theoretically well-established for the specific heterogeneous LLI system. Especially from our result of the perpendicular permittivity profile, the approximation of the constant field in the respective high-dielectric and low-dielectric phases may be questionable. This assumption will be investigated by the varying perpendicular dielectric permittivity of the central water phase with different thickness of the water phase and. This will be discussed in the following.

Since our simulation system is only anisotropic in the z dimension, we extend the water and DCE phases to elucidate how this anisotropy affects the perpendicular dielectric response in the respective central phase. We perform a series of LLI simulations, keeping the original box size in x and y dimensions as well as the thickness along z of the DCE phase ($\approx 68 \text{ \AA}$), only changing the thickness of the water phase. The studied thicknesses are approximately 11, 22, 88, 154, 220, 250 \AA , which will change the distance of the center of the water phase

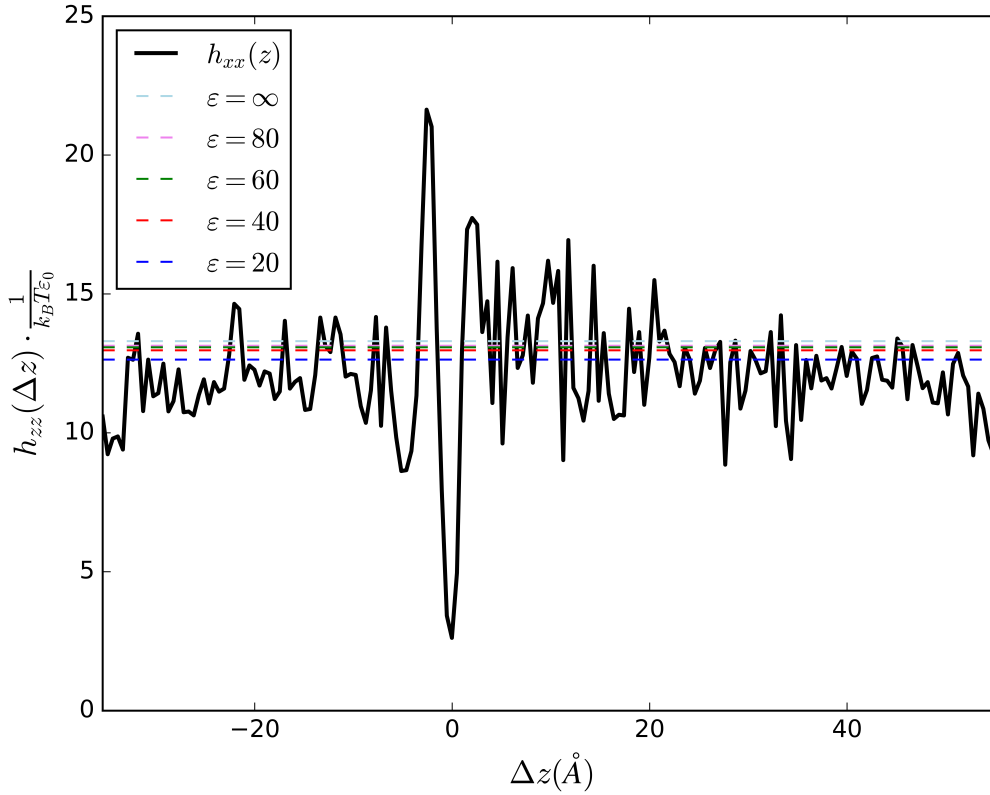


Figure 4.14: The polarization correlation function $h_{zz}(\Delta z)$ as a function of the distance normal to the lower instantaneous interface, along with that corresponding to various dielectric constants from Eq. 4.4

to the LLI as a result. Here we calculate the dielectric permittivity of the central slabs of the water phases using the procedure described in Section 4.2.1, but only taking the water molecular dipole contributions into account. The extracted dielectric permittivity tensors are given in Figure 4.15. It shows the value of the parallel dielectric permittivity tensor components ϵ_{xx} and ϵ_{yy} and the perpendicular permittivity in the z direction ϵ_{zz} of the central water phase as a function of vertical distance to the interface in a series of LLI simulations. The parallel dielectric permittivity tensor components all reproduce the approximate bulk water dielectric constant, while ϵ_{zz} calculated in the same central layers first increases significantly with increasing the thickness of the

4. INTRINSIC LIQUID-LIQUID INTERFACE

simulated water phase in the z direction and then reaches a plateau after the thickness grows beyond 20 nm. This finding is not due to the limited system sizes of the MD simulations. It is important to mention that if we take out the central water region from the simulated water phases, and analyze this water box as if it was a simulation of the pure water. We can obtain the expected normal water dielectric constant. But for the same water/DCE LLI simulation, we only get average perpendicular dielectric profile in Figure 4.13 and a much lower perpendicular dielectric tensor component for water in Figure 4.15. This indicates that there are problems with the assumptions invoked in the treatment of the statistics for the calculation of the perpendicular dielectric permittivity tensor for the specific heterogeneous LLI system.

Let's revisit the theory in Chapter 2, where we assume the perturbation field is due to the same molecular motions as the reaction field. Basing on the fact that dielectric permittivity is frequency dependent, this assumption only works when the perturbation field oscillate at the same frequency at which the medium can respond. For our specific water/DCE LLI, there are two different types of molecules with two intrinsic different molecular dipole reorientation frequencies. In such a system, ϵ responds to frequencies of the reorientation of molecular dipoles. If the response and the field cannot perfectly overlap, ϵ does not respond for all dipole oscillations, which will result in a lower dielectric permittivity. For the bulk or solid-(one) liquid simulations, there is only one type of molecule and one dipole reorientation frequency, which means the assumption of identical simulation and response frequency is naturally fulfilled. But for the anisotropic LLI system, this approximation may have been broken. In addition, it should be mentioned that even though varying the thickness of the DCE phase in a related set of simulations, the perpendicular dielectric constant of the central DCE phase always stays around 10, which is approximately the dielectric constant of the pure DCE liquid. This finding seems to

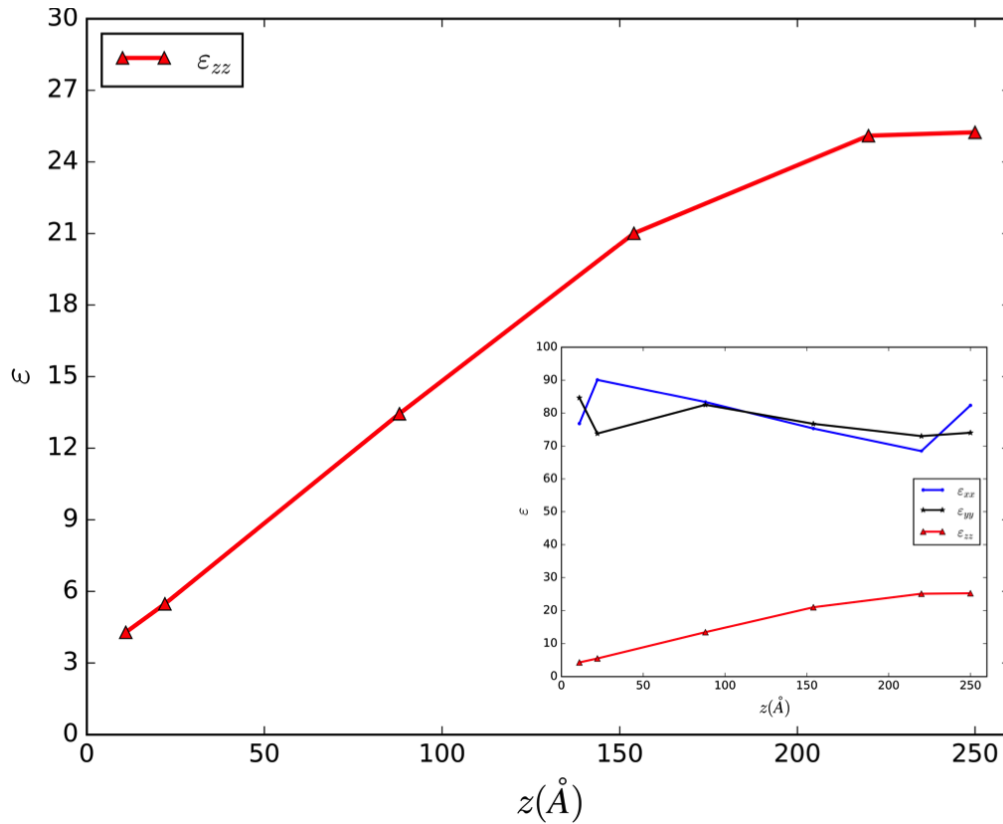


Figure 4.15: Perpendicular dielectric permittivity at the center of the water phase as a function of the thickness of the water phase in water/DCE LLI simulations. The small inset graph shows the parallel dielectric tensor components in the same situation.

indicate that the water phase has no impact on DCE's static dielectric constant. This microscopically indicates that water molecules vibrate faster than DCE molecules, which results in a varying induced electric field with frequency that will be averaged out over the time scale seen by a DCE molecule. Thus DCE molecules never see the constant displacement field and keep its static field. Given the comparatively slow vibrations, DCE molecules will have a particular orientation. This will generate a static electric field in the water phase seen from the inertial system of a water molecule. The impact of this electric field on water changes with the distance to the interface, which is large

at the interface and is decreasing with increasing distance from the interface further into the water central phase. However to formalize this spatial dependence of the dielectric permittivity tensor would be tricky because of the undetermined volume fraction in terms of the electric field. Even so, the above analysis is at least a hint for the understanding of the perpendicular dielectric permittivity profile of heterogeneous LLI systems.

4.4 Conclusion to Chapter 4

In conclusion, we have presented a methodology to extract the static dielectric permittivity profile from the correlations between the system's dipole moment fluctuations and the local polarization density for a water/DCE LLI that is nonuniform along the z axis. All these correlations are calculated from classical MD atomic coordinates. The novel aspect of our analyses is an appraisal of the difference between the coordinates based on the coarse grained theoretical framework of an instantaneous interface and one based on the average Gibbs dividing interface, which is examined by the molecular density, the dielectric permittivity profiles and molecular orientation profiles respectively. At the LLI, occasional penetration of the interfacial molecules into each other's phase leads to the interfacial layers roughening and a broadened interfacial region. This effect of the "fingering" phenomenon is enough to smear out any response properties within the vicinity of the interface. For studies that purport to show the response of physical properties of moieties (e.g. nanoparticles) embedded in such interfaces, we need to take the anisotropy between the two liquid phases into account appropriately. For meaningful statistical analyses of interface effects on the response properties, they always have to be referenced to the closest interface and the distance between such interfaces in a simulation needs to be large enough to reach true bulk behavior.

Our MD simulation results of the water/DCE LLI demonstrate that the long-range response properties such as the dielectric permittivity tensor with respect to the instantaneous interfaces having intrinsic responses, which can not be dealt with through the average Gibbs dividing interface reference. Referencing to the instantaneous interface, we obtain an enhanced parallel dielectric permittivity tensor at the interface. The mechanism behind this overshooting response is the interfacial molecular orientation. In the vicinity of the water/DCE LLI, molecules show nonuniform orientation and result in an oriented molecular dipole density because of the nonuniform molecular environment. We can conclude that the preference of the molecular arrangements of the two involved phases of the LLI are consequences of the effect induced by the charge distributions of the respective molecules in the vicinity of the interface. This makes the dielectric permittivity tensor not as simple as the isotropic case. The finding is confirmed experimentally by atomic force microscopy to measure the interfacial water dielectric permittivity profile, where the variable permittivity profile suggested a reorientation of the water molecule dipoles in the presence of the interface.[154] We expect our observation to extend a clear understanding about the dielectric behavior of the LLI and may provide detailed insights into a further theoretical investigation on the mechanism of the important subject of the dielectric permittivity for the liquid-vapor, solid-liquid or confined liquid simulations.

Chapter 5

Summary & Outlook

In conclusion, the work throughout the course of this thesis presents an example of an effective fitting approach for the derivation of geometric parameters for a set of important CHCs to reproduce accurate dielectric constants without sacrificing the well-reproduced properties of the existing OPLS-AA models. The improvement of the dielectric constants is achieved due to the fact that the atomic partial charges and thereby the molecular dipole moments are improved via the RESP approach based on first-principle computations; systematically improved torsional potential energy surface cuts for the internal degree of freedom in the flexible DCE molecules are constructed by adjusting the torsional potential parameters to match corresponding first-principle calculations and cross-validated based on rotational conformational distributions from short MD simulations. For the prototype model molecule 1,2-DCE, we also develop a polarizable model based on the classical Drude oscillator model by assigning the polarizability to the carbon atom site, in order to capture the electronic polarization incurred by a soft internal degree of freedom explicitly. What should be noted here is that the development of the 1,2-DCE-DO model gave rise to challenges concerning the torsional potential coefficients fitting approach. Instead of a direct first-principles-driven parametrization of the polarizable

5. SUMMARY & OUTLOOK

model, a careful modification of the torsion potential coefficients starting from the NP parametrization proved to be crucial. This allows the DO model to remedy some problems with correlations among physical properties observed in the reparametrization of the NP force field.[123] The efficient and effective force field reparametrization methodology developed here might be useful in deriving and improving further force fields for molecules relevant in applications that are sensitive to response properties.

Using the new reparametrized force field, we analyze the dynamic properties of the water/1,2DCE liquid liquid interface by molecular dynamics simulations. We present a relation between the dielectric permittivity tensor and the correlations between the system's total dipole moment and the local polarization fluctuations. The general description of the dielectric response using the average Gibbs dividing interface will lose valuable information of the interfacial structure, hence a striking calculation within the course of this thesis is that we have established the calculation of this dielectric profile with a coarse grained theoretical framework of the instantaneous interface. This approach allows us to eliminate the fluctuations of the interface location caused by capillary wave thermal fluctuations. This way we can obtain statistics extracted from MD simulations with significantly higher accuracy than in previous works based on the usual average interface. Our computer simulations of the instantaneous LLI show the parallel dielectric permittivity profile to exhibit large deviations from bulk behavior in the interfacial region. Via the bivariate distributions of the molecular orientations in the vicinity of the LLI, we can conclude that this overshooting response upon approaching the interface owes partial preferential molecular orientation effects in the vicinity of the LLI.

As an Outlook, for the perpendicular dielectric permittivity profile, although we expect it to relate to the interface statistics as much

the parallel dielectric profile does, our preliminary simulation results demonstrate that the interface effect is a much more long-range property than one might think. Apparently it much exceeds the actual thickness of the interface layers of some tens of nanometers. The systematic procedure to extract the perpendicular dielectric permittivity profile for the anisotropic LLI needs to be better established though to validate this notion. For example, the constant displacement field approximation is highly questionable for the inhomogenous simulation system that is nonuniform in the dimension in which the displacement field lies.[33] Furthermore, from our theoretical modeling point of view, the dielectric response of the polarized water/1,2-DCE-DO interface would be a promising topic with our developed polarizable model, such as the polarization field analysis and dielectric permittivity response property within this simulation system.

Bibliography

- [1] Alexander G Volkov and David W Deamer. *Liquid-liquid interfaces Theory and methods*. CRC press, 1996.
- [2] HHJ Girault and DJ Schiffrin. Thermodynamics of a polarised interface between two immiscible electrolyte solutions. *Journal of Electroanalytical Chemistry and Interfacial Electrochemistry*, 170(1-2):127–141, 1984.
- [3] HH Girault. Electrochemistry at the interface between two immiscible electrolyte solutions. *Electrochimica Acta*, 32(3):383–385, 1987.
- [4] Mitsugi Senda, Takashi Kakiuchi, and Toshiyuki Osaka. Electrochemistry at the interface between two immiscible electrolyte solutions. *Electrochimica Acta*, 36(2):253–262, 1991.
- [5] Zdenek Samec. Electrical double layer at the interface between two immiscible electrolyte solutions. *Chemical Reviews*, 88(4):617–632, 1988.
- [6] Jacob Israelachvili and Hakan Wennerstrom. Role of hydration and water structure in biological and colloidal interactions. *Nature*, 379(6562):219, 1996.

- [7] Daniel K Beaman, Ellen J Robertson, and Geraldine L Richmond. Ordered polyelectrolyte assembly at the oil-water interface. *Proceedings of the National Academy of Sciences of the United States of America*, 109(9):3226–3231, 2012.
- [8] Ilan Benjamin. *Reactivity and dynamics at liquid interfaces*, volume 28. Wiley: Chichester, 2015.
- [9] John Shipley Rowlinson and Benjamin Widom. *Molecular theory of capillarity*. Courier Corporation, 2013.
- [10] Ilan Benjamin. Theoretical study of the water/1,2-dichloroethane interface: Structure, dynamics, and conformational equilibria at the liquid-liquid interface. *The Journal of Chemical Physics*, 97(2):1432–1445, 1992.
- [11] Ilan Benjamin. Molecular structure and dynamics at liquid-liquid interfaces. *Annual Review of Physical Chemistry*, 48(1):407–451, 1997.
- [12] G Taylor and HHJ Girault. Ion transfer reactions across a liquid-liquid interface supported on a micropipette tip. *Journal of Electroanalytical Chemistry and Interfacial Electrochemistry*, 208(1):179–183, 1986.
- [13] Takeshi Shioya, Seiichi Nishizawa, and Norio Teramae. Anion recognition at the liquid-liquid interface. sulfate transfer across the 1,2-dichloroethane-water interface facilitated by hydrogen-bonding ionophores. *Journal of the American Chemical Society*, 120(44):11534–11535, 1998.
- [14] Tsun-Mei Chang and Liem X Dang. Molecular dynamics simulations of ccl₄-h₂o liquid-liquid interface with polarizable potential models. *The Journal of Chemical Physics*, 104(17):6772–6783, 1996.

-
- [15] KB Eienthal. Liquid interfaces probed by second-harmonic and sum-frequency spectroscopy. *Chemical Reviews*, 96(4):1343–1360, 1996.
- [16] Alexander G Volkov. *Liquid interfaces in chemical, biological and pharmaceutical applications*. CRC Press, 2001.
- [17] David Michael and Ilan Benjamin. Molecular dynamics computer simulations of solvation dynamics at liquid/liquid interfaces. *The Journal of Chemical Physics*, 114(6):2817–2824, 2001.
- [18] Liem X Dang. Computer simulation studies of ion transport across a liquid/liquid interface. *The Journal of Physical Chemistry B*, 103(39):8195–8200, 1999.
- [19] Tsun-Mei Chang and Liem X Dang. Recent advances in molecular simulations of ion solvation at liquid interfaces. *Chemical Reviews*, 106(4):1305–1322, 2006.
- [20] Daniel A Higgins and Robert M Corn. Second harmonic generation studies of adsorption at a liquid-liquid electrochemical interface. *The Journal of Physical Chemistry*, 97(2):489–493, 1993.
- [21] José L Rivera, Clare McCabe, and Peter T Cummings. Molecular simulations of liquid-liquid interfacial properties: Water–*n*-alkane and water-methanol–*n*-alkane systems. *Physical Review E*, 67(1):011603, 2003.
- [22] Pál Jedlovszky, Árpád Vincze, and George Horvai. New insight into the orientational order of water molecules at the water/1,2-dichloroethane interface: A monte carlo simulation study. *The Journal of Chemical Physics*, 117(5):2271–2280, 2002.
- [23] R Hidalgo-Alvarez, A Martin, A Fernandez, D Bastos, F Martinez, and FJ De Las Nieves. Electrokinetic properties, colloidal stability

and aggregation kinetics of polymer colloids. *Advances in Colloid and Interface Science*, 67:1–118, 1996.

- [24] Yaakov Levy and José N Onuchic. Water mediation in protein folding and molecular recognition. *Annual Review of Biophysics and Biomolecular Structure*, 35:389–415, 2006.
- [25] Phillip W Snyder, Jasmin Mecinović, Demetri T Moustakas, Samuel W Thomas, Michael Harder, Eric T Mack, Matthew R Lockett, Annie Héroux, Woody Sherman, and George M Whitesides. Mechanism of the hydrophobic effect in the biomolecular recognition of arylsulfonamides by carbonic anhydrase. *Proceedings of the National Academy of Sciences of the United States of America*, 108(44):17889–17894, 2011.
- [26] John G Kirkwood. The dielectric polarization of polar liquids. *The Journal of Chemical Physics*, 7(10):911–919, 1939.
- [27] Herbert Fröhlich. *Theory of dielectrics: dielectric constant and dielectric loss*. Clarendon Press, 1958.
- [28] Carl Johan Friedrich Böttcher, Oenes Christoffel van Belle, Paul Bordewijk, and Arie Rip. *Theory of electric polarization*, volume 2. Elsevier Science Ltd, 1978.
- [29] Peter A Kollman, Irina Massova, Carolina Reyes, Bernd Kuhn, Shuanghong Huo, Lillian Chong, Matthew Lee, Taisung Lee, Yong Duan, Wei Wang, et al. Calculating structures and free energies of complex molecules: combining molecular mechanics and continuum models. *Accounts of Chemical Research*, 33(12):889–897, 2000.
- [30] Mitsunori Kato, Andrei V Pisliakov, and Arieh Warshel. The barrier for proton transport in aquaporins as a challenge for electrostatic models: the role of protein relaxation in mutational

- calculations. *Proteins: Structure, Function, and Bioinformatics*, 64(4):829–844, 2006.
- [31] Lin Li, Chuan Li, Zhe Zhang, and Emil Alexov. On the dielectric “constant” of proteins: smooth dielectric function for macromolecular modeling and its implementation in delphi. *Journal of Chemical Theory and Computation*, 9(4):2126, 2013.
- [32] Alexander Schlaich, Ernst W Knapp, and Roland R Netz. Water dielectric effects in planar confinement. *Physical Review Letters*, 117(4):048001, 2016.
- [33] Douwe Jan Bonthuis and Roland R Netz. Beyond the continuum: how molecular solvent structure affects electrostatics and hydrodynamics at solid–electrolyte interfaces. *The Journal of Physical Chemistry B*, 117(39):11397–11413, 2013.
- [34] Douwe Jan Bonthuis, Stephan Gekle, and Roland R Netz. Profile of the static permittivity tensor of water at interfaces: Consequences for capacitance, hydration interaction and ion adsorption. *Langmuir*, 28(20):7679–7694, 2012.
- [35] Douwe Jan Bonthuis, Stephan Gekle, and Roland R Netz. Dielectric profile of interfacial water and its effect on double-layer capacitance. *Physical Review Letters*, 107(16):166102, 2011.
- [36] Stefan Ringe, Harald Oberhofer, and Karsten Reuter. Transferable ionic parameters for first-principles poisson-boltzmann solvation calculations: Neutral solutes in aqueous monovalent salt solutions. *The Journal of Chemical Physics*, 146(13):134103, 2017.
- [37] Daniel Berger, Andrew J Logsdail, Harald Oberhofer, Matthew R Farrow, C Richard A Catlow, Paul Sherwood, Alexey A Sokol, Volker Blum, and Karsten Reuter. Embedded-cluster calculations

in a numeric atomic orbital density-functional theory framework. *The Journal of Chemical Physics*, 141(2):024105, 2014.

- [38] Maria Francesca Iozzi, Maurizio Cossi, Roberto Improta, Nadia Rega, and Vincenzo Barone. A polarizable continuum approach for the study of heterogeneous dielectric environments. *The Journal of Chemical Physics*, 124(18):184103, 2006.
- [39] Verónica M Sánchez, Mariela Sued, and Damián A Scherlis. First-principles molecular dynamics simulations at solid-liquid interfaces with a continuum solvent. *The Journal of Chemical Physics*, 131(17):174108, 2009.
- [40] KJ Tielrooij, D Paparo, L Piatkowski, HJ Bakker, and M Bonn. Dielectric relaxation dynamics of water in model membranes probed by terahertz spectroscopy. *Biophysical Journal*, 97(9):2484–2492, 2009.
- [41] U Heugen, G Schwaab, E Bründermann, M Heyden, X Yu, DM Leitner, and Martina Havenith. Solute-induced retardation of water dynamics probed directly by terahertz spectroscopy. *Proceedings of the National Academy of Sciences of the United States of America*, 103(33):12301–12306, 2006.
- [42] V Ballenegger and J-P Hansen. Local dielectric permittivity near an interface. *Europhysics Letters*, 63(3):381, 2003.
- [43] Harry A Stern and Scott E Feller. Calculation of the dielectric permittivity profile for a nonuniform system: application to a lipid bilayer simulation. *The Journal of Chemical Physics*, 118(7):3401–3412, 2003.
- [44] V Ballenegger and J-P Hansen. Dielectric permittivity profiles of confined polar fluids. *The Journal of Chemical Physics*, 122(11):114711, 2005.

-
- [45] Allan D Friesen and Dmitry V Matyushov. Local polarity excess at the interface of water with a nonpolar solute. *Chemical Physics Letters*, 511(4):256–261, 2011.
- [46] Aziz Ghoufi, Anthony Szymczyk, Richard Renou, and Minxia Ding. Calculation of local dielectric permittivity of confined liquids from spatial dipolar correlations. *Europhysics Letters*, 99(3):37008, 2012.
- [47] Stanislav Parez, Milan Predota, and Michael Machesky. Dielectric properties of water at rutile and graphite surfaces: effect of molecular structure. *The Journal of Physical Chemistry C*, 118(9):4818–4834, 2014.
- [48] Olle Bjoernehholm, Martin H Hansen, Andrew Hodgson, Li-Min Liu, David T Limmer, Angelos Michaelides, Philipp Pedevilla, Jan Rossmeisl, Huaze Shen, Gabriele Tocci, et al. Water at interfaces. *Chemical Reviews*, 116(13):7698–7726, 2016.
- [49] Shunhao Xiao, Florian Figge, Guillaume Stirnemann, Damien Laage, and John A McGuire. Orientational dynamics of water at an extended hydrophobic interface. *Journal of the American Chemical Society*, 138(17):5551–5560, 2016.
- [50] John David Jackson and Ronald F Fox. Classical electrodynamics. *American Journal of Physics*, 67(9):841–842, 1999.
- [51] R Evans. The nature of the liquid-vapor interface and other topics in the statistical mechanics of non-uniform, classical fluids. *Advances in Physics*, 28(2):143–200, 1979.
- [52] Frank H Stillinger. Capillary waves and the inherent density profile for the liquid-vapor interface. *The Journal of Chemical Physics*, 76(2):1087–1091, 1982.

- [53] Scott W Sides, Gary S Grest, and Martin-D Lacasse. Capillary waves at liquid-vapor interfaces: A molecular dynamics simulation. *Physical Review E*, 60(6):6708, 1999.
- [54] Dragoslav M Mitrinović, Aleksey M Tikhonov, Ming Li, Zhengqing Huang, and Mark L Schlossman. Noncapillary-wave structure at the water-alkane interface. *Physical Review Letters*, 85(3):582, 2000.
- [55] Ahmed E Ismail, Gary S Grest, and Mark J Stevens. Capillary waves at the liquid-vapor interface and the surface tension of water. *The Journal of Chemical Physics*, 125(1):014702, 2006.
- [56] Sanjib Senapati and Max L Berkowitz. Computer simulation study of the interface width of the liquid/liquid interface. *Physical Review Letters*, 87(17):176101, 2001.
- [57] E Chacón and P Tarazona. Intrinsic profiles beyond the capillary wave theory: A monte carlo study. *Physical Review Letters*, 91(16):166103, 2003.
- [58] Fernando Bresme, Enrique Chacón, and Pedro Tarazona. Molecular dynamics investigation of the intrinsic structure of water-fluid interfaces via the intrinsic sampling method. *Physical Chemistry Chemical Physics*, 10(32):4704–4715, 2008.
- [59] Marcello Sega, Balázs Fábián, and Pál Jedlovszky. Layer-by-layer and intrinsic analysis of molecular and thermodynamic properties across soft interfaces. *The Journal of Chemical Physics*, 143(11):114709, 2015.
- [60] Sotiris S Xantheas and Gregory A Voth. *Aqueous solutions and their interfaces*, 2009.
- [61] Rémi Khatib, Ellen HG Backus, Mischa Bonn, María-José Pérez-Haro, Marie-Pierre Gageot, and Marialore Sulpizi. *Water*

- orientation and hydrogen-bond structure at the fluorite/water interface. *Scientific Reports*, 6, 2016.
- [62] Sandeep Patel and Charles L Brooks III. Structure, thermodynamics, and liquid-vapor equilibrium of ethanol from molecular-dynamics simulations using nonadditive interactions. *The Journal of Chemical Physics*, 123(16):164502, 2005.
- [63] Fernando Bresme, Enrique Chacón, Pedro Tarazona, and Kafui Tay. Intrinsic structure of hydrophobic surfaces: The oil-water interface. *Physical Review Letters*, 101(5):056102, 2008.
- [64] György Hantal, Mária Darvas, Livia B Partay, George Horvai, and Pál Jedlovszky. Molecular level properties of the free water surface and different organic liquid/water interfaces, as seen from itim analysis of computer simulation results. *Journal of Physics: Condensed Matter*, 22(28):284112, 2010.
- [65] Livia B Pártay, György Hantal, Pál Jedlovszky, Árpád Vincze, and George Horvai. A new method for determining the interfacial molecules and characterizing the surface roughness in computer simulations. application to the liquid-vapor interface of water. *Journal of Computational Chemistry*, 29(6):945–956, 2008.
- [66] Maria Darvas, Miguel Jorge, M Natalia DS Cordeiro, Sofia S Kantorovich, Marcello Sega, and Pal Jedlovszky. Calculation of the intrinsic solvation free energy profile of an ionic penetrant across a liquid-liquid interface with computer simulations. *The Journal of Physical Chemistry B*, 117(50):16148–16156, 2013.
- [67] Adam P Willard and David Chandler. Instantaneous liquid interfaces. *The Journal of Physical Chemistry B*, 114(5):1954–1958, 2010.

- [68] Christopher J Fennell, Libo Li, and Ken A Dill. Simple liquid models with corrected dielectric constants. *The Journal of Physical Chemistry B*, 116(23):6936–6944, 2012.
- [69] Pedro EM Lopes, Edward Harder, Benoît Roux, and Alexander D Mackerell Jr. Formalisms for the explicit inclusion of electronic polarizability in molecular modeling and dynamics studies. In *Multi-Scale Quantum Models for Biocatalysis*, pages 219–257. Springer, 2009.
- [70] William L Jorgensen, Robert C Binning Jr, and Bernard Bigot. Structures and properties of organic liquids: n-butane and 1,2-dichloroethane and their conformation equilibriums. *Journal of the American Chemical Society*, 103(15):4393–4399, 1981.
- [71] Y Taniguchi, H Takaya, PTT Wong, and E Whalley. Effect of pressure on molecular conformations. ii. trans–gauche equilibrium of 1,2-dichloroethane and 1,2-dibromoethane. *The Journal of Chemical Physics*, 75(10):4815–4822, 1981.
- [72] Kuan-Huang Kuo, Yi-Shiue Lin, Jain-Jung Shih, Yung-Hsuan Liao, Jian-Shiun Lin, Che-Ming Yang, and Jong-Liang Lin. 1,2-dichloroethane on cu (100) and oxygen-covered cu (100): Conformation, orientation, and transformation. *The Journal of Physical Chemistry C*, 111(21):7757–7764, 2007.
- [73] N Arul Murugan, Håkan Wilhelm Hugosson, and Hans Ågren. Solvent dependence on conformational transition, dipole moment, and molecular geometry of 1,2-dichloroethane: insight from car-parrinello molecular dynamics calculations. *The Journal of Physical Chemistry B*, 112(47):14673–14677, 2008.
- [74] Frank Jose Salas, G Arlette Mendez-Maldonado, Edgar Nunez-Rojas, Gabriel Eloy Aguilar-Pineda, Hector Domínguez, and Jose

- Alejandre. Systematic procedure to parametrize force fields for molecular fluids. *Journal of Chemical Theory and Computation*, 11(2):683–693, 2015.
- [75] C Millot and JL Rivail. Molecular dynamics simulation of conformational equilibrium of 1,2-dichloroethane. *Journal of Molecular Liquids*, 43:1–11, 1989.
- [76] William L Jorgensen, David S Maxwell, and Julian Tirado-Rives. Development and testing of the opls all-atom force field on conformational energetics and properties of organic liquids. *Journal of the American Chemical Society*, 118(45):11225–11236, 1996.
- [77] Stephen D Fried, Lee-Ping Wang, Steven G Boxer, Pengyu Ren, and Vijay S Pande. Calculations of the electric fields in liquid solutions. *The Journal of Physical Chemistry B*, 117(50):16236–16248, 2013.
- [78] Rafael A Zubillaga, Ariana Labastida, Bibiana Cruz, Juan Carlos Martínez, Enrique Sanchez, and Jose Alejandre. Surface tension of organic liquids using the opls/aa force field. *Journal of Chemical Theory and Computation*, 9(3):1611–1615, 2013.
- [79] Siyan Chen, Shasha Yi, Wenmei Gao, Chuncheng Zuo, and Zhonghan Hu. Force field development for organic molecules: Modifying dihedral and 1-n pair interaction parameters. *Journal of Computational Chemistry*, 36(6):376–384, 2015.
- [80] Joseph Costandy, Vasileios K Michalis, Ioannis N Tsimpanogiannis, Athanassios K Stubos, and Ioannis G Economou. The role of intermolecular interactions in the prediction of the phase equilibria of carbon dioxide hydrates. *The Journal of Chemical Physics*, 143(9):094506, 2015.

- [81] William L Jorgensen and Julian Tirado-Rives. Potential energy functions for atomic-level simulations of water and organic and biomolecular systems. *Proceedings of the National Academy of Sciences of the United States of America*, 102(19):6665–6670, 2005.
- [82] Junmei Wang, Romain M Wolf, James W Caldwell, Peter A Kollman, and David A Case. Development and testing of a general amber force field. *Journal of Computational Chemistry*, 25(9):1157–1174, 2004.
- [83] Carl Caleman, Paul J van Maaren, Minyan Hong, Jochen S Hub, Luciano T Costa, and David van der Spoel. Force field benchmark of organic liquids: density, enthalpy of vaporization, heat capacities, surface tension, isothermal compressibility, volumetric expansion coefficient, and dielectric constant. *Journal of Chemical Theory and Computation*, 8(1):61–74, 2011.
- [84] William L Jorgensen, Nora A McDonald, Massimo Selmi, and Paul R Rablen. Importance of polarization for dipolar solutes in low-dielectric media: 1,2-dichloroethane and water in cyclohexane. *Journal of the American Chemical Society*, 117(47):11809–11810, 1995.
- [85] Kenno Vanommeslaeghe, Elizabeth Hatcher, Chayan Acharya, Sibsankar Kundu, Shijun Zhong, Jihyun Shim, Eva Darian, Olgun Guvench, P Lopes, Igor Vorobyov, et al. Charmm general force field: A force field for drug-like molecules compatible with the charmm all-atom additive biological force fields. *Journal of Computational Chemistry*, 31(4):671–690, 2010.
- [86] FL Ning, K Glavatskiy, Z Ji, S Kjelstrup, and TJ H Vlught. Compressibility, thermal expansion coefficient and heat capacity of ch 4 and co 2 hydrate mixtures using molecular dynamics simulations. *Physical Chemistry Chemical Physics*, 17(4):2869–2883, 2015.

-
- [87] David van der Spoel, Paul J van Maaren, and Carl Caleman. Gromacs molecule & liquid database. *Bioinformatics*, 28(5):752–753, 2012.
- [88] Guillaume Lamoureux, Alexander D MacKerell Jr, and Benoit Roux. A simple polarizable model of water based on classical drude oscillators. *The Journal of Chemical Physics*, 119(10):5185–5197, 2003.
- [89] Igor V Vorobyov, Victor M Anisimov, and Alexander D MacKerell. Polarizable empirical force field for alkanes based on the classical drude oscillator model. *The Journal of Physical Chemistry B*, 109(40):18988–18999, 2005.
- [90] Liem X Dang and Tsun-Mei Chang. Molecular dynamics study of water clusters, liquid, and liquid-vapor interface of water with many-body potentials. *The Journal of Chemical Physics*, 106(19):8149–8159, 1997.
- [91] Guillaume Lamoureux and Benoit Roux. Modeling induced polarization with classical drude oscillators: Theory and molecular dynamics simulation algorithm. *The Journal of Chemical Physics*, 119(6):3025–3039, 2003.
- [92] Alain Dequidt, Julien Devémy, and Agílio AH Pádua. Thermalized drude oscillators with the lammmps molecular dynamics simulator. *Journal of Chemical Information and Modeling*, 56(1):260–268, 2015.
- [93] Christopher I Bayly, Piotr Cieplak, Wendy Cornell, and Peter A Kollman. A well-behaved electrostatic potential based method using charge restraints for deriving atomic charges: the resp model. *The Journal of Physical Chemistry*, 97(40):10269–10280, 1993.

- [94] Wendy D Cornell, Piotr Cieplak, Christopher I Bayly, and Peter A Kollmann. Application of resp charges to calculate conformational energies, hydrogen bond energies, and free energies of solvation. *Journal of the American Chemical Society*, 115(21):9620–9631, 1993.
- [95] Martin Neumann. Dipole moment fluctuation formulas in computer simulations of polar systems. *Molecular Physics*, 50(4):841–858, 1983.
- [96] M Neumann and O Steinhauser. On the calculation of the dielectric constant using the ewald-kornfeld tensor. *Chemical Physics Letters*, 95(4-5):417–422, 1983.
- [97] M Neumann and O Steinhauser. Computer simulation and the dielectric constant of polarizable polar systems. *Chemical Physics Letters*, 106(6):563–569, 1984.
- [98] Simon W de Leeuw, John William Perram, and Edgar Roderick Smith. Simulation of electrostatic systems in periodic boundary conditions. i. lattice sums and dielectric constants. In *Proceedings of the Royal Society of London A: Mathematical, Physical and Engineering Sciences*, volume 373, pages 27–56. The Royal Society, 1980.
- [99] Kazuya Shiratori and Akihiro Morita. Molecular theory on dielectric constant at interfaces: A molecular dynamics study of the water/vapor interface. *The Journal of Chemical Physics*, 134(23):234705, 2011.
- [100] Daan Frenkel and Berend Smit. Understanding molecular simulation: from algorithms to applications. *Computational sciences series*, 1:1–638, 2002.
- [101] Mike P Allen and Dominic J Tildesley. *Computer simulation of liquids*. Oxford university press, 1989.

-
- [102] Loup Verlet. Computer “experiments” on classical fluids. i. thermodynamical properties of lennard-jones molecules. *Physical Review*, 159(1):98, 1967.
- [103] Ulrich Essmann, Lalith Perera, Max L Berkowitz, Tom Darden, Hsing Lee, and Lee G Pedersen. A smooth particle mesh ewald method. *The Journal of Chemical Physics*, 103(19):8577–8593, 1995.
- [104] Tom Darden, Darrin York, and Lee Pedersen. Particle mesh ewald: An n·log (n) method for ewald sums in large systems. *The Journal of Chemical Physics*, 98(12):10089–10092, 1993.
- [105] Zhu Liu, Jakob Timmermann, Karsten Reuter, and Christoph Scheurer. Benchmarks and dielectric constants for reparametrized opl and polarizable force field models of chlorinated hydrocarbons. *The Journal of Physical Chemistry B*, 2017.
- [106] John M Wood. Chlorinated hydrocarbons: oxidation in the biosphere. *Environmental Science & Technology*, 16(5):291A–297A, 1982.
- [107] Liem X Dang. Intermolecular interactions of liquid dichloromethane and equilibrium properties of liquid-vapor and liquid-liquid interfaces: a molecular dynamics study. *The Journal of Chemical Physics*, 110(20):10113–10122, 1999.
- [108] Thomas Fox and Peter A Kollman. Application of the resp methodology in the parametrization of organic solvents. *The Journal of Physical Chemistry B*, 102(41):8070–8079, 1998.
- [109] Alexander D Mackerell. Empirical force fields for biological macromolecules: overview and issues. *Journal of Computational Chemistry*, 25(13):1584–1604, 2004.

- [110] Michiel Sprik and Michael L Klein. A polarizable model for water using distributed charge sites. *The Journal of Chemical Physics*, 89(12):7556–7560, 1988.
- [111] D Van Belle and SJ Wodak. Extended lagrangian formalism applied to temperature control and electronic polarization effects in molecular dynamics simulations. *Computer Physics Communications*, 91(1-3):253–262, 1995.
- [112] Y Marcus. The properties of solvents: Wiley series in solutions chemistry. *Baffins Lane, Chichester*, 4, 1998.
- [113] William M Haynes. *CRC handbook of chemistry and physics*. CRC press, 2014.
- [114] M Frenkel, X Hong, Q Dong, X Yan, and RD Chirico. 2.2. 1 c1-c2. In *Densities of Halohydrocarbons*, pages 107–130. Springer, 2003.
- [115] MJ Frisch, GW Trucks, Hs B Schlegel, GE Scuseria, MA Robb, JR Cheeseman, JA Montgomery Jr, TKKN Vreven, KN Kudin, JC Burant, et al. Gaussian 03, revision c. 02; gaussian, inc. *Wallingford, CT*, 26, 2004.
- [116] Rainer Storn and Kenneth Price. Differential evolution—a simple and efficient heuristic for global optimization over continuous spaces. *Journal of Global Optimization*, 11(4):341–359, 1997.
- [117] Aaron Garrett. Inspyred: Bio-inspired algorithms in python. <http://pythonhosted.org/inspyred/>, 2014.
- [118] Jin Yong Lee, Norio Yoshida, and Fumio Hirata. Conformational equilibrium of 1,2-dichloroethane in water: comparison of pcm and rism-scf methods. *The Journal of Physical Chemistry B*, 110(32):16018–16025, 2006.

- [119] Bryan M Wong, Maria M Fadri, and Sumathy Raman. Thermodynamic calculations for molecules with asymmetric internal rotors. ii. application to the 1,2-dihaloethanes. *Journal of Computational Chemistry*, 29(3):481–487, 2008.
- [120] Richard Renou, Minxia Ding, Haochen Zhu, Anthony Szymczyk, Patrice Malfreyt, and Aziz Ghoufi. Concentration dependence of the dielectric permittivity, structure, and dynamics of aqueous nacl solutions: Comparison between the drude oscillator and electronic continuum models. *The Journal of Physical Chemistry B*, 118(14):3931–3940, 2014.
- [121] Victor M Anisimov, Guillaume Lamoureux, Igor V Vorobyov, Niu Huang, Benoît Roux, and Alexander D MacKerell. Determination of electrostatic parameters for a polarizable force field based on the classical drude oscillator. *Journal of Chemical Theory and Computation*, 1(1):153–168, 2005.
- [122] Meagan C Small, Asaminew H Aytenfisu, Fang-Yu Lin, Xibing He, and Alexander D MacKerell. Drude polarizable force field for aliphatic ketones and aldehydes, and their associated acyclic carbohydrates. *Journal of Computer-Aided Molecular Design*, 31(4):349–363, 2017.
- [123] Justin A Lemkul, Jing Huang, Benoît Roux, and Alexander D MacKerell Jr. An empirical polarizable force field based on the classical drude oscillator model: development history and recent applications. *Chemical Reviews*, 116(9):4983–5013, 2016.
- [124] Keith D Bonin and Vitaly V Kresin. *Electric-dipole polarizabilities of atoms, molecules, and clusters*. World Scientific, 1997.
- [125] Orsolya Gereben and László Pusztai. On the accurate calculation of the dielectric constant from molecular dynamics simulations:

The case of spc/e and swm4-dp water. *Chemical Physics Letters*, 507(1):80–83, 2011.

- [126] Yujie Wu, Harald L Tepper, and Gregory A Voth. Flexible simple point-charge water model with improved liquid-state properties. *The Journal of Chemical Physics*, 124(2):024503, 2006.
- [127] Carl Caleman, Jochen S Hub, Paul J van Maaren, and David van der Spoel. Atomistic simulation of ion solvation in water explains surface preference of halides. *Proceedings of the National Academy of Sciences of the United States of America*, 108(17):6838–6842, 2011.
- [128] Erik JW Wensink, Alex C Hoffmann, Paul J van Maaren, and David van der Spoel. Dynamic properties of water/alcohol mixtures studied by computer simulation. *The Journal of Chemical Physics*, 119(14):7308–7317, 2003.
- [129] John G Kirkwood and Frank P Buff. The statistical mechanical theory of surface tension. *The Journal of Chemical Physics*, 17(3):338–343, 1949.
- [130] Steve Plimpton. Fast parallel algorithms for short-range molecular dynamics. *Journal of Computational Physics*, 117(1):1–19, 1995.
- [131] Steve Plimpton, Matt Jones, and Paul Crozier. Pizza.py toolkit. Technical report, Sandia National Laboratories, 2006.
- [132] Kazutoshi Tanabe. Calculation of infrared band intensities and determination of energy differences of rotational isomers of 1,2-dichloro-, 1,2-dibromo- and 1-chloro-2-bromoethane. *Spectrochimica Acta Part A: Molecular Spectroscopy*, 28(3):407–424, 1972.
- [133] Dmitry Bedrov, Oleg Borodin, Zhe Li, and Grant D Smith. Influence of polarization on structural, thermodynamic, and

- dynamic properties of ionic liquids obtained from molecular dynamics simulations. *The Journal of Physical Chemistry B*, 114(15):4984–4997, 2010.
- [134] TJ Morrow and ER Smith. Simulation calculation of dielectric constants: Comparison of methods on an exactly solvable model. *Journal of Statistical Physics*, 61(1):187–201, 1990.
- [135] Thomas D Kuehne, Tod A Pascal, Efthimios Kaxiras, and Yousung Jung. New insights into the structure of the vapor/water interface from large-scale first-principles simulations. *The Journal of Physical Chemistry Letters*, 2(2):105–113, 2010.
- [136] György Hantal, M Natália DS Cordeiro, and Miguel Jorge. What does an ionic liquid surface really look like? unprecedented details from molecular simulations. *Physical Chemistry Chemical Physics*, 13(48):21230–21232, 2011.
- [137] György Hantal, Iuliia Voroshylova, M Natália DS Cordeiro, and Miguel Jorge. A systematic molecular simulation study of ionic liquid surfaces using intrinsic analysis methods. *Physical Chemistry Chemical Physics*, 14(15):5200–5213, 2012.
- [138] Miguel Jorge, Gyorgy Hantal, Pál Jedlovszky, and M Natália DS Cordeiro. A critical assessment of methods for the intrinsic analysis of liquid interfaces: 2. density profiles. *The Journal of Physical Chemistry C*, 114(43):18656–18663, 2010.
- [139] Miguel Jorge and M Natália DS Cordeiro. Intrinsic structure and dynamics of the water/nitrobenzene interface. *The Journal of Physical Chemistry C*, 111(47):17612–17626, 2007.
- [140] Mária Darvas, Miguel Jorge, M Natalia DS Cordeiro, and Pál Jedlovszky. Solvation free energy profile of the scn⁻ion across the water-1,2-dichloroethane liquid/liquid interface. a computer

simulation study. *The Journal of Physical Chemistry C*, 115(22):11140–11146, 2011.

- [141] Miguel Jorge and M Natália DS Cordeiro. Molecular dynamics study of the interface between water and 2-nitrophenyl octyl ether. *The Journal of Physical Chemistry B*, 112(8):2415–2429, 2008.
- [142] Pedro Alexandrino Fernandes, M Natalia DS Cordeiro, and Jose ANF Gomes. Molecular simulation of the interface between two immiscible electrolyte solutions. *The Journal of Physical Chemistry B*, 105(5):981–993, 2001.
- [143] Pedro Alexandrino Fernandes, M Natalia DS Cordeiro, and Jose ANF Gomes. Influence of ion size and charge in ion transfer processes across a liquid— liquid interface. *The Journal of Physical Chemistry B*, 104(10):2278–2286, 2000.
- [144] Pedro Alexandrino Fernandes, M Natalia DS Cordeiro, and José ANF Gomes. Molecular dynamics simulation of the water/2-heptanone liquid-liquid interface. *The Journal of Physical Chemistry B*, 103(30):6290–6299, 1999.
- [145] Tatsuya Ishiyama, Yuji Sato, and Akihiro Morita. Interfacial structures and vibrational spectra at liquid/liquid boundaries: molecular dynamics study of water/carbon tetrachloride and water/1,2-dichloroethane interfaces. *The Journal of Physical Chemistry C*, 116(40):21439–21446, 2012.
- [146] Shaowei Ong, Xiaolin Zhao, and Kenneth B Eissenthal. Polarization of water molecules at a charged interface: second harmonic studies of the silica/water interface. *Chemical Physics Letters*, 191(3-4):327–335, 1992.
- [147] Per Linse. Monte carlo simulation of liquid-liquid benzene-water interface. *The Journal of Chemical Physics*, 86(7):4177–4187, 1987.

-
- [148] Aldert R van Buuren, Siewert Jan Marrink, and Herman JC Berendsen. A molecular dynamics study of the decane/water interface. *The Journal of Physical Chemistry*, 97(36):9206–9212, 1993.
- [149] David Michael and Ilan Benjamin. Molecular dynamics simulation of the water— nitrobenzene interface. *Journal of Electroanalytical Chemistry*, 450(2):335–345, 1998.
- [150] Seung Soon Jang, Shiang-Tai Lin, Prabal K Maiti, Mario Blanco, William A Goddard, Patrick Shuler, and Yongchun Tang. Molecular dynamics study of a surfactant-mediated decane-water interface: effect of molecular architecture of alkyl benzene sulfonate. *The Journal of Physical Chemistry B*, 108(32):12130–12140, 2004.
- [151] William E Lorensen and Harvey E Cline. Marching cubes: A high resolution 3d surface construction algorithm. In *ACM Siggraph Computer Graphics*, volume 21, pages 163–169. ACM, 1987.
- [152] Dennis K Hore, Dave S Walker, and Geraldine L Richmond. Water at hydrophobic surfaces: When weaker is better. *Journal of the American Chemical Society*, 130(6):1800–1801, 2008.
- [153] Eric S Shamay, Kevin E Johnson, and Geraldine L Richmond. Dancing on water: The choreography of sulfur dioxide adsorption to aqueous surfaces. *The Journal of Physical Chemistry C*, 115(51):25304–25314, 2011.
- [154] O Teschke, G Ceotto, and EF De Souza. Interfacial water dielectric-permittivity-profile measurements using atomic force microscopy. *Physical Review E*, 64(1):011605, 2001.

List of Figures

- 1.1 Schematic representation of the solid-liquid interface between water and a variety of hydrophobic or hydrophilic substrates (left) with the parallel or perpendicular dielectric response (right). Reprinted with permission from ref. [33]. © 2013 American Chemical Society. 3
- 1.2 Snapshot of an instantaneous equilibrium configuration of the water/DCE interface in the top panel and the representation of the dipole fluctuations of the same simulation snapshot in the bottom panel. Water molecular dipole moments are marked by blue arrows. Red arrows are those of DCE molecules. 8
- 3.1 Dipole moment (left, dipole profile) and torsional potential energy (right, potential energy profile) of a single 1,2-DCE molecule as a function of its Cl-C-C-Cl dihedral angle. The quantum chemical reference of the dipole profile is calculated with GAUSSIAN 03 using the 6-311G* basis set.[115] The quantum chemical reference of the potential energy profile is calculated with GAUSSIAN 03 at B3LYP aug-cc-pVDZ level.[115] The potential energy of the most stable conformer is set to zero. 26

3.2	Deviations of the properties obtained by using the improved OPLS-NP and OPLS-DO models with respect to the experiment value, comparing to those of the standard OPLS all atom parametrization. (Other labels consist with Table 3.4.)	44
3.3	Static bulk dielectric constant ϵ as a function of the sampling time for the CHCs studied. All the simulations have been already equilibrated prior to these runs. Reproduced with permission from ref. [i]. © 2017 American Chemical Society.	45
3.4	Static bulk dielectric constant ϵ as a function of the system size for 1,2-DCE-NP and 1,2-DCE-DO models. The number of molecules N_1, N_2, N_3, N_4 in the four different simulation systems are 63, 126, 189 and 252, respectively. Reproduced with permission from ref. [i]. © 2017 American Chemical Society.	46
3.5	Temperature dependence of isothermal compressibility k_T for the CHC models. The black dashed lines are the polynomial fitting curves for each liquid shown. The cyan-circle marked outliers of the CHCl_3 model at 328 K, CH_2Cl_2 model at 303 K and 1,2-DCE-NP model at 303 K and 318 K are removed from the fit. All models capture the trend of increasing k_T with increasing temperature. Reproduced with permission from ref. [i]. © 2017 American Chemical Society.	47
3.6	Temperature dependence of the static bulk dielectric constant ϵ for the CHC models. The black dashed lines are the polynomial fitting curves for each liquid shown. All models capture the trend of decreasing ϵ with increasing temperature. Reproduced with permission from ref. [i]. © 2017 American Chemical Society.	49
3.7	The isothermal compressibility $k_T(T)$ as a function a temperature with its polynomial fitting for CHCs. Reproduced with permission from ref. [i]. © 2017 American Chemical Society.	51

- 3.8 The static dielectric constant $\epsilon(T)$ as a function a temperature with its polynomial fitting for CHCs. Reproduced with permission from ref. [i]. © 2017 American Chemical Society. 52
- 4.1 Schematic representation of the interface structure in the same snapshot from a MD simulation: (a) the instantaneous interface; (b) the average Gibbs dividing interface. 61
- 4.2 The distribution of dipole moment magnitudes for the water/DCE LLI system (left panel) with water molecular dipoles shown as black histogram while DCE as blue histogram. The histograms of molecular dipole moment magnitudes have been averaged over whole trajectories. The *trans/gauche* ratio of the total DCE phase is 0.465. The right panel shows the fluctuations of the *trans/gauche* ratio (black curves and left axis) and average absolute molecular dipole moment (blue curves and right axis) of the total DCE phase within each LLI's MD snapshot as a function of the simulation time. . . . 66
- 4.3 Molecular number density as a function of distance from the respective instantaneous interface along the z-axis (blue and black solid lines refer to water and DCE components, respectively; left axis), normalized by the experimental molecular number density of N_{ρ}^{water} and N_{ρ}^{DCE} . Contributions of the *gauche* (cross) and *trans* (plus) DCE conformers are also showed, scaled by N_{ρ}^{DCE} of the overall DCE molecules. The oscillations of the DCE density profile are mostly due to the *gauche* conformer. The zero dashed line is set at the central water phase. Negative values indicate positions below the central water and are measured with respect to the lower instantaneous LLI (the left light grey region), while positive values are relative to the upper instantaneous LLI (the right light grey region). 68

-
- 4.4 Parallel dielectric profiles ($\epsilon_{\parallel}(\Delta z)$, top panel) with respect to the distances normal to the lower and upper instantaneous interface respectively. The zero locations are approximately the reference instantaneous interfaces. Parallel dielectric permittivity as a function of z referenced to the average Gibbs dividing interface ($\epsilon_{\parallel}(z)$, bottom panel). The dashed lines show the central water phase, corresponding to the zero dashed line in Figure 4.3. 71
- 4.5 Schematic orientation of the water and DCE molecule the instantaneous liquid-liquid interface. The definition of the angles θ and φ in the local atomic coordinate frame for water and DCE molecules are showed. The vectors are the instantaneous interface normal vector \vec{n} , the molecular dipole vector $\vec{\mu}$, the molecular normal vector \vec{m} for water and the carbon-carbon axis vector \vec{c} for DCE; the new defined vector \vec{d} for *trans* DCE. 72

- 4.6 Top panels: correlation histograms of *trans* DCE within an interfacial region from 0.5 Å to 2.5 Å relative to the lower instantaneous LLI ($z = 0$ Å). Top left panel shows the correlation between the C-C vector \vec{c} and dipole vector $\vec{\mu}$, while top right panel shows that between the C-C vector \vec{c} and the new defined vector \vec{d} . The horizontal axes of the histograms represent $\cos \alpha = \frac{\langle \vec{n} | \vec{c} \rangle}{\|\vec{c}\|}$. The vertical axis of the top left panel represents $\beta = \arccos(\frac{\langle \vec{n} | \vec{\mu} \rangle}{\|\vec{\mu}\|})$, whereas it represents $\beta = \arccos(\frac{\langle \vec{n} | \vec{d} \rangle}{\|\vec{d}\|})$ in the top right panel. The grey thick dashed line in the top right panel is a perfect Sine function of angle β . Areas of low intensity appear in dark blue, and highest intensity in dark red. The black curve in the bottom panel shows population distributions lie within the intensified red and white realm (see the top right panel) as a function of $\cos \alpha$. The blue curve in the bottom panel shows the normed relative population ratio (see text) as a function of $\cos \alpha$. The dashed lines in the top right panel indicate the analyzed windows for the integral. 75
- 4.7 Molecular orientation histograms of H₂O for the water/DCE LLI system with respect to the lower instantaneous interface region. The location of each of the regions which are represented by these histogram is given by their distance from the LLI in Å. The instantaneous interface is located at 0 Å with positive distances toward the water phase. Each histogram shows the bivariate angle distribution for $\cos \theta$ (horizontal axes, $\cos \theta = \frac{\langle \vec{n} | \vec{\mu} \rangle}{\|\vec{\mu}\|}$) and φ (vertical axes, $\varphi = \arccos(\langle \vec{n}_\perp | \vec{m} \rangle)$). Regions of high intensity are marked as dark red, and low intensity are dark blue. A completely white histogram would correspond to a distribution which attains the perfect average homogenous bulk state at each point. 77

- 4.8 Relative population within the regions of preferential molecular orientation marked by the semi-ellipse for water (blue line, left axis) and rectangular box for DCE (red line, right axis) in the respective orientation profiles. The details to define these regions can be found in the main text. The population of each slab with respect to the instantaneous LLI is normalized by the respective molecular number density. 80
- 4.9 Molecular orientation histograms of DCE near the water/DCE LLI with respect to the lower instantaneous interface $z = 0$ Å (top panel). Positive distances indicate locations further into the DCE phase. Each histogram is a bivariate angle distributions for $\cos \theta$ (horizontal axes, $\cos \theta = \frac{\langle \vec{n} | \vec{\mu} \rangle}{\|\vec{\mu}\|}$) and φ (vertical axes, $\varphi = \arccos(\langle \vec{n}_\perp | \vec{c} \rangle)$). Regions of high intensity are marked as dark red, and low intensity are dark blue. Bottom panel shows the molecular orientation histograms of DCE near LLI after removing the Sine statistical effect (see text) while all other settings are the same for the top panel. A completely white histogram in the bottom panel corresponds to a distribution which attains the perfect average homogenous bulk DCE state at each point. 82
- 4.10 Integrals $\int_{-1}^0 H d \cos \theta$ as a function of the angle φ with respect to the histograms in the top panel of Figure 4.9. All the integrals are normalized by the respective total population within each histogram. 84

- 4.11 Orientation profiles of the *gauche* (top panel) and *trans* DCE (bottom panel) with respect to the lower instantaneous LLI. The respective conformer and the average number of molecules in each layer is showed on the top of each plot. The distances of each histogram from the instantaneous LLI are also showed on the top in Å with the location of the LLI set at 0 Å. Regions of high intensity are marked as dark red, and low intensity are dark blue. 86
- 4.12 Relative population within the intensified region marked by the dashed rectangular box for *gauche* (blue line, left axis) and *trans* DCE (red line, right axis) in the respective orientation profiles in Figure 4.11. The definition of these regions are same as for the local DCE population. The population of each slab with respect to the *gauche* or *trans* profile is normalized by the overall number of DCE molecules within the same layer. The inset graph shows the *trans/gauche* ratio as a function of vertical distance to instantaneous LLI. 87
- 4.13 Perpendicular dielectric profiles ($\epsilon_{\perp}(\Delta z)$, two top panels) with respect to the distances normal to the lower (blue) and upper (black) instantaneous interface. The zero locations are approximately the reference instantaneous interfaces. The bottom panel shows for comparison the perpendicular dielectric permittivity as a function of z referenced to the average Gibbs dividing interface. The black and blue dashed lines show the respective upper and lower LLI, corresponding to the zero locations in the two top panels. 89
- 4.14 The polarization correlation function $h_{zz}(\Delta z)$ as a function of the distance normal to the lower instantaneous interface, along with that corresponding to various dielectric constants from Eq. 4.4 91

4.15 Perpendicular dielectric permittivity at the center of the water phase as a function of the thickness of the water phase in water/DCE LLI simulations. The small inset graph shows the parallel dielectric tensor components in the same situation.	93
------------------------------------------------------------------------------------------------------------------------------------------------------------------------------------------------------------------------------------------------------------------	----

List of Tables

3.1 Atomic charges for the interaction site of the chlorinated hydrocarbon molecules. q denotes the atomic charge. Reproduced with permission from ref. [i]. © 2017 American Chemical Society.	31
3.2 Coefficients of the torsion potential energy for 1,1-DCE and 1,2-DCE. Reproduced with permission from ref. [i]. © 2017 American Chemical Society.	34
3.3 Sizes of the cubic liquid-vapor simulation boxes for the different CHC systems, only showing the edge length in the X dimension. Each system contains $N = 1000$ molecules. Reproduced with permission from ref. [i]. © 2017 American Chemical Society.	38

3.4	Properties of CHCs with the improved force field models. ρ , ΔH_{vap} , r , ϵ , α_P , k_T , C_V and C_P denote the density, surface tension, relative dielectric constant, volumetric expansion coefficient, isothermal compressibility, heat of vaporization, constant volume heat capacity and constant pressure heat capacity at 298.15 K. OPLS-NP is the new non-polarizable model which is directly comparable to the standard OPLS (all atom) parametrization. OPLS-DO denotes the polarizable model (see text for details). ^a Reference [112]. ^b Reference [113]. ^c Reference [114]. ^d For the polarizable model $\epsilon_\infty = 1.54$ is determined according to the procedure from refs [88] and vorobyov2005polarizable. Reproduced with permission from ref. [i]. © 2017 American Chemical Society.	42
3.5	Parametrization of temperature dependence of isothermal compressibility in a polynomial form $k_T = A + BT + CT^2$. N is the number of data points included in each fit. Reproduced with permission from ref. [i]. © 2017 American Chemical Society.	48
3.6	Parametrization of temperature dependence of dielectric constant in a polynomial form $\epsilon = A + BT + CT^2$. N is the number of data points included in each fit. Reproduced with permission from ref. [i]. © 2017 American Chemical Society.	48

Acknowledgements

This work has been performed at the Chair of Theoretical Chemistry of Prof. Dr. Karsten Reuter at the Technische Universität München between October 2013 and November 2017. First of all, I would like to express my sincere gratitude to Prof. Dr. Karsten Reuter for offering the opportunity for a PhD. I would like to express my deep thanks to Dr. Christoph Scheurer for being my direct supervisor and providing me innumerable valuable instructions and suggestions about my research and help me through the PhD study. Whenever I needed him, he was always there and very helpful in answering all my questions. I sincerely appreciate all his patient and careful corrections through completing this thesis.

Many thanks to Hendrik Heenen and Georg Michelitsch for their willingness to help with my simulation codes during the early stages of joining the group; my officemates Dr. Simon Rittmeyer and Markus Sinstein for providing lots of helpful information, help, and good time, making our office so live and enjoyable; Jakob Timmermann for the fruitful collaborations in the research; David Eager for the provoking discussions related to the research of dielectric things.

I would also like to thank Dr. Stefan Ringer, Dr. Juan Lorenzi, Dr. Christoph Sober for their technical support; Ruth Mösch for her kind

ACKNOWLEDGEMENTS

support that makes my PhD life much easier; Dr. Tongyu Wang and Dr. Berna Dogan for their help in the beginning of my PhD. Furthermore, I would specifically like to thank all my former and current colleagues of the whole chair of the theoretical chemistry for their company and support.

My sincere thanks are also extended to my friends in Munich: Xiang Lu, Long Cheng, Dr. Weiwei Xie, Xiuxiu Wu, Zhen Yao, Di Xu, Yue Li for all the times we had in the past years.

The most important, my dearest thanks go to my parents and my sisters for their full support and encouragement throughout all these years of my study. To my fiancée Yuanyuan Qu, your love, support and encouragement help me get through all the ups and downs of our lives.

Finally I should mention the work presented in this thesis was supported by the China Scholarship Council (grant number: 201306190104), which is gratefully acknowledged.

List of Publications

- [i] Zhu Liu, Jakob Timmermann, Karsten Reuter, and Christoph Scheurer. Benchmarks and dielectric constants for reparametrized opls and polarizable force field models of chlorinated hydrocarbons. *The Journal of Physical Chemistry B*, 2017 (**ACS Editor's Choice** article).
- [ii] Zhu Liu, Jakob Timmermann, Karsten Reuter, and Christoph Scheurer. Dielectric permittivity of the instantaneous water/dichloroethane liquid-liquid interface. *to be submitted*, 2017.